Microgrid Enabling Towards the Implementation of Smart Grids

by

Mohammed Nassar

A thesis
presented to the University of Waterloo
in fulfillment of the
thesis requirement for the degree of
Doctor of Philosophy
in
Electrical and Computer Engineering

Waterloo, Ontario, Canada, 2017

Examining Committee Membership

The following served on the Examining Committee for this thesis. The decision of the Examining Committee is by majority vote.

External Examiner	Osama A. Mohammed Professor
Supervisor(s)	Magdy Salama Professor
Internal Member	Mehrdad Kazerani Professor
Internal Member	Ramadan El-Shatshat Lecturer
Internal-external Member	Jatin Nathwani Professor

AUTHOR'S DECLARATION

I hereby declare that I am the sole author of this thesis. This is a true copy of the thesis, including any required final revisions, as accepted by my examiners.

I understand that my thesis may be made electronically available to the public.

Abstract

Smart grids have emerged as dominant platforms for effectively accommodating high penetration of renewable-based distributed generation (DG) and electric vehicles (EVs). These smart paradigms play a pivotal role in the advancement of distribution systems and pave the way for active distribution networks (ADNs). However, the large number of smart meters deployed in the distribution system (e.g., 200 million smart meters will be installed in Europe by 2020) represents one of the main challenges facing the management and control of distribution networks and thus the enabling of smart grids. In addition to the data tsunami flooding central controllers, the concerns about privacy and system vulnerability are fast becoming a key restraint for the implementation of the smart grids. These concerns are prompting utilities to be more reluctant to adopt new techniques, leaving the distribution system mired in relatively old-fashioned routines. Microgrids provide an ideal paradigm to form smart grids, thanks to their limited size and ability to 'island' when supplying most of their loads during emergencies, which improves system reliability. However, preserving load-generation balance is comprehensively challenging, given that microgrids are dominated by renewable-based DGs, which are characterized by their probabilistic nature and intermittent power. Although microgrids are now well-established and have been extensively studied, there is still some debate over having microgrids that are solely ac or solely dc, with the consensus tending toward hybrid ac-dc microgrids. Furthermore, while some research has addressed using solely ac microgrids, the planning of hybrid ac-dc microgrids has not yet been investigated, despite the many benefits these types of microgrids offer. Additionally, developing steady-state analysis tools capable of handling grid-connected mode and islanded mode for the operation of ac microgrids and hybrid ac-dc microgrids still has uncertainties about their computational burden, complexity, and convergence. The high R/X ratio characterized distribution systems result in ill-condition that hinders the convergence of conventional Newton Raphson (NR) techniques. Moreover, calculating the inversion of the Jacobian matrix that is formed from the calculation of derivatives adds to the complexity of these techniques. Therefore, developing a simple, accurate, and fast steady-state analysis tool is crucial for enabling microgrids and hence smart grids.

Driven by the aforementioned challenges, the broad goal of this thesis is to enable microgrids as building clusters to smooth and accelerate the realization of smart grids. Achieving this objective involves a number of stages, as follows: 1) The development of probabilistic models for loads and renewable DG-based output power. These models are then integrated with the load flow analysis techniques to form a probabilistic power flow (PPF) tool. 2) The proposal of a novel operational

philosophy that divides existing bulky grids into manageable clusters of self-adequate microgrids that adapt their boundaries to keep load-generation balance at different operating scenarios. 3) The proposal of planning a framework for the newly constructed grids as hybrid ac-dc microgrids with minimum levelized investment costs and consideration of the probabilistic nature of load and renewable generation. 4) The development of a branch-based power flow algorithm for steady-state analysis of ac microgrids and hybrid ac-dc microgrids.

Acknowledgements

First and foremost, praise be to Allah, the Almighty and Merciful, for the heavenly blessing and guidance that led me this far.

Then, I would like to express my sincere gratitude to my advisor, Professor Magdy Salama, for his continuous support, guidance, and patience. He was always more than happy to discuss not only about research but also personal issues. He was always willing to provide me with honest advice and suggestions for improvements whenever I needed them. Words cannot describe how grateful I am.

Next, I would like to thank all my PhD committee members: Professor Ramadan El-Shatshat, Professor Mehrdad Kazerani, and Professor Jatin Nathwani, for their time, suggestions, and constructive criticism. Thanks are also extended to my external examiner, Professor Osama A. Mohammed, for coming to referee this thesis.

Besides my advisor and my committee members, I would like to express my honest thanks to Dr. Mohamed Elkhatib, for all the helpful comments regarding my studies and my life in Waterloo. Also, my sincere thanks go to my colleague Amr Said for all the deep technical discussions we had.

Last but not least, I would like to thank my family: my wife, Nancy, who gives me moral and emotional support in my life, for the sleepless nights we stayed working together before deadlines, and for all the fun we had in the last four years, and my mother, Hekmat, for supporting me spiritually throughout my life and her unconditional love. I cannot find any appropriate words to express how grateful I am to all of you for every sacrifice that you have made on my behalf. I am also grateful to my other family members (Mona, Maryem and Moataz) who have supported me along the way. Finally, lots of love goes to my son, Saif Eldeen, who always adds fun to my life and succeeded to make me laugh from the heart and forget about being overloaded.

Dedication

To my beloved wife and soul mate, Nancy, in recognition of your endless patience, love, support, and encouragement.

Table of Contents

List of Figures

List of Tables

Nomenclature

Acronyms

PST	Phase-shifting transformers
FACTS	Flexible ac transmission systems
HVAC	High voltage ac
HVDC	High voltage dc
DGs	Distributed generations
MT	Micro turbine
PEV	Plug-in electric vehicles
MCS	Monte Carlo Simulation
ARMA	Auto regression moving average
WECS	Wind energy conversion system
PDF	Probability distribution function
IESO	Independent Electrical System Operator
PV	Photovoltaic
MPP	Maximum power point
RTS	Reliability test system
PCC	Point of common coupling
ESS	Energy storage system
IC	Interlinking converter
NTR	Newton-trusted-region
NR	Newtorn-Raphson
MTDC	Multi-terminal dc systems
K-S	Kolmogorov-Smirnov
A-D	Anderson-Darling
CDF	Cumulative density function
PPF	Probabilistic power flow
2PEM	Two-point estimate method
FBS	Forward backward sweep
KCL	Kirchhoff’s current law

KVL	Kirchhoff's voltage law
DOE	Department of energy
CLs	Candidate lines
BBs	Boundary buses
DER	Distributed energy resources
CRF	Capital recovery factor
SoC	State of charge
O&M	Operational and maintenance
FR-FBS	Forward return forward backward sweep
BF	Backward forward

Functions

$f(x)$	Probability of variable x
$F(x)$	Cumulative probability of variable x

Sets

n	Set of data samples
N	Set of buses
$\boldsymbol{F}$	Set of fuel-based DG units
$\boldsymbol{L}$	Set of loads
$\boldsymbol{T}$	Set of interlinking converters
$\boldsymbol{W}$	Set of renewable DG units
$\boldsymbol{\eta_z}$	Set of neighboring zones of a zone ($\boldsymbol{z}$)
$\boldsymbol{N_{dg}}$	Set of DGs
x	Set of interlinking converters

Indices

$\boldsymbol{ac}$	Subscript for the ac systems
$\boldsymbol{B}$	Subscript for the ESS
$\boldsymbol{ch}$	Superscript for the ESS charging mode
$\boldsymbol{dc}$	Subscript for the dc systems
$\boldsymbol{dis}$	Superscript for the ESS discharging mode

$\boldsymbol{g}$	Index for distributed generation resource (DG)
$\boldsymbol{h}$	Index for hour
$\boldsymbol{t}$	Index of an interlinking converter
$\boldsymbol{V}$	Subscript for capacitive units
$\boldsymbol{z}$	Index for zone

Parameters

k	2-parmeter Weibull shape factor
c	2-parameter Weibull scale factor
v	Wind speed
σ	Standard deviation
v_m	Average wind speed
v_i	Wind speed sample i
$v_{ob,t}$	Wind speed observed at t
μ_t	Mean at t
$v_{est,t}$	Wind speed estimated at t
P_{rated}	Rated power
v_{ci}	Cut-in speed
v_{co}	Cut-out speed
v_r	Rated speed
$\alpha, \beta c$	Beta PDF parameters
I_{sc}	Short-circuit current
V_{oc}	Open-circuit voltage
I_{MPP}	Current at maximum power point
V_{MPP}	Voltage at maximum power point
N_{OT}	Nominal operating temperature
ω_o	Droop reference frequency
K_p	Active power droop slope
V_o	Droop reference voltage
K_v	Reactive power droop slope

Δf	Frequency deviation
Δv	Voltage deviation
V_{dc}	DC bus voltage
K_{dc}	Active power droop slope for dc DG
$P_{dc,max}$	Rated DG power
$V_{dc,max}$,	Maximum and minimum allowable voltage
x_i^j	Data sample i in cluster j
α, β, Γ	Weibull shape, scale and location parameters
γ, δ	Johnson SB shape parameters
λ, ξ	Johnson SB scale and location parameters
T_c, T_A	Cell temperature and ambient temperature in ºC
K_i, K_v	Voltage and current temperature coefficients
N	Number of cells per module
r_{ij}	Resistance of the line connecting buses i and j
x_{ij}	Reactance of the line connecting buses i and j
$Z_{i,j}$	impedance of the line connecting buses i and j
$\boldsymbol{\omega_{ref,i}}$	Reference frequency of DG i
$\boldsymbol{m_{p,i}}$	Active power droop coefficient of DG i
$\boldsymbol{m_{p,eq}}$	Active power equivalent droop slope
$\boldsymbol{V_{ref,i}}$	Reference voltage of DG i
$\boldsymbol{m_{q,i}}$	Reactive power droop coefficient of DG i
$\boldsymbol{V_{pivot,k}}$	Pivot point voltage at iteration k
$\boldsymbol{\rho}$	Reactive power share ratio
$\boldsymbol{S_{pivot,m}}$	Rated apparent power of pivot DG
$\boldsymbol{A_{ij}}$	Connectivity index
$\boldsymbol{P_{L,i}}$	Load active power at bus i
$\boldsymbol{Q_{L,i}}$	Load reactive power at bus i
$\boldsymbol{V^*}$	Reference voltage for DC DG`s droop
$\boldsymbol{m_V}$	DC DG`s droop slope

$e_{pu,x}$	Per unit error for IC x
CC	Cost for load curtailment
CE	Levelized investment cost of an ESS maximum SoC
CF	Levelized energy cost of the fuel-based DG units
CI	Levelized investment cost of an inverter
CP	Levelized investment cost of a DG or ESS power
CR	Levelized investment cost of a rectifier
CT	Levelized investment cost of an interlinking converter
CV	Levelized investment cost of a capacitor
P_L^{max}	Maximum active load demand
$Q_{L_{ac}}^{max}$	Maximum reactive load demand
$S_{L_{ac}}^{max}$	Maximum apparent load demand
u_d	Day weight during the year
β	Fraction of the peak demand corresponding to a specific scenario
γ	Available active power ratio of a renewable DG
η	Efficiency of the ESS power cycle
ρ	Ratio of the system power losses
σ	Ratio of the system power security
Ω_d^{st}	Daily probability of a combined load-generation scenario
Ω_{gd}^{st}	Daily probability of a generation scenario
Ω_{ld}^{st}	Daily probability of a load scenario
Ω_{gdh}^{st}	Probability of a generation state at time segment h
Ω_{ldh}^{st}	Probability of a load state at time segment h
$\Omega_{gdh+1\|}^{st}$ $\Omega_{ldh+1\|i}^{st}$	Generation and load probability of transition from a state at time segment h to another state at time segment h+1

Variables

V_i	Voltage magnitude at bus i
ω	System operating frequency
c_j	Centroid of cluster j
D	Statics of Kolmogorov-Smirnov test

A^2	Statics of Anderson-Darling test
s_a	Solar irradiance
$P_{j,k}$,	Injected active power at bus j and iteration k
$Q_{j,k}$	Injected reactive power at bus j and iteration k
$P_{i,j,k}$	Active power flows between buses i and j at iteration k
$Q_{i,j,k}$	Reactive power flows between buses i and j at iteration k
$I_{i,j,k}$	Current flows between buses i and j at iteration k
$P_{j,k}$,	Injected active power at bus j and iteration k
$\boldsymbol{P_i}$	Active power injected from DG i
$\boldsymbol{V_i}$	Voltage magnitude at DG i
$\boldsymbol{Q_i}$	Reactive power injected from DG i
$\boldsymbol{IC}$	Total investment cost
$\boldsymbol{M_z}$	Zone type (0 for dc, 1 for ac)
P, *Q*	Active and reactive powers (+ve if produced)
$\boldsymbol{P^{loss}}$	Associated power loss due to energy conversion
$\boldsymbol{P^{Cap}}$	Maximum installed power of a DG, ESS and rectifier
$\boldsymbol{Q^{cap}}$	The installed VAR of a capacitive unit
$\boldsymbol{S^{cap}}$	Maximum apparent power of DG, inverter and interlinking converter
$\boldsymbol{SoC^{Cap}}$	Maximum state of charge of an ESS
$\boldsymbol{SoC^{min}}$	Minimum state of charge of an ESS
$\boldsymbol{\alpha}$	Load curtailment ratio
$\boldsymbol{\omega_{cor,i}}$	frequency correction ratio
$\boldsymbol{P_{g_{AC}}}$	Total generated power from ac DGs
$\boldsymbol{P_{g_{DC}}}$	Total generated power from dc DGs
$\boldsymbol{P_{Load}}$	Total system load
$\boldsymbol{P_{Loss}}$	Total system losses
$\boldsymbol{P_{g_{AC}}}$	Total generated power from ac DGs
$\boldsymbol{P_{g_{DC}}}$	Total generated power from dc DGs
$\boldsymbol{P_{Load}}$	Total system load
$\boldsymbol{V_{pu,x}}$	Per unit voltage for IC x
$\boldsymbol{P_{IC,x}}$	Injected power from IC x

Chapter 1
Introduction

The electricity sector is facing serious problems as a result of aging power system infrastructure, limited capacity of transmission systems, rapidly growing demand for electricity, depletion of conventional energy resources, increasing concern over greenhouse gas emissions and global warming, and overwhelming data collection from smart meters. Thus, it is critically important to refine and improve the way in which players from different sectors construct the power system grid and manage electricity. In order to satisfy increasing electricity demands at high reliability and premium power quality, utilities have to add new central generation units, construct new extra high voltage (EHV) and high voltage (HV) transmission lines, install power quality conditioners, and extend and upgrade existing power distribution networks. However, achieving these modifications is challenging due to the shortage in investments, lack of available physical space for the expansion, and other environmental and policy-related concerns.

Hence, utilities apply three strategies to deal effectively with these challenges. The first strategy is based on improving the existing transmission capacity without building new lines. This is accomplished by using technically feasible methods such as phase-shifting transformers (PST) to improve the transmission network utilization and optimally placed flexible ac transmission systems devices (FACTS) to increase power system load-ability. It also includes placing series capacitors to improve load-ability or converting the existing high voltage ac (HVAC) transmission system to high voltage dc (HVDC) to increase the loadability and efficiency.

A second strategy is allowing for the installation of more DG units on the system instead of investing in transmission and distribution infrastructure upgrades. Numerous benefits can be achieved by placing generation close to customers, such as power loss reduction, fewer environmental impacts, peak saving, increased overall energy efficiency, relieved transmission and distribution network, voltage support, and deferred investments to upgrade existing generation, transmission, and distribution systems.

DG technologies may be conventional, such as micro turbine (MT), or non-conventional, such as fuel cells and renewable energy sources. However, renewable-based DGs are gaining most of the interest these days, thanks to their green effect on the environment, especially given the keen public awareness regarding environmental impacts of electric power generation. For example, in 2014, Canada

had 225 wind farms with over 5,130 wind turbines, for a total installed capacity of almost 9.7 GW, compared to 1998, when it had only 8 wind farms with 60 wind turbines and a 27 MW capacity. In addition, a total generation capacity of almost 1.8 GW from solar energy and 2.04 GW from biomass were available by 2014 [1], while in 2015, a total power of 2.4 GW from renewable resources was in service at the distribution level. The probabilistic nature of these renewable resources results in negative impacts and technical challenges when embedded into the distribution network, especially regarding power quality indices, power system reliability, voltage regulator operation and power system protection coordination.

A third strategy represents a long-term plan and is based on moving from the conventional grid to a smart grid. Smart grids can be defined as "intelligent electricity infrastructure that uses technology such as sensors, monitoring, two-way communications, automation and computational ability to improve the flexibility, reliability and efficiency of the electric power system". They are poised to become the future of the world's power systems, owing to the numerous advantages offered by their implementation, which may solve most of the present problems and challenges. Opportunities offered by smart grids can be summarized as follows [2]. Smart grids:

1. Allow customers to effectively manage their electricity use and benefit from conservation and small-scale generation.
2. Permit higher penetration of renewable electricity generation, such as wind and solar power, to connect to the electricity grid.
3. Improve reliability by helping utilities to quickly identify and fix outages and enable self-healing during system disturbances.
4. Facilitate convenient charging of electric vehicles.
5. Optimize assets utilization and avoid construction of back-up generation units.
6. Increase the utilization of existing power system capacity.
7. Improve the efficiency of existing electric power system.
8. Enable predictive maintenance.
9. Reduce fuel consumption by limiting the need for using inefficient generation during peak load periods.
10. Present new markets and opportunities.
11. Enable the widespread usage of energy storage devices to improve the power system performance.

However, moving from a conventional to a smart grid is a slow process due to the technical problems and technology limitations facing the construction and implementation of the grids. One of the most serious challenges facing the realization of smart grids is the tremendous amount of data that must be collected from all grid components and buses and the huge amount of control commands that need to be sent to the elements in the grid. This data tsunami is way beyond the capability of the existing processing devices, so many inaccurate assumptions and simplifying analyses are being applied. In addition, end-user de-motivators (such as loss of control and loss of privacy) limit the progress in smart grid implementation. With smart grids, the control is centralized, which may cause minor discomfort to users, as the central controllers could override users' control actions. Moreover, from the data collected from smart meters, detailed information about the end users' activities can be extracted, which deeply impacts the privacy of consumers.

Correspondingly, to enable the smart grid and accelerate the transition from a conventional power system to a smart grid, the existing gigantic and bulky power system should first be transferred into manageable, self-adequate, reliable and stable microgrids, a transition which will expedite the realization of smart grids using existing technologies. This can be divided into two schemes. The first scheme is adopting a novel management strategy based on an operational planning for the existing system and using the available resources as clusters of microgrids rather than a bulk unit. The second scheme is planning new systems and extensions of the existing systems as self-adequate microgrids. Each microgrid is a space-limited power distribution network that contains both load and generation units together and can operate autonomously or connected to another microgrid. Thus, the power system will be formed from clusters of self-controlled microgrids and will collect data and send commands to these microgrid entities.

The advent of electronically-based DGs and the radical changes in the nature of loading have promoted power distribution in a dc paradigm. On the one hand, greater economies could be achieved if renewable energy resources such as wind, PV, and ESSs were integrated into dc rather than ac systems. On the other hand, major loads such as modern elevators operate based on variable speed drives [3]. PEVs represent a crucial factor in future electric distribution systems, and extensive electronic loads do exist in all modern homes with new inventions, including high-quality and highly efficient dc lighting systems. Further considerations are the intuitive merits of DC systems, which are the reduction of interference with AC grids and facilitation of expanded power capacity. Thus, the

concept of dc systems has emerged for active distribution systems and isolated microgrids as well [4], [5].

As stated earlier, the concept of isolated microgrids has recently attracted significant attention since it provides a viable solution for remote community electrification. Isolated microgrids can eliminate investments on additional generation and transmission facilities to supply remote loads. Initiated as ac networks, similar to the common distribution systems, the construction of isolated microgrids has dramatically evolved to include dc and hybrid ac/dc systems that could adapt high penetration of dc-based DGs and loads [6], [7]. Recent publications have addressed several operational and planning issues in isolated microgrids. Operational studies include modelling and energy management. Additionally, load flow and stability have been extensively performed for the different isolated microgrid structures [7]-[10]. However, the planning studies are performed mostly for ac microgrids. In [11], a probabilistic VAR planning was proposed. The presented formulation incorporates a high penetration level of intermittent energy resources to address the minimization of power loss within active and reactive power adequate profiles. In [12], Jun et al. provided a coordinated sizing scheme for diesel generators and energy storage units to maintain the power adequacy in isolated microgrids. Based on the bifurcation theory, Guzmán et al. [13] introduced a scheduling methodology for the droop coefficients that improves the system frequency and voltage regulation. Morad et al. [14] optimized the droop settings in isolated microgrids of the DGs to compromise the system loadability and the economical behavior according to the fuzzy utility function. The aforementioned work was extended in [15] to include the improvement in the system voltage profile as well. However, the planning of new networks as clusters of hybrid microgrids to minimize investment costs and improve system efficiency was not considered. In fact, the configuration of such hybrid ac/dc microgrids has not yet been addressed at all in the literature.

Given the aforementioned discussion, smart grids cannot be realized with the existing technology, tools, and system structure: a step in-between is needed. The benefits of microgrids make them a perfect host for high penetration of renewable energy resources, while their size allows for realizing smart grid paradigms with existing know-how. The clustering of the existing system into smart microgrids represents an interesting research path, especially the operational planning framework that is needed for selecting the clustered network and the development of relevant operation tools. Moreover, the planning of new systems or extensions of existing systems should consider the hybrid ac-dc layout due to the rapid advances in electrical loads with more dc loads being used. Thus, a planning framework for these systems that considers the system type as a decision variable and plans the system as clusters

of self-adequate hybrid ac-dc entities represents a fresh research topic.

1.1 Motivation

The clustering of power systems into microgrids is a new planning philosophy in the power system area. The probabilistic nature of loads and renewable-based DGs present serious challenge in setting borders for self-adequate microgrids. The abandonment of the probabilistic nature of loads and generations hinders the successful islanding ability of clustered microgrids during disturbances due to load and generation imbalance. The literature contains frameworks for clustering power systems into self-adequate microgrids with static virtual borders. These borders are selected based on carrying out load flow analysis and minimizing the load-generation imbalance. However, the static borders approach cannot guarantee the self-adequacy operation of a microgrid when a large variability of load exists in the presence of renewable-based DGs. In addition, using the average concept to model load and generation power and avoiding the proper consideration of the probabilistic nature of renewable-based DGs and loads represents a serious deficiency in these studies.

The realization of this novel philosophy of constructing the power system from virtual clusters that are capable of islanding during disturbances can be divided into two stages. The first stage is the virtual partitioning of the existing power system into self-adequate clusters considering the current layout and structure of the system. The second stage is the optimal planning of new systems as self-adequate microgrids. The planning of these new systems has to consider the dc microgrids option due to their numerous benefits, as discussed earlier. Thus, the type of clustered microgrid (e.g., either dc or ac) will be part of the planning problem. On the other hand, in static clustering techniques, load flow analysis algorithms are applied considering grid connected mode while the clusters are selected to allow for successful islanding during disturbances. Thus, a scalable, accurate, fast, and generic load flow technique is a requisite for the successful operation and management of the clustered microgrids. The load flow analysis technique should be capable of accounting for different microgrid characteristics such as droop-controlled DGs and the absence of slack bus.

Although load flow analysis for islanded microgrids is extensively presented in recent literature, these analyses are based on a centralized approach through the formation and solution of Jacobian-like matrices. However, for the proposed operation philosophy of smart grids, distributed agents with limited computational capability are more appropriate than centralized powerful controllers, and thus the conventional derivative-based load flow will be inadequate for these applications. Hence, branch-

based techniques are the candidate methods for these applications due to their simplicity, scalability, and robustness, yet these techniques necessitate the existence of slack bus to guarantee convergence. The modification of branch-based techniques and adapting them to be applicable for islanded microgrids represents a challenging research topic that is not well-studied in the literature, especially when one considers the intrinsic characteristics of the branch-based techniques, such as the absence of a slack bus and the variable frequency behaviour of the microgrid. Moreover, with the emergent dc microgrids, the load flow tool should be applicable to hybrid layout with coupled ac and dc microgrids through an interlinking converter (IC) to ensure proper load-sharing between DGs. This tool is essential in steady-state and dynamic studies for both planning cases (e.g., clustered microgrids from an existing system or freshly planned microgrids).

Based on the aforementioned discussion, enabling smart grids can be achieved through novel paradigms that improve system reliability and can be managed using existing technologies. This transition will accelerate the move from conventional grids to smart and renewable-dominated grids. Moreover, these paradigms will represent a candidate host for applying optimal energy utilization and efficient power system operation strategies at a feasible cost. The probabilistic nature of renewable-based DGs and loads resulted in paradigms that involve clustering of bulky grids into smart self-adequate microgrids that changes their borders to keep load-generation balance at different operating scenarios. In addition, the planning of new microgrids should consider the type of the microgrid as a design variable with the emerging dc distribution paradigms. As well, a new analysis tool that considers branch-based load flow is required to facilitate the operation of the microgrids clustered from an existing distribution system in addition to the newly planned ones. This tool should have the following features:

- Simple and fast to fit the distributed controllers' capabilities.
- Capable of handling different microgrid modes of operation.
- Suitable for both solely-ac and hybrid microgrids.

1.2 Research Objectives

This research work in general aims at enabling the smart grid through introducing the concept of clustering the distribution system into adaptive self-adequate microgrids. Such microgrids would be

capable of operating in connected mode or isolated mode without affecting the load-generation balance. However, to achieve the proposed operation philosophy, numerous elements need to be addressed and fully studied. Initially, an accurate probabilistic modelling for renewable-based DGs and loads is a prerequisite for precise evaluation of self-adequacy of the distribution system. On the other hand, the increasing interest in dc distribution and the widespread use of dc loads and renewable-based DGs necessitate the optimum planning of new microgrids layout, whether ac or dc, while maintaining the self-adequacy and considering the probabilistic nature of DGs and loads. Moreover, load flow analysis tools with specific features are needed for steady-state and dynamic studies required for the successful operation of microgrids. In order to address these challenges, the main objectives of this research can be briefed as follows:

1. Developing a criterion to determine the borders of microgrids. This criterion will be used to cluster the existing bulky grid into distributed self-adequate microgrids. In addition, the borders of constructed microgrids will be kept flexible and dynamic in order to adopt any variation in the operating conditions.
2. Determining the efficient number and best locations of candidate interconnection buses that should be available to allow dynamic and flexible microgrid borders.
3. Developing probabilistic models for renewable-based generation and loads that are capable of accurately describing their variability and integrating these models with the load flow tools to form a probabilistic load flow analysis tool that will be used for the operational planning study.
4. Studying the optimum distribution system configuration that minimizes the investment and operational cost for new distribution systems or existing distribution system extensions. In this study, determining the cluster type (whether ac or dc) and selecting the ICs size (when needed) is essential to completing the planning process. It is crucial for this type of planning to determine the optimum supply mix to achieve the self-adequacy of the distribution system. The loads and generations of the distribution systems should be represented by their probabilistic models. Moreover, the size of the energy storage and/or capacitor banks are calculated if needed to achieve this self-adequacy operational constraint.
5. Developing a branch-based load-flow algorithm that precisely computes the steady-state system operation for islanded ac and hybrid ac-dc microgrids to facilitate the operation philosophy of the distribution system as interconnected microgrids.

1.3 Thesis Organization

The remainder of this thesis is organized as follows:

Chapter 2 presents the essential background and critical survey of previously directed studies for both ac and dc microgrids, the correlation between smart grid and microgrids, and the analysis tools for microgrids.

Chapter 3 introduces the probabilistic models for renewable-based DGs and load. It then explains their integration with the conventional branch-based load flow and the application of the Monte Carlo Simulation (MCS) to form the probabilistic load flow tool needed for the existing distribution system's operational planning study.

Chapter 4 explains the proposed philosophy for clustering the existing distribution system with its available resources into adaptive self-adequate microgrids and their philosophy of operation as building blocks for enabling smart grids. The framework is applied to an existing distribution system that has its own DGs in order to identify the building clusters (which facilitate the formation of self-adequate microgrids at different operating scenarios) and determine the corresponding minimum boundary buses.

Chapter 5 provides a planning framework that can be used to construct new distribution systems that consist of clusters of self-adequate microgrids. This framework can also be used for extending an existing distribution system. It performs an optimum system configuration analysis for the planning of new distribution systems as isolated microgrids to select the type of microgrid (i.e., ac or dc) and size the supply mix to achieve self-adequacy, taking into consideration the probabilistic nature of renewable-based generation and load. This optimal layout is based on proposing a planning framework to minimize the levelized investment and operation cost in consideration of various system constraints, especially those related to power balance.

Chapter 6 presents the development of a branch-based load flow algorithm for islanded ac microgrids to enable the operation of the clustered microgrids. The proposed algorithm overcomes the challenges associated with the absence of a slack bus and presents a novel handling of reactive power share between $Q-V$ droop-regulated DGs. As a branch-based technique, the algorithm is efficient for distribution systems with high R/X ratio while being fast, simple and less computationally extensive compared to derivative-based techniques. The proposed planning for new distribution systems considers the type of microgrid as a decision variable, and thus the distribution system is formed from

hybrid ac-dc microgrids. Therefore, the load-flow algorithm is then extended to incorporate the case of hybrid isolated microgrids to form a unified load flow tool for steady-state analysis of microgrids, either solely ac or hybrid ac-dc.

Chapter 7 describes the conclusions and contributions of the research presented in this thesis and recommends directions for future work.

Chapter 2
Background and Literature Review

2.1 Introduction

The objectives of this research, along with the motivations that prompted the work and an overview of the thesis' organization, are presented in Chapter 1. This chapter introduces the important insights into the required background. The material here primarily concerns the literature survey related to the stated research objectives. First, the probabilistic models for load and renewable-based generations are reviewed, since they are the cornerstone for most of the power system studies. In view of the focus of this work, a general background about microgrids and their operation scenarios is provided. Afterwards, challenges that face the practical implementation of microgrids are surveyed to provide an information base for the ongoing research in the area of microgrids. Furthermore, as this work sheds more light on the islanded microgrids, a survey is presented to address the common control technique for DGs and energy storage and their cooperation strategies during islanded mode of operation. Adding dc laterals to the existing distribution system with the system capability of islanding and operating as a microgrid during emergencies created a novel hybrid paradigm and presented different operation modes, as explained in this chapter. In addition to ac and hybrid microgrids operation research, this survey will review common steady-state analysis tools and their pros and cons when these tools are practically implemented.

2.2 Modelling of Load and Renewable Resources

Renewable-based energy sources are gaining increased interest due to their numerous benefits for both customers and utilities. In addition, the keen public awareness about the environmental impacts of electric power generation added to the renewable energy eminence due to their green effect on the environment [16]. However, the integration of DGs to the distribution network is a challenging task, as they may have negative impacts and many technical difficulties. These include adverse effects on power quality [17], impacts on power system reliability [18], [19], and complexities related to power system protection coordination [20], [21].

Fortunately, many of the extensive studies have been conducted to maximize the gained benefits from DGs while minimizing negative impacts on the distribution network via the optimal allocation and sizing of the capacities of DGs [22]-[25]. One key element in all the existing studies related to renewable DGs is the type of model used to represent the random behavior of their output power and the way in which these models treat the high probabilistic nature of wind speed and solar irradiance. There is no single and distinctive model commonly used for load and renewable resources. Instead, different methodologies are adopted to model the load and renewable resources random behavior. Thus, the obtained models are based on the application and type of analysis to be performed. These methodologies are generally categorized into two classes:

- Chronologically, using time-series techniques.
- Probabilistically, using a probability density function.

Hence, this section discusses different methodologies used to model renewable-based DGs (here, specifically wind and solar) in addition to load models.

2.2.1 Wind-based Resources Modelling

Recently, wind power became a salient component of the energy mix as an alternate for coal-based generation to reduce emissions and achieve the transition to a low-carbon economy. Currently in Ontario, there are 2,465 wind turbines, with an installed capacity of 4.781 GW. These facts indicate that wind-based generation is an important renewable source of energy. Thus, a precise model for the wind output power is crucial for power system studies and operations. The following subsection describes the commonly used models for wind renewable resources.

2.2.1.1 Wind speed modeling using probability density function

This approach is usually used in planning applications. The wind speed in the model is represented with a suitable PDF. The most common PDF used to model wind speed is the Weibull distribution (2.1) [26].

$$f(x) = \frac{k}{c}\left(\frac{v}{c}\right)^{k-1} e^{\left(-\left(\frac{v}{c}\right)^{k}\right)} \tag{2.1}$$

The parameters of the PDF (i.e., k and c) are approximately calculated from historical data using average wind speed and standard deviation, as presented in (2.2-2.5).

$$k = \left(\frac{\sigma}{v_m}\right)^{-1.086} \tag{2.2}$$

$$c = \frac{v_m}{\Gamma\left(1 + \frac{1}{k}\right)} \tag{2.3}$$

$$v_m = \frac{1}{n}\left(\sum_{i=1}^{n} v_i\right) \tag{2.4}$$

$$\sigma = \sqrt{\frac{1}{n-1}\sum_{i=1}^{n}(v_i - v_m)^2} \tag{2.5}$$

The Weibull distribution is used to model wind speed for certain location over specific periods of time. Generally, annual wind speed distribution is used.

2.2.1.2 Time series method for wind speed modeling

In this chronological model, wind speed is expressed as a function of preceding values and the model is comprised of a sequence of data points equally spaced in time. The auto regression moving average (ARMA) method can be used to obtain the wind speed model. This ARMA(p, q) modelling approach can be divided into two modules – the AR(p) module, which relates wind speed to data from preceding hours, and the MA(q) module, which introduces the noise via a normally distributed random variable. Historical wind speed data are used to calculate the model parameters and generate the hourly wind speed throughout the simulated year. With the hourly observed wind speed ($v_{ob,t}$) , wind speed mean (μ_t) and standard deviation (σ_t) are used to calculate $v_t$as expressed in (2.6). The obtained $v_t$is then used to calculate model parameters using (2.7). Finally, the estimated hourly speed ($v_{est,t}$) is calculated using (2.8)

$$v_t = \frac{v_{ob,t} - \mu_t}{\sigma_t} \tag{2.6}$$

$$v_t = \sum_{i=1}^{p} \alpha_i \, v_{t-i} + e_t - \sum_{i=1}^{q} \theta_i \, e_{t-i} \tag{2.7}$$

$$v_{est,t} = \sigma_t \, v_{ob,t} + \mu_t \tag{2.8}$$

2.2.1.3 Wind-based generator output power

A wind turbine with a coupled generator will convert wind energy into electrical output power. Hence, the equations of that wind energy conversion system (WECS) are used to convert wind speed into output power. The output power depends on the efficiency and the output of the wind energy generation

subsystems (i.e., aerodynamic, mechanical, or generator subsystem). However, the overall WECS power curve that relates output power to wind speed can be approximated to be linear [27]. This conversion is obtained with the knowledge of the wind turbine's manufacturing data: rated power P_{rated}, cut in speed v_{ci}, cut out speed v_{co}, and rated speed v_r. This complete modelling process is shown in Figure 2.1.

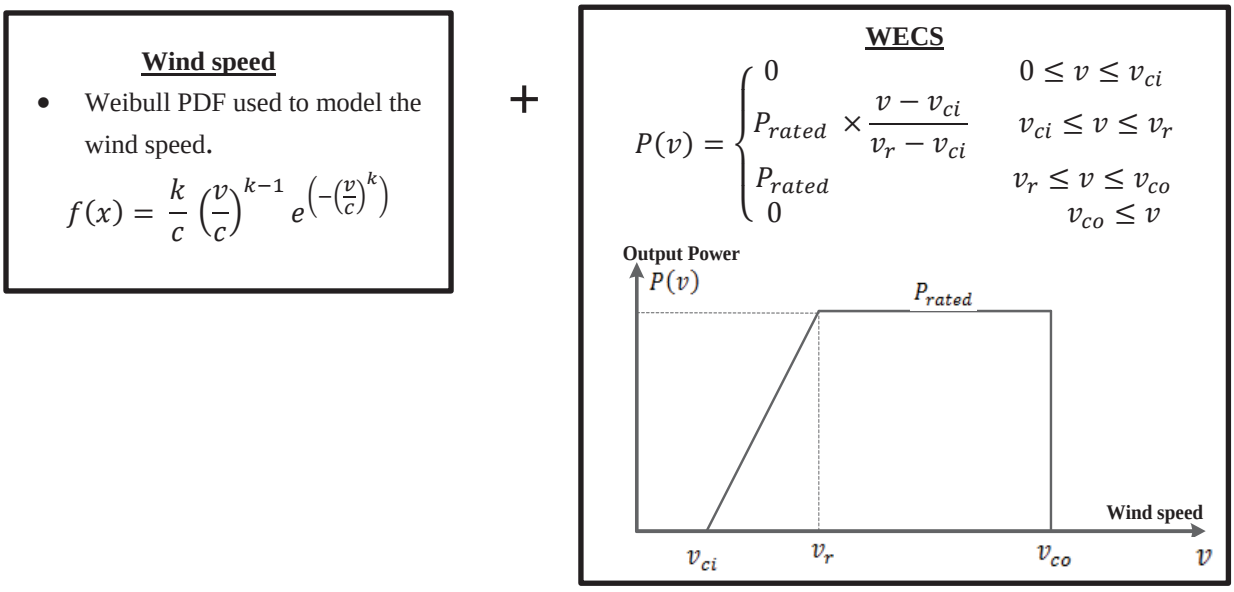

Figure 2.1: Modelling stage of wind-based generator output power.

The combination of wind speed and WECS characteristics results in a PDF for the wind output power that has two concentrations: one at low speed and one at high speed. This PDF is different from the Weibull PDF, which has low probability at both ends. Hence, the power output is a mixed random variable that is continuous between values of zero and rated power, and discrete at values of zero and rated power output [28]

2.2.2 Solar-based Resources Modelling

Although wind-based resources dominate renewable technologies connected at the transmission system level, solar-based resources are dominating at the distribution system level. In Ontario, according to Independent Electrical System Operator (IESO) published data, 1947 MW of solar are installed at the distribution system compared to 561.8 MW of wind [29]. This increased existence of solar-based generation heightens the need for an accurate model that appropriately represents the probabilistic behavior of the output power of these generators. The best method for converting solar energy into electricity is photovoltaic (PV) modules.

Similar to wind, the solar model consists of two stages. The first stage represents solar irradiance, and second stage PV energy conversion. Solar irradiance is usually modelled using a bimodal distribution function, so the data are grouped into two divisions, each of which is represented by a unimodal distribution function [30] . The typical irradiance data shown in Figure 2.2 explains the phenomenon of dividing solar irradiance into two groups.

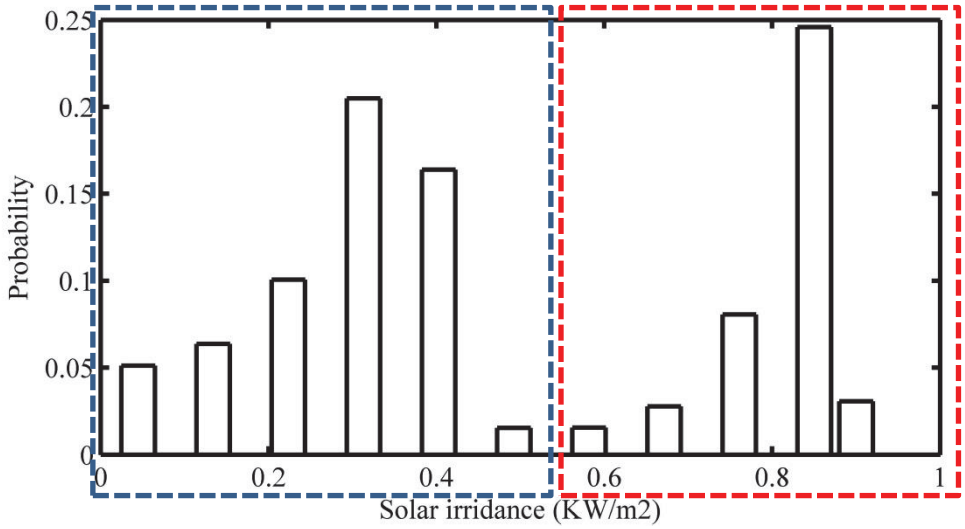

Figure 2.2: Histogram for typical solar irradiance data.

Beta PDF is broadly used to represent solar irradiance for each modal. Hence, the model is comprised of two beta PDFs, one for each group. The beta PDF equation as presented in (2.9) has two parameters: α and βc. These model parameters are calculated from solar irradiance historical data using their average (μ) and standard deviation (σ), as described in (2.10) and (2.11).

$$f(x) = \begin{cases} \dfrac{\Gamma(\alpha+\beta c)}{\Gamma(\alpha)\Gamma(\beta c)}\, x^{(\alpha-1)}(1-x)^{(\beta c-1)} & for\ 0 \le x \le 1, \alpha \ge 0, \beta c \ge 0 \\ 0 & Otherwise \end{cases} \tag{2.9}$$

$$\beta c = (1-\mu)\left[\frac{\mu(1+\mu)}{\sigma^2} - 1\right] \tag{2.10}$$

$$\alpha = \frac{\mu\, \beta c}{1-\mu} \tag{2.11}$$

The solar energy is converted to electrical energy through the PV modules that absorb photons from solar radiation and provide dc power. Usually PV modules are connected in an array of series and parallel connections to provide the required current and voltage, respectively. A typical characteristic

of a single PV module is shown in Figure 2.3 at a specific level of radiation and ambient temperature. The PV module characteristic has parameters such as a short-circuit current (I_{sc}), open-circuit voltage (V_{oc}), current at maximum power point (I_{MPP}), voltage at maximum power point (V_{MPP}), and nominal operating temperature (N_{OT}). Typically, PV modules are operated at their maximum power point (MPP) through a MPP tracker that ensures the operation at or close to this point at different weather conditions. The short circuit current is a function of the solar irradiance and the voltage is a function of the temperature. The modelling stage of solar-based DG output is shown in Figure 2.4, which combines the solar irradiance PDF with the PV module characteristics to calculate the output power.

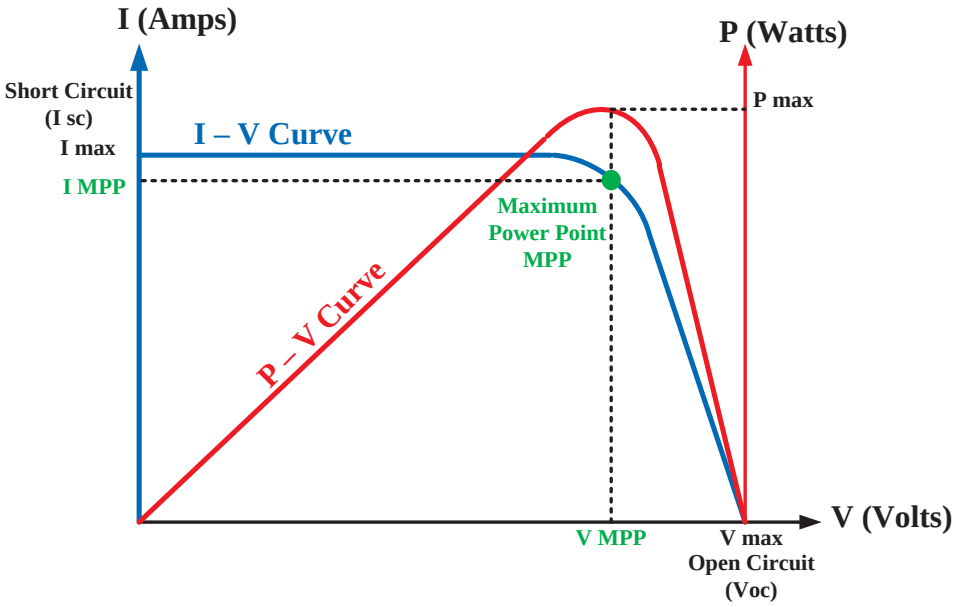

Figure 2.3: Typical characteristics of PV module.

Solar irradiance

Beta PDF used to model the solar irradiance.

$$\frac{\Gamma(\alpha+\beta c)}{\Gamma(\alpha)\Gamma(\beta c)}\, x^{(\alpha-1)}(1-x)^{(\beta c-1)}$$

+

PV Module characteristic

$$T_C = T_A + I_\beta\left(\frac{N_{OT}-20}{0.8}\right)$$

$$I = I_\beta[I_{SC} + K_i(T_C - 25)]$$

$$V = V_{OC} - K_v T_C$$

$$P = N\left(\frac{V_{MPP} I_{MPP}}{V_{OC} I_{SC}}\right) V\, I$$

Figure 2.4: Modelling stage of solar-based generator output power.

2.2.3 Load Modelling

IEEE reliability test system (IEEE-RTS) [31] data are usually used as benchmarking historical load data. The system presents daily load profiles for one year as a percentage of the yearly peak load. The data are constructed from tables for the weekly peak as a percentage of the yearly peak (for 52 weeks), and the daily peak as a percentage of the weekly peak. The hourly peak is a percentage of the daily peak. These tables are used to generate the 365 daily profiles shown in Figure 2.5 that represent one year. The numbers from (1-6) show the candidate grouping for the data into six clusters which share the same behavior.

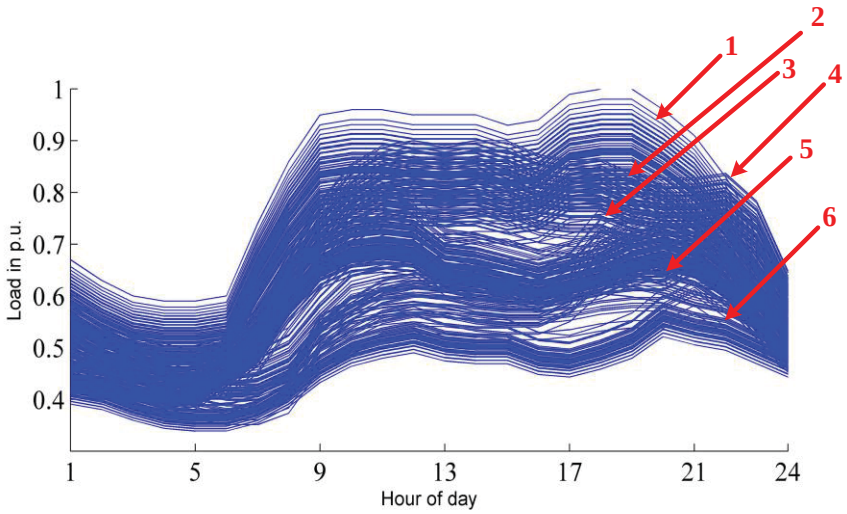

Figure 2.5: IEEE-RTS daily load profiles with six candidate clusters for data.

One approach in modelling the load is to cluster the load profile into the proper number of clusters. As shown in Figure 2.5, the load profiles can be grouped into six clusters. Another approach is to divide the annual load into a number of levels and find the probability of each load level. The histogram for the IEEE-RTS data is presented in Figure 2.6, which shows the load level and its probability.

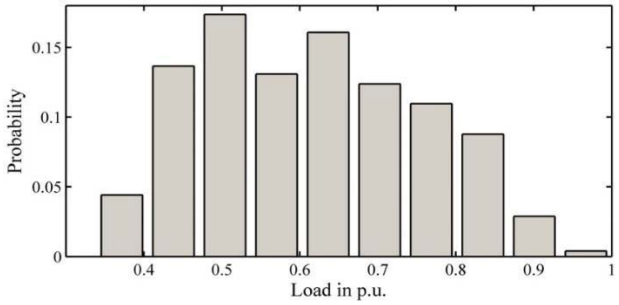

Figure 2.6: Histogram for load levels and their probabilities.

2.3 Smart Grids and Microgrids

A smart grid is a modernized grid system that manages electricity demand in a sustainable, efficient, secured, reliable and economic means. Smart grids are constructed on an advanced infrastructure and are planned to facilitate the integration of all involved technologies. Smart grids allow bi-directional energy flows and utilize two-way communication and control abilities which will lead to a series of novel functionalities and uses. As illustrated using the conceptual model for a smart grid shown in Figure 2.7, smart grids rely extensively on communication infrastructure and use advanced sensors, two-way communications, computational ability and control in order to enhance the overall functionality of the electric power system [32].

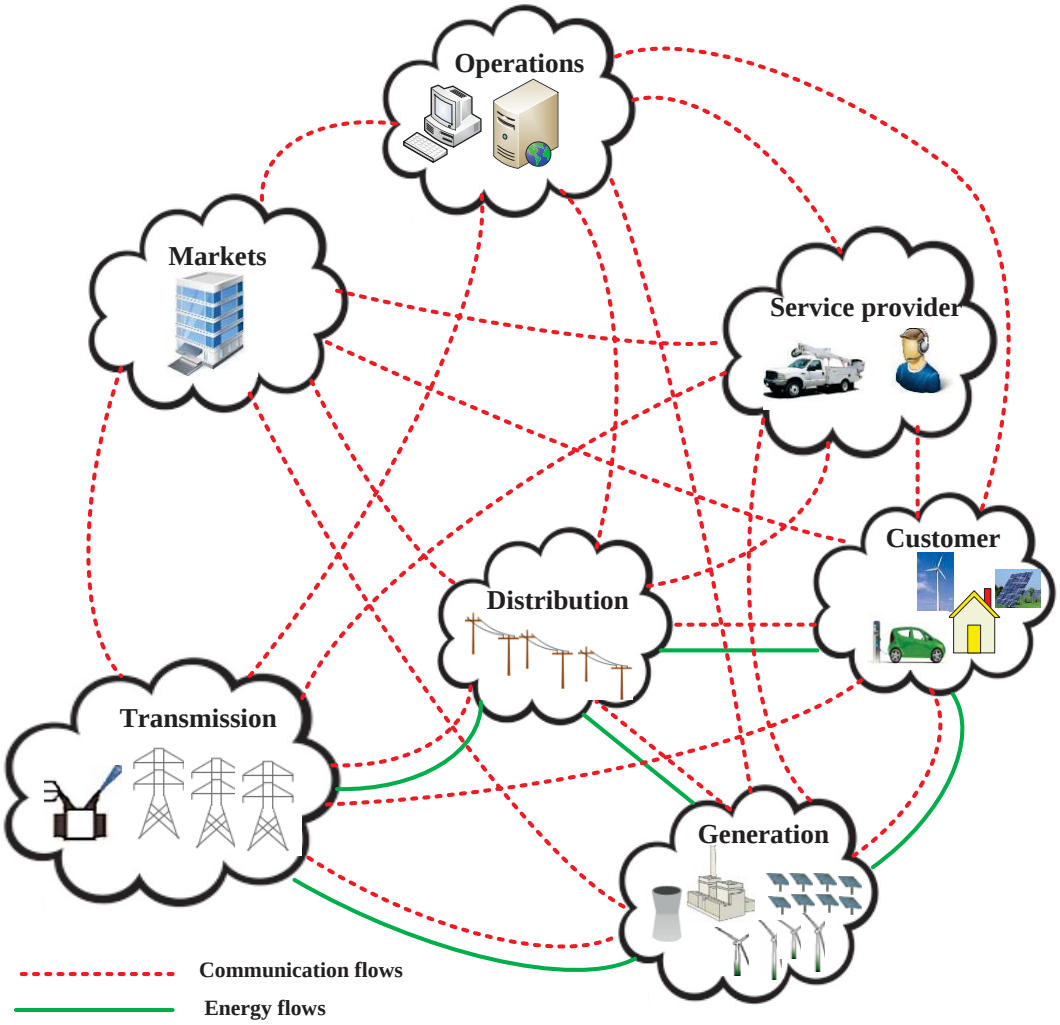

Figure 2.7: Conceptual model for smart grids [33].

The key differences between smart grids and conventional grids can be summarized as shown in Table 2.1 [34] .

Table 2.1: Key Differences Between Smart Grids and Conventional Grids

Conventional grid	**Smart grid**
Electromechanical relays	Digital relays
One-way communication	Two-way communication
Centralized and bulky generation	Distributed generation
Minimum sensors	Widespread sensors
Manual monitoring	Self-monitoring
Manual restoration	Self-healing
Blackouts	Islanding
Manual check	Remote check
Limited control	Expanded control
Limited customer choice	Flexible customer choice

2.3.1 Microgrid Definitions and Benefits

Where there is no unique definition for a microgrid, the following are some common definitions in the literature:

- "A microgrid comprises low voltage distribution systems with distributed resources, such as PV power systems and wind turbines, together with storage devices. These systems are interconnected to the medium voltage distribution network. But they can also be operated isolated from the main grid."[35]
- "A microgrid is a cluster of interconnected distributed generators, loads and intermediate storage units that co- operate with each other to be collectively treated by the grid as a controllable load or generator. Power quality events and pre-set conditions will make the microgrid disconnect from the main grid and operate as a separate island."[36]
- "A microgrid is a cluster of loads and micro-sources operating as a single controllable system that provides power to its local area."[37]
- "Microgrids are power systems in which generation elements are co-located with loads, regardless of the aggregated generation capacity or the grid interconnection."[38]

The common microgrid characteristic across these definitions is that a microgrid is controlled as a single entity and has co-located power generation sources, energy storage elements, and end-use loads. However, the discrepancy is the definitions mainly concerns the total rating of generation units within the microgrid and whether the interconnection to the main grid is done through single or multiple points. Enabling microgrids is achieved by solving the technical challenges associated with their practical implementation and is believed to facilitate the transition from conventional grid to smart and efficient grid. Moreover, adopting microgrids as the building units for a power system implies various benefits such as:

- For end-users:
  - Improves reliability and power quality.
  - Reduces average energy cost.
  - Supports restoration of supply after contingencies.
  - Enables high penetration level of renewable energy sources.
- For the utility:
  - Deferral of new transmission infrastructure.
  - Loading relief of existing transmission system.
  - Support for electrical network in remote sites and rural areas.
  - Helps to achieve self-adequacy through controlling local load and generation.
  - Provides ancillary services, such as voltage support and demand response.
- For the environment:
  - Emissions are significantly reduced, especially greenhouse gases, due to increased dependence on renewable resources in microgrids.
  - Defers the need for new rights on how to build transmission lines.

2.3.2 Microgrid Operation Modes

Microgrids, as per their definition, are controlled as a single entity for improved reliability and flexibility and thus should be able to operate in the following differing modes of operations:

2.3.2.1 Isolated (islanded) mode of operation

In this mode of operation, the microgrid is operated as a standalone and self-adequate grid with zero active and reactive power interchange with the main grid, as shown in Figure 2.8. In order to achieve self-adequacy, the energy storage units may be used or alternatively load shedding of noncritical loads may be applied. In this mode of operation, a microgrid has no slack bus and energy resources have to share the microgrid load. Therefore, in this situation, the dispatchable energy resources are usually droop-controlled.

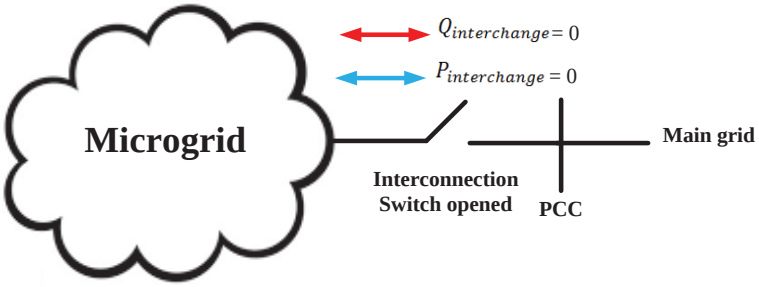

Figure 2.8: Microgrid isolated mode of operation.

2.3.2.2 Grid-connected mode of operation

In this mode of operation, the microgrid is connected to the main grid in order to import or export energy, as shown in Figure 2.9. The main grid will act as a slack bus for the microgrid and can supply any power mismatch between generation and load. The complexity of interconnecting the microgrid to the main grid depends on the types of energy generation units within the microgrid, the level of penetration (which represents the amount of allowable energy interchange between the microgrid and main grid), and the location and number of interconnecting nodes.

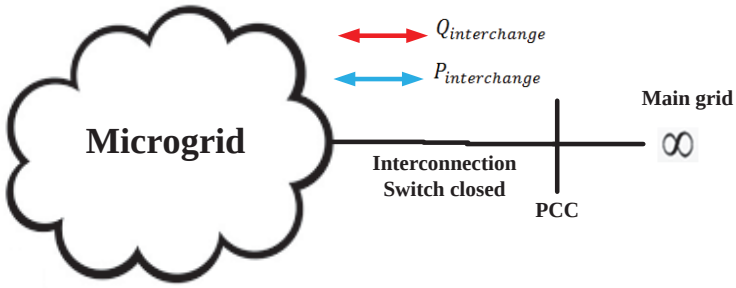

Figure 2.9: Microgrid grid-connected mode of operation.

However, increasing the level of penetration can negatively affect both the microgrid and the main grid. If the microgrid exports/imports power to the main grid and a contingency occurs there, the microgrid will disconnect and be transferred to isolated mode to protect itself, which may increase the impact on the main grid due to losing a considerable generation/load capacity. Moreover, when a microgrid with initial high penetration level or renewable energy resources is isolated from the main grid (importing/exporting), the generation-load imbalance is significant and hence frequency oscillations and instability of the microgrid may take place, which requires fast action of the controller to shed non critical loads and reduce generated energy in order to maintain the stability of the islanded microgrid. On the other hand, a microgrid can provide ancillary service to the main grid by injecting reactive power, Q, to support the grid voltage and supply active power, P, to help the generators to

achieve black start and present a reserve power for the utility through the storage units within the microgrid.

2.3.2.3 Microgrid-to-microgrid interconnected mode of operation

In this mode of operation, multiple microgrids are connected together in order to increase reliability, power supply quality and system stability as well as reduce average energy costs by utilizing ultimate benefits from renewable resources. This is achieved by operating these resources at MPP and import/export excess energy with other microgrids or storing it locally. The interconnected mode of operation (microgrid-to-microgrid) layout for n microgrids is shown in Figure 2.10. The interconnected mode is still a challenging task, as it is not investigated in the published research work in the microgrid area, even though this mode of operation will allow a secure and reliable operation of the microgrid.

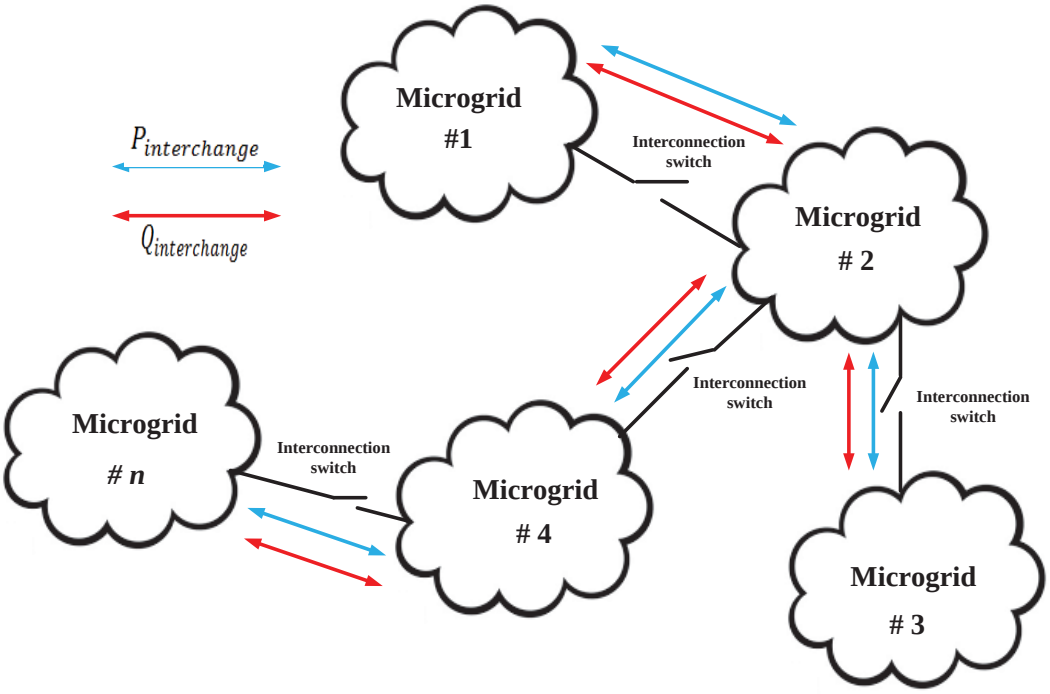

Figure 2.10: Microgrid interconnected mode of operation.

2.3.3 Challenges to Microgrid Implementation

There are several challenges facing the implementation of microgrids. This section discusses the common challenges listed in the literature.

2.3.3.1 Multiple modes of operation

Microgrid components should support multiple modes of operation (grid-connected, interconnected and isolated modes of operation). In addition, the transition between different modes of operation should be fast and seamless, and hence the control for transition should be applied at the device level in order to achieve this fast transition. However, some existing inverters are used to interface DGs to the microgrid to support only one mode of operation, which presents a challenge to the microgrid operation. For example, the inverter used to interface energy storage to microgrid should operate in current mode during grid-connected microgrid mode and in voltage mode during islanded microgrid [39], [40].

2.3.3.2 Protection of new microgrids or protection of upgraded microgrids

The microgrid protection scheme should be able to differentiate between internal and external faults during different operation modes in order to have high selectivity. The challenge is setting the protection devices to ensure high sensitivity and selectivity with changeable short-circuit levels, as the short-circuit level during isolated mode is significantly lower than that during grid-connected mode. This is due to the fact that inverter-based DGs have lower short-circuit levels compared with machine-based DGs. However, in order to solve this problem, the relay settings should be capable of being adjusting during different operating modes, which requires a fast, reliable, and cost-effective communication link [41].

2.3.3.3 Regulatory policies

Regulation barriers and policies placed by network operators on the interconnection and operation are carried out mainly for DG units. These policies should be reformed to consider the microgrids as one entity, which requires additional modifications and studies to keep up with the increased interest in microgrid interconnections. In addition, the optimization between seamless islanding during disturbances and the low voltage ride-through required by the grid are challenging tasks that also need further study. On the other hand, the grid operator definition for the microgrid at the point of common coupling (PCC) significantly affects the operation and control of microgrids under different market policies. Microgrids at the PCC can be defined according to different market policies as:

- “Good citizen”: with this definition, the microgrid is allowed only to import power from the grid. No reactive power import or export with the grid is permissible in this case and

thus the microgrid is considered as a unity power factor variable load, which represents the preferred situation for the upstream network operators.

- "Promise-keeping good citizen": This indicates that the microgrid is a good citizen but provides a forecast for the load on a day-to-day basis.
- "Flexible good citizen": This indicates that the microgrid is a good citizen that keeps the voltage at PCC constant by exchanging reactive power with the main grid.
- "Ideal citizen": This indicates that the microgrid contributes to the energy market by selling/buying active/reactive power to the main grid. In this mode, the reversible power flow should be allowed and the protection scheme should be modified to allow the reverse power flow.
- "Docile citizen": If the main network owns the DGs operated in the microgrid, the network operators have full control over all microgrid components.

2.3.3.4 Challenges during isolated mode of operation

The challenges facing the operation of microgrids in isolated mode with no access to the main grid are summarized as follow [36] :

- Voltage and frequency control: After islanding, the control of voltage and frequency is no longer achieved by the main grid. So, it needs to be controlled by the primary or intermediate energy sources within the microgrid to avoid voltage collapse or large frequency deviations.
- Self-adequacy: After islanding, the microgrid should be able to achieve balance between the energy generated and the load. If the microgrid was initially importing power from the grid, non-critical loads will be shed after islanding unless the microgrid has sufficient stored energy. However, if the microgrid was exporting power, the output power from the DGs should be reduced. Unless these DGs are renewable, it is recommended to store the excess power to maximize the power collected from the resources.
- Power quality: During the islanding operation, the microgrid has to maintain an acceptable power quality level. In addition, there should be a sufficient supply of active and reactive power to support the frequency and voltage of the microgrid. Also, the microgrid has to be capable of supplying the non-linear currents required by non-linear loads.

2.3.4 Common Control Techniques for DGs and Energy Storage Units

Several control techniques are used for DG units and ESS to ensure proper load-sharing and avoid overloading. The selection of the appropriate control technique depends on the system mode of operation. This section reviews common control techniques reported in the literature.

2.3.4.1 PQ control

In this type of control, the inverter used to interface either the DG or the ESS can act as a current controlled voltage source. The inverter control is used to inject certain active and reactive power into the microgrid. The set value of P and Q (reference values to the controllers) are sent from the supervisory central controller of the microgrid. A block diagram of the PQ control scheme for inverter-interfaced DG or ESS is shown in Figure 2.11[36], [42]. For steady state analysis, this PQ-controlled DG or ESS can be considered as constant PQ elements with set values.

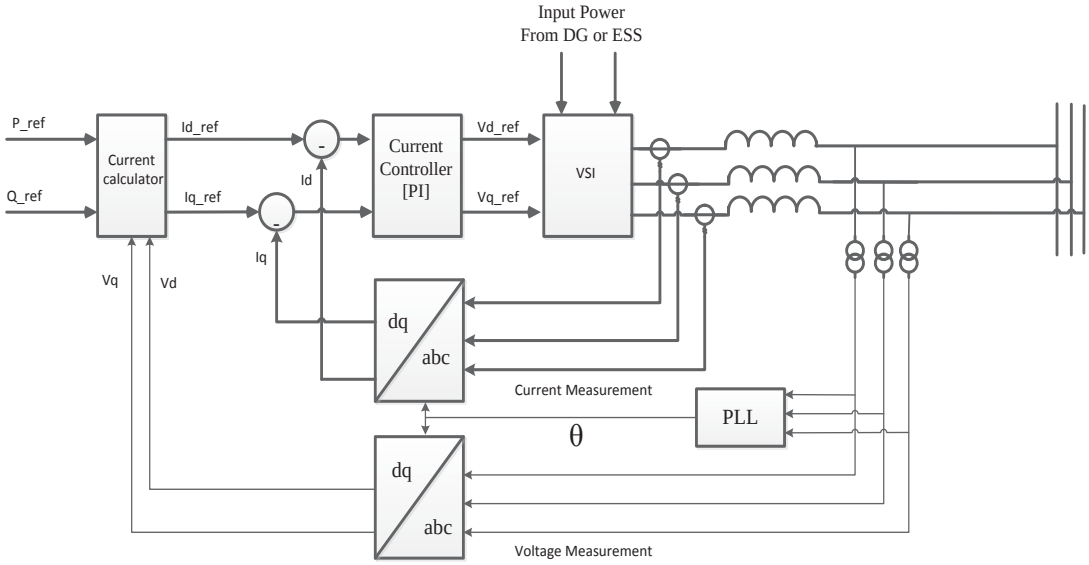

Figure 2.11: PQ control of inverter-interfaced DG or ESS.

2.3.4.1 Droop control

The droop control technique used with conventional bulky generators for many years is utilized in the distribution system. Droop control allows DG and ESS to share loads without being overloaded and without communication, as the system frequency is used in setting the output

power which is common for the microgrid [43]–[47]. A block diagram of a droop control scheme for inverter-interfaced DG or ESS is shown in Figure 2.12 [43]. For transmission systems, X/R ratio is large and hence the resistance of the lines is neglected. The power flow equations can be expressed as in (2.12) and (2.13).

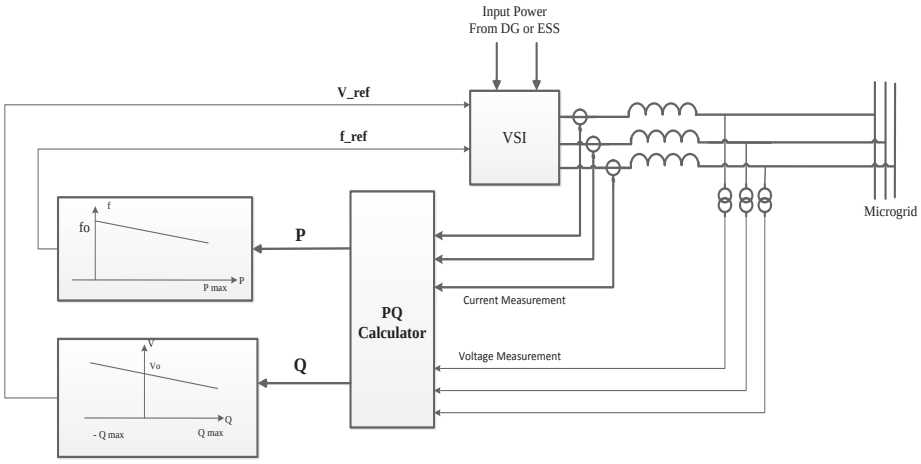

Figure 2.12 : Block diagram of droop control for inverter-interfaced DG or ESS.

$$P = \frac{V_1 V_2}{X} \sin \delta \tag{2.12}$$

$$Q = \frac{V_1^2}{X} - \frac{V_1 V_2}{X} \cos \delta \tag{2.13}$$

However, δ is usually a small angle and thus the previous equations can be simplified to the following equations:

$$\delta \cong \frac{X\,P}{V_1 V_2} \tag{2.14}$$

$$V_1 - V_2 \cong \frac{X\,Q}{V_1} \tag{2.15}$$

From (2.14), it is clear that the angle δ and hence the frequency depends on the active power flow. In addition, from (2.15), the voltage difference depends on the reactive power flow, so that the control of active and reactive power will control the system voltage and frequency. This concept is implemented using the droop control, which controls active and reactive power to regulate the system voltage and frequency according to Equations (2.16) and (2.17), respectively. $Q - v$ is shown in Figure 2.13 [47].

$$\omega = \omega_o - K_p\,P \tag{2.16}$$

$$V = V_o - K_v Q \tag{2.17}$$

The parameters of these droop relations are determined based on the rated active and reactive power and allowed frequency deviation (Δf) and voltage deviation (Δv). The relation between $P-f$ and $Q-v$ is shown in Figure 2.13.

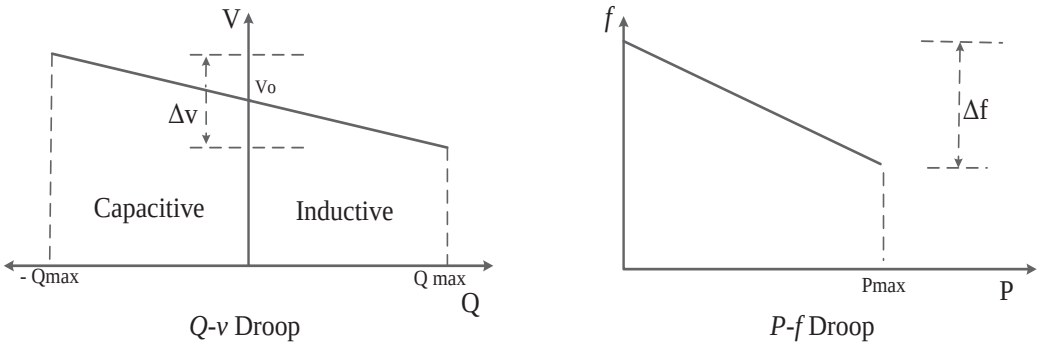

Figure 2.13: $P-f$ and $Q-v$ droop control of inverter interfaced DG or ESS.

2.3.4.2 PV control

In this type of control, the active power and the voltage at the PCC are used as feedback signals to generate the control reference signals. As a result, the DG controls the voltage at the PCC; it also controls the frequency by balancing the active power. Figure 2.14 shows the block diagram for the PV control [48].

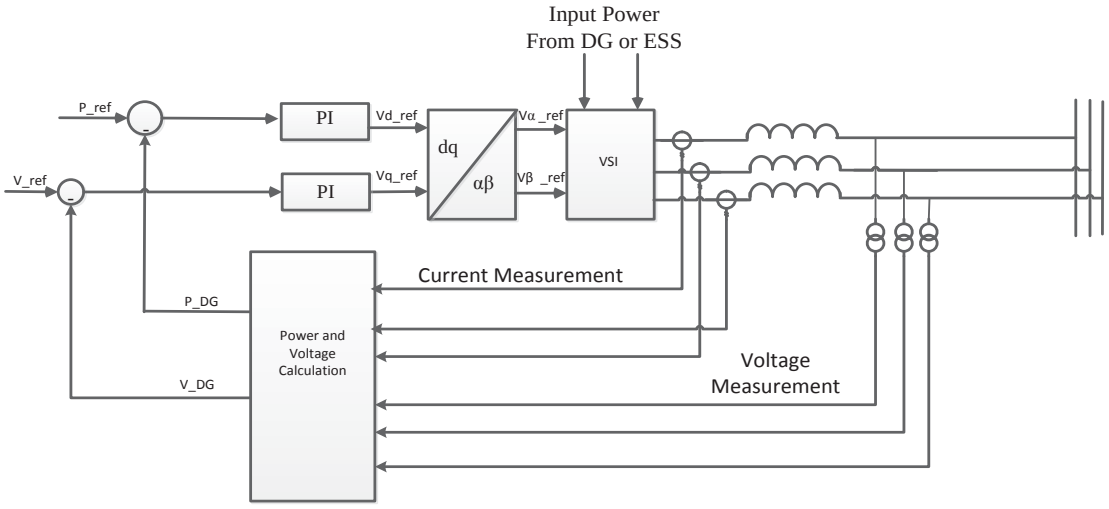

Figure 2.14: PV control of inverter-interfaced DG or ESS.

2.3.5 Cooperation Control Strategies Between DGs and ESS for Islanded Microgrids

Many cooperative control strategies are presented in the literature to coordinate the operation of DGs and energy storage. These strategies define the control techniques used to control DGs and ESS during island and grid-connected modes of operation. Non-dispatchable DGs are assumed to have maximum power controllers and operate at their maximum output power [36]. The cooperative strategies can be categorized as follows:

I. Pure droop control

For this control strategy, the storage devices and all DGs are capable of switching from PQ control during the grid-connected mode of operation to droop control during the islanded mode of operation, and hence controlling the voltage and frequency of islanded microgrids. This cooperation strategy requires no communication links between different DGs and storage units [49].

II. Single master operation SMO

During island mode, the energy storage device moves to droop control while all other DGs remain in PQ control. However, the set point for the inverter's active power is calculated using a PI controller fed with the frequency of the network, whereas the set point for the inverter's reactive power is calculated using $Q - v$ droop. No communication links are required for this cooperation control strategy. If the DG has an internal storage device, it can cooperate in the voltage and frequency control by switching to the droop control, which is called multi-master operation (MMO) [50], [51].

III. Primary energy source control

During islanded mode of operation, the energy storage system (ESS) emulates the synchronous generator operation by performing secondary control action. As a result, the voltage and frequency of the microgrid are restored to their normal values before islanding. This is done by shifting the droop characteristics of the ESS until the microgrid restores the normal voltage and frequency V_0 and ω_0, respectively. This control strategy requires no communication links [52].

IV. Reverse droop control

In this control strategy, all DGs remain in the PQ control mode when the microgrid isolates, and only the energy storage shifts to the droop control. However, the droop control used with the energy storage is the reverse droop control due to the high R/X ratio of the LV distribution

system. Active power output is controlled to regulate the voltage ($P - v$ droop), while reactive power output is controlled to regulate the frequency ($Q - f$ droop) [53].

V. Autonomous control

This control strategy does not rely on a microgrid central controller or central ESS. Instead, each DG unit has an internal storage unit connected to its DC bus. This strategy allows the plug-and-play feature, so adding a new DG does not require any reconfiguration of the system. DGs are controlled using droop control in both the grid-connected and isolated mode of operation. During grid-connected operation mode, the output power from DGs is constant, as the voltage and frequency are set and kept constant by the grid [46].

VI. Intelligent agent-based PQ control

This strategy is based on keeping all DGs operating with PQ control in grid-connected and isolated modes of operation. In addition, the energy storage unit is operated with droop control to regulate the microgrid voltage and frequency and to achieve the balance between generation and load by acting as a load-following unit. Moreover, the set points for the DG's P and Q are sent from an intelligent agent and updated twice per minute, which means that this strategy needs a microgrid central controller. However, fast and reliable communication links are required to transfer set points. [54]

2.4 Hybrid AC/DC Microgrid

There has been renewed interest recently in DC distribution due to their enormous benefits offered for the integration of renewable-based DGs and modern loads. Thus, having a dc feeder as a part of the ac distribution system represents a promising topology. The hybrid distribution system will be formed from hybrid ac and dc subgrids with an interconnection point between the ac subgrid to the main grid and an isolation switch between the ac and dc subgrids. The layout of this recent topology is shown in Figure 2.15. The IC that connects ac and dc subgrids facilitates and manages energy interchange between both subgrids.

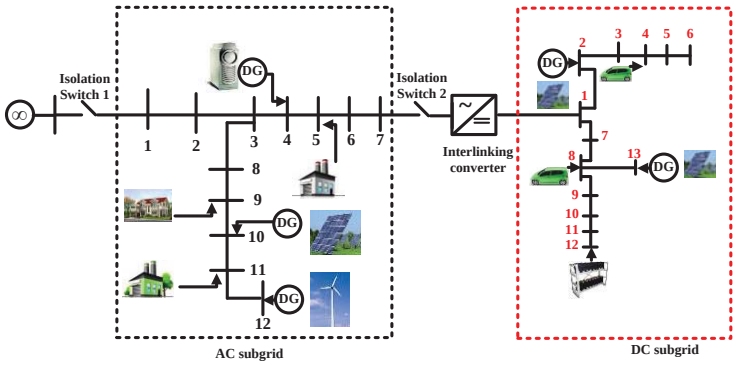

Figure 2.15: Layout of hybrid ac/dc paradigm.

2.4.1 Droop Control for DC DGs

The majority of DGs in microgrids use droop control to ensure reasonable load sharing without the need for communication. Similar to the ac droop, the dc droop relates the power injected to the locally measured variables at the DG bus, which in this case is the voltage. The dc droop equations are presented in (2.18) and (2.19) [55].

$$V_{dc} = V^* - K_{dc} P_{dc} \tag{2.18}$$

$$K_{dc} = \frac{P_{dc,max}}{V_{dc,max} - V_{dc,min}} \tag{2.19}$$

2.4.2 Operation Modes for Hybrid AC/DC System

The operation modes of the hybrid paradigm depend on the availability of the connection to the main grid and the installed generation capacities in ac and dc subgrids. These operation modes can be summarized as follows:

a) Grid-connected hybrid system:

In this mode of operation, a connection is available with the main grid. Thus, the ac subgrid can be considered stiff and can act as a slack bus to the dc subgrid, supplying any power mismatch between load and generation.

The system during this mode can be represented as shown in Figure 2.16. The ac and dc subgrids can be studied separately as each subgrid has a slack bus, and the conventional steady state analysis tools can be used for each subgrid.

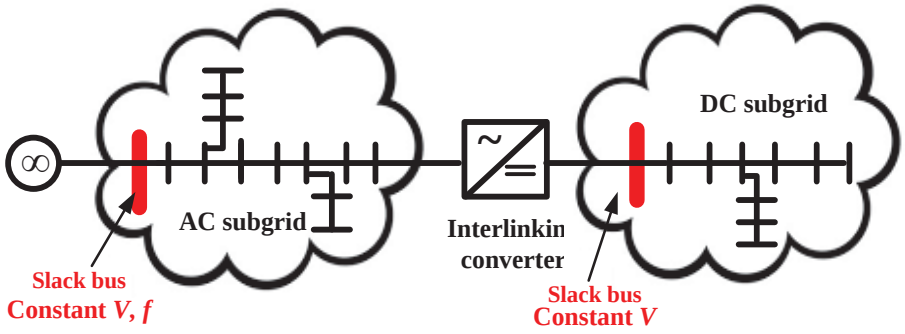

Figure 2.16: Schematic diagram for grid-connected hybrid system mode of operation.

b) Islanded hybrid system:

In this mode of operation, the connection to the main grid is lost, while the two subgrids are still intact. Several operation scenarios depend on the installed generation and storage capacities in each subgrid. These scenarios can be summarized as follows:

I. Islanded hybrid system with stiff ac subgrid [56]

In this scenario the ac subgrid has sufficient generation capacity to act as a slack bus to the dc subgrid, and thus the dc voltage is constant and regulated by the power injected from the ac subgrid. DGs in the dc subgrid will be operated as constant power while DGs in the ac subgrid will be droop-controlled to balance load and generation.

II. Islanded hybrid system with stiff dc subgrid [57]

Conversely, in this scenario, the dc subgrid has sufficient generation capacity to act as a slack bus to the ac subgrid. Thus, the ac frequency and voltage are constants and regulated by the active and reactive power injected from the dc subgrid. DGs located in the dc subgrid can be operated in the PV or PQ control mode, while DGs installed in the dc subgrid will be droop-controlled to balance system load and generation.

III. Islanded hybrid system with limited ac and dc capacities [58]

In this scenario, neither the ac subgrid nor the dc subgrid has sufficient generation capacity to act as a slack bus. Hence, the IC will link the dc voltage of the dc subgrid to the ac subgrid frequency to allow the resources in both grids to cooperate the sharing of the load. If the load in the dc subgrid rises, the dc voltage will drop, which reduces the frequency in the ac subgrid and increases the injected power in the ac DGs. Similarly, if the load in the ac subgrid rises,

the ac frequency will drop, reducing the dc voltage in the dc subgrid and increasing the dc DGs' injected power to support the DGs located in the ac subgrid. This scenario is the most feasible scenario with the current limited capacities of installed DGs. The layout of the hybrid system in this scenario is shown in Figure 2.17 [58], highlighting the characteristics of the ac subgrid, dc subgrid and IC. The ac subgrid can be represented with an equivalent droop-regulated ac DG. Similarly, the dc subgrid is represented by a droop-regulated dc DG. The IC function is to equalize the per-unit voltage of the dc subgrid to the per-unit frequency of the ac subgrid by managing the power exchange between both grids.

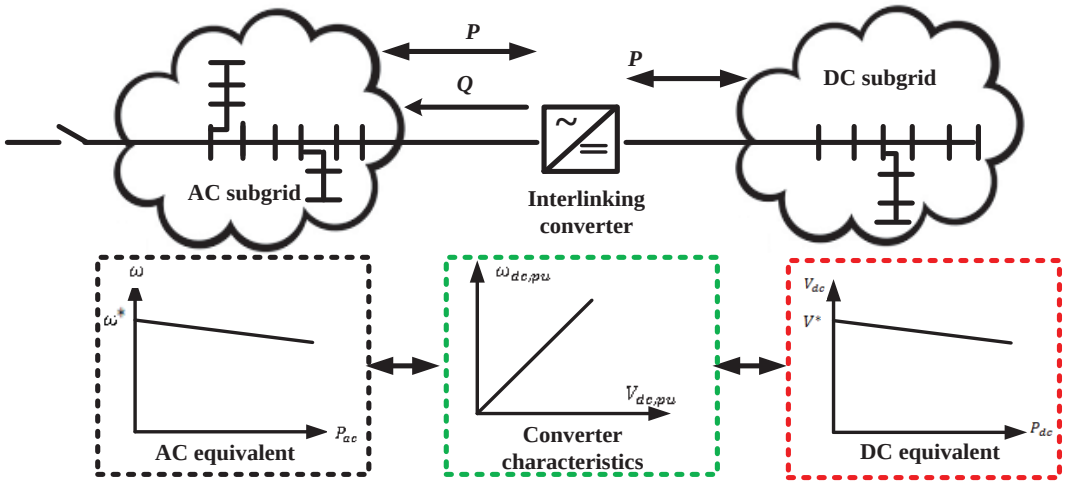

Figure 2.17: Schematic diagram for islanded hybrid system with limited ac and dc capacities.

c) Islanded and isolated hybrid system:

In this mode of operation, the connection to the main grid is lost and the two subgrids are isolated. The system is thus transferred to the islanded ac microgrid, and the islanded dc microgrid works independently.

2.5 Steady-State Analysis of Solely AC and Hybrid Microgrids

The steady-state analysis tool has been instrumental in the planning and operational studies of power systems. These studies range from the allocating and setting of protective devices to dynamic stability analysis. Islanded microgrids represent a challenge for the conventional steady state analysis tools due to their unique features, which are highly distinctive from traditional distribution systems. For instance, the absence of a slack bus is a challenging aspect of islanded microgrids, in addition to the various DG control techniques that need to be considered. Power flow analysis tools for islanded solely ac microgrids have been presented in multiple research work. In [59], Abdelaziz et al. presented a novel

load flow algorithm using the Newton-trusted-region (NTR) technique. The rationale behind the technique is to form the problem as a combination of the load flow equations and DG droop equations, and then to use a nonlinear equation solver to find the load flow. However, this technique is similar to Newtorn-Raphson (NR) in forming a matrix (the dogleg, in this case) and then calculating the inverse numerically. The computatiuonal time in this method is $O(n^3)$, which increases dramtically with the number of variables. Simliary, Mumtaz et al. in [60] proposed a modified NR-based algorithm for isalnaded ac moicrogrids. However, distribution systems have high R/X ratio which may hinder the convergence of NR-based techniques. Moreover, these techniques require the formulation and inversaion of a Jacobian matrix, which increases the computational time and burden. As suggested by Abdelaziz et al. [59], although branch-based techniques are superior for distribution system analysis, they are based on having a slack bus in the system for convergence.

Overall, the literature lacks comprehensive studies for load flow analysis of islanded hybrid microgrids. A limited number of recent research articles has studied the power flow for this islanded paradigm by considering the operational philosophy of ICs [55]. Most of the work studying the hybrid microgrids has used time-domain analysis tools (e.g., MATLAB/Simulink and PSCAD/EMTP). This approach is feasible for very small systems, as developing the required models for this simulation environment is laborious and time-consuming and requires full details of the hardware parameters.

Another approach is the formulation of the load flow problem as an optimization problem to minimize the power mismatch equation subjected to the system's constraints, as in [61]. The solution for this optimization problem is, however, slow and computationally demanding. The authors in [62] and [63] considered load flows of multi-terminal dc systems (MTDC) as a form of a hybrid system, yet this mode is applicable only to a grid-connected mode of operation and with a slack bus and thus is not suitable for islanded hybrid microgrids. A steady-state load flow technique that takes into consideration limited capacity and droop-controlled DGs was presented in [64], with the generalized alternatives presented in [65] and [55]. However, these approaches are based on NTR and NR and thus still suffer from convergence issues when the R/X ratio is high. Furthermore, the computational time of these approaches increases significantly with the number of buses.

2.6 Discussion

The literature review presented in this chapter has shown the common probabilistic models used for renewable-based generation and loads. Although these models are widely used for power system

studies, they have discrete probability distribution functions when the output power is considered. The development of accurate probabilistic models for load and generation represents the very first step in conducting power system studies. In addition, this chapter illustrated different operational modes of microgrids presented in the literature and introduced the microgrid-to-microgrid mode of operation. Although, microgrids represent a feasible transition from bulky conventional grids to interconnected smart grids, this transition is still vague and requires more investigation. While extensive work has been done with respect to ac microgrids, few studies have tackled hybrid microgrids despite the increasing interest in these paradigms. Hence, there is a significant lack in literature of the overall planning of microgrids as hybrid ac/dc systems [55]. Although sufficient research work regarding the steady-state analysis of ac and hybrid microgrids has been conducted, the techniques used are centralized and computationally demanding. Thus, a fast and decentralized analysis tool is needed for the application of smart microgrids to cope with the limited computational capacity of the distributed agents and solution time restrictions for these types of applications.

Chapter 3
Novel Probabilistic Load and Generation Models and Probabilistic Power Flow Analysis

3.1 Introduction

Renewable-based distributed generators are being used more and more extensively, owing to the benefits they offer to both utilities and investors. With the near-viral spread of these DGs in power systems, the need for an accurate model that describes the probabilistic nature of renewable generation and load power is becoming crucial. These models represent a vital tool for analyzing the power system and are of extreme importance for applications related to power system planning and operation. Clearly, it is extremely challenging to obtain an accurate estimation of power system voltages and flows while both generation and load are continually changing. However, a precise model that follows the probabilistic behavior of wind or solar is crucial for power system planning and operation. Benchmark probabilistic models for renewable generation have been developed [66], [67] and widely used while probabilistic load models need more improvements to capture a load's behavior.

In this chapter, historical daily load profiles [31] are clustered into a proper number of clusters. Each cluster centroid load curve is used as the cluster's representative. Afterwards, the error between different load curves belonging to a cluster and its centroid is calculated. The goodness-of-fit tests K-S [68] and A-D [69] are used to find the best-fit PDF to model this error. Hence, the load is modelled by a number of average daily profiles associated with a PDF for the error around these averages. On the other hand, the existing and widely used probabilistic models for renewable generation (wind and solar) [70]-[72] need more improvements to appropriately capture the wind speed and solar irradiance behavior. Weibull PDF has been extensively used to model wind speed, but a discrete PDF will be used here to model the output power due to WECS [71], and a bi-modal beta PDF to model the solar irradiance.

Additionally, this chapter presents novel models that give one continuous PDF for the output power from wind or solar as a per-unit of their rating. The historical data for wind speed and solar irradiance at the same site (for a certain number of years) is used to calculate the per-unit output power from wind

and solar DGs. The per-unit output power is gathered into the appropriate number of clusters (scenarios). Then, similar to the approach used for load modelling, the goodness-of-fit tests K-S and A-D are used to find the best-fit PDF to model the per-unit output power. Hence, for each scenario, a PDF is used to model per-unit output power from wind- or solar-based DGs. To that end, the proposed load and generation models are integrated with the conventional forward/backward power flow algorithm to create a PPF tool that can be used to find the PPF in the power system lines and calculate the probabilistic voltage profiles. The MCS concept was adopted to calculate the probabilistic load flow. However, it was adapted here to accommodate the developed load and generation models.

The rest of the chapter is organized as follows. In section 3.2, the detailed process for obtaining probabilistic models for load is presented, while in section 3.3, renewable generation models are illustrated. Finally, the probabilistic load flow analysis based on MCS is described in section 3.4.

3.2 Probabilistic Load Model

Accurate probabilistic load modelling is crucial for power system planning and steady-state studies, especially with the growing deployment of renewable energy resources and PHEV. The increased penetration of renewable resources, which have high intermittency, initiated the need for PPF analysis of power systems. The deterministic model of load is no longer sufficient for accurate power system planning studies. The proposed model captures the probabilistic nature of loads and is suitable for the power flow studies needed for power system planning and adequacy studies. This novel model can be integrated with the probabilistic generation models and power flow algorithm to establish a PPF tool which will be described later in this chapter.

The modelling stages are shown in Figure 3.1, where historical daily load profiles are gathered into the appropriate number of clusters. The centroid of a cluster is considered the representative load curve for that cluster, while errors between all load profiles belonging to this cluster and its centroid are calculated. Finally, a goodness-of-fit technique is used to select the best PDF that fits the calculated error, and the load is modelled with a number of average load profiles representing different scenarios (clusters) in addition to the error represented by the PDF. These modelling stages will be explained in detail in the following sections.

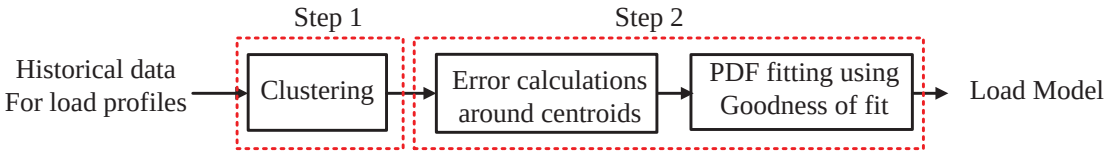

Figure 3.1: Load modelling stages.

3.2.1 Clustering of Load Profiles

Although the probabilistic load model in this section is developed based on the load data given in the IEEE RTS [31], the same methodology can be used for any historical data available. The annum is divided into four seasons, each of which has two different clusters: a weekday and weekend cluster. Accordingly, the historical daily load profiles are gathered into 8 different clusters (4 seasons × 2 clusters/season), as shown in Figure 3.2. However, the spring and fall seasons are identical, so these 8 clusters are reduced to only 6 distinguished clusters, as described in Figure 2.5.

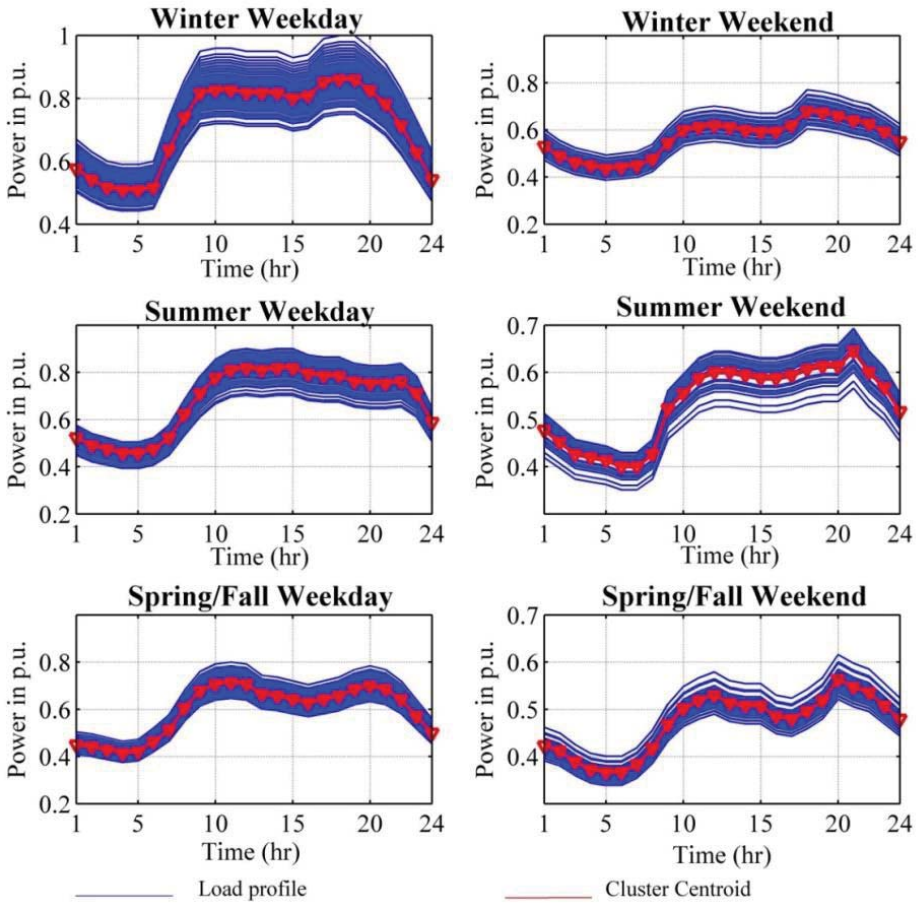

Figure 3.2: Different load clusters.

The load is accordingly modelled using 8 different models based on the aforementioned clusters, as presented in Table 3.1.

Table 3.1 Different Load Models

Season	Day Category	Model
Summer	Weekday	L1
	Weekend	L2
Winter	Weekday	L3
	Weekend	L4
Fall	Weekday	L5
	Weekend	L6
Spring	Weekday	L7
	Weekend	L8

As shown in Table 3.1, the load will have 8 models L1-L8 with two repeated models (i.e., L5/L7 and L6/L8 are the same). Each model corresponds to a cluster, which will be represented by the centroid or representative load curve. These load curves are established using the K-means clustering technique [73], which is based on minimizing the square of the error function presented in Equation (3.1).

$$\min\left(\sum_{j=1}^{k}\sum_{i=1}^{n} || x_i^j - c_j ||^2\right) \qquad (3.1)$$

where $|| x_i^j - c_j ||$ is the distance between data point x_i^j that belongs to a cluster, j , and the cluster's centroid, c_j. The resultant centroids are presented in Table 3.2, where, as we can see, the centroids are a daily load curve per unit.

3.2.2 Error Calculations and PDF Fitting

Using the cluster's centroids as load models is an approach that had been considered previously in the literature. It represents the deterministic load model that is not accounting for the probabilistic behavior of the load. Thus, the proposed methodology is an attempt to capture the probabilistic behavior of the load by calculating the difference between all the load curves that belong to the cluster and the cluster's centroid, and afterwards fit it to a PDF to represent this error. In order to find the PDF that appropriately fits the error calculated, the best-fit technique is used to select the PDF that matches the distribution of errors calculated. Accordingly, each cluster (scenario) will be represented by a load profile in conjunction with a probabilistic error that is represented by a PDF calculated from the historical data.

The best-fit PDF can be selected using the well-known goodness-of-fit tests [68], [69]. These tests are usually carried out by calculating a parameter called the test statistic, which is proportional to the error between theoretical (fitted) and experimental (historical) cumulative density functions (CDFs). Hence, the PDF with the lower static is the one that better fits the historical data. As the available number of samples for load data exceeds 2,000, both the K-S test, as expressed by Equation (3.2), and the A-D test, as expressed by Equation (3.3), can be used to identify the best-fit PDF.

Table 3.2 Representative Load Curves (Cluster Centroids)

Time	L1	L2	L3	L4	L5/L7	L6/L8
1	0.523	0.478	0.576	0.530	0.449	0.423
2	0.491	0.452	0.542	0.489	0.442	0.411
3	0.474	0.426	0.516	0.462	0.428	0.389
4	0.458	0.420	0.508	0.449	0.414	0.372
5	0.458	0.413	0.508	0.435	0.421	0.366
6	0.474	0.401	0.516	0.442	0.464	0.366
7	0.523	0.401	0.637	0.449	0.514	0.383
8	0.621	0.426	0.740	0.476	0.606	0.417
9	0.711	0.523	0.817	0.544	0.678	0.468
10	0.777	0.556	0.826	0.598	0.706	0.502
11	0.810	0.588	0.826	0.612	0.713	0.519
12	0.818	0.601	0.817	0.618	0.706	0.530
13	0.810	0.601	0.817	0.612	0.664	0.513
14	0.818	0.594	0.817	0.598	0.656	0.507
15	0.818	0.588	0.800	0.591	0.642	0.507
16	0.793	0.588	0.809	0.591	0.628	0.485
17	0.785	0.594	0.852	0.618	0.642	0.479
18	0.785	0.607	0.860	0.680	0.656	0.496
19	0.760	0.614	0.860	0.673	0.685	0.519
20	0.752	0.614	0.826	0.659	0.699	0.564
21	0.752	0.646	0.783	0.639	0.685	0.547
22	0.760	0.601	0.714	0.625	0.642	0.535
23	0.711	0.568	0.628	0.591	0.571	0.507
24	0.589	0.517	0.542	0.550	0.499	0.479

$$D = \max_{1 \le i \le n} \left(F(X_i) - \frac{i-1}{n}, \frac{i}{n} - F(X_i)\right) \tag{3.2}$$

$$A^2 = -n - \frac{1}{n}\sum_{i=1}^{n}(2i-1)\left[\ln F(X_i) + \ln\left(1 - F(X_{n-i+1})\right)\right] \tag{3.3}$$

These tests were applied to the IEEE-RTS data with the clusters described in the previous section.

The PDFs presented here are the ones with the least error (namely, Weibull, Beta, and Normal) distributions. This explains their extensive use and familiarity in the power system studies. The results for the statics of Anderson-Darling and Kolmogorov-Smirnov test are presented in Table 3.2.

Table 3.3 Goodness-of-Fit Test Results for Each Season

Season		**Distribution**					
		Normal		Beta		**Weibull**	
		K-S	A-D	A-D	A-D	K-S	**A-D**
Spring	weekday	0.06152	14.84	0.02592	1.6182	0.02119	**1.3777**
	weekend	0.12800	18.753	0.08348	6.4684	0.07062	**5.3665**
Fall	weekday	0.06152	14.840	0.02592	1.6182	0.02119	**1.3777**
	weekend	0.12800	18.753	0.08348	6.4684	0.07062	**5.3665**
Summer	weekday	0.06981	6.7969	0.04306	2.0816	0.03717	**1.2649**
	weekend	0.11731	9.5498	0.06259	1.9336	0.06258	**1.8939**
Winter	weekday	0.05075	4.5330	0.02839	1.2482	0.02728	**0.9970**
	weekend	0.09231	3.8603	0.07633	1.9491	0.0686	**1.8820**

Based on the obtained results presented in Table 3.3 and the goodness-of-fit tests described earlier, the Weibull PDF described by Equation (3.4) is the best PDF to model the error, as it has the least mismatch between fitted and historical data. Table 3.4 presents the parameters for the fitted Weibull PDF for each model L1-L8, as the Weibull PDF is the best fit for the historical data of load profiles.

$$f(x) = \frac{\alpha}{\beta}\left(\frac{x-\gamma}{\beta}\right)^{\alpha-1} e^{-\left(\frac{x-\gamma}{\beta}\right)^{\alpha}} \tag{3.4}$$

Table 3.4 Weibull PDF Parameters for Each Load Model

Model	**α**	**β**	**Γ**
L1	2.4226	0.09934	**-0.08812**
L2	1.7979	0.05353	**-0.04758**
L3	5.247	0.22676	**-0.20872**
L4	5.1698	0.16188	**-0.14876**
L5	8.2088	0.21547	**-0.20307**
L6	17.046	0.29313	**-0.28402**
L7	8.2088	0.21547	**-0.20307**
L8	17.046	0.29313	**-0.28402**

The calculated error between the IEEE-RTS data and load centroids presented in Table 3.2 is graphed as a histogram, with the fitted Weibull PDF curve calculated using the parameters shown in Table 3.3. Figure 3.3 compares both the histogram and fitted PDF for two load models. The graphs show the

closeness between the fitted PDF and the historical data.

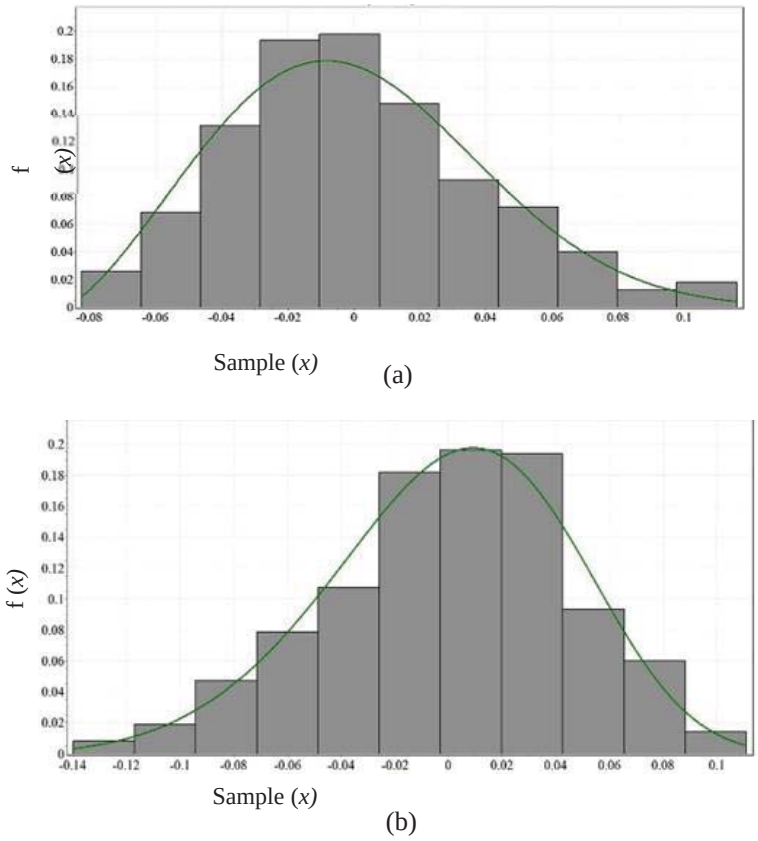

Figure 3.3: Historical data histogram and fitted PDF for (a) L1, (b) L3.

In summary, these results showed that the probabilistic model for load is a deterministic representative curve as presented in Table 3.2 in conjunction with a probabilistic error modelled with a Weibull PDF that has the parameters presented in Table 3.4. The models presented in Table 3.4 can be used as a benchmark probabilistic version of the IEEE-RTS deterministic load profiles data. However, the presented approach can be followed for any other load data. This approach can be summarized, as shown in Figure 3.1, in the following two steps:

- Step 1: Clustering of load profiles and finding the cluster centroids.
- Step 2: Calculating the error between cluster centroid and profiles belonging to the cluster and then fitting a PDF to the error.

The probabilistic load model will be formed from the deterministic load profiles (clusters centroid) in conjunction with a random error modelled using a best-fit PDF.

3.3 Renewable-generation Model

Benchmark models for renewable generation (i.e., wind and solar) have been used widely for many years. However, these models need enhancements to appropriately capture the behavior of wind speed and solar irradiance. The Weibull PDF has been broadly adopted and used to model wind speed, but no continuous PDF can be used to model the output power due to the WECS characteristics [71]. The approximate relation between wind speed and output power can be expressed in Equation (3.5).

$$P(v) = \begin{cases} 0 & 0 \le v \le v_{ci} \\ P_{rated} \times \dfrac{v - v_{ci}}{v_r - v_{ci}} & v_{ci} \le v \le v_r \\ P_{rated} & v_r \le v \le v_{co} \\ 0 & v_{co} \le v \end{cases} \tag{3.5}$$

The WECS characteristics shown in Figure 3.4 can be divided into three regions:

- Region 1: No output power
- Region 2: Constant output power
- Region 3: Linear output power-wind speed

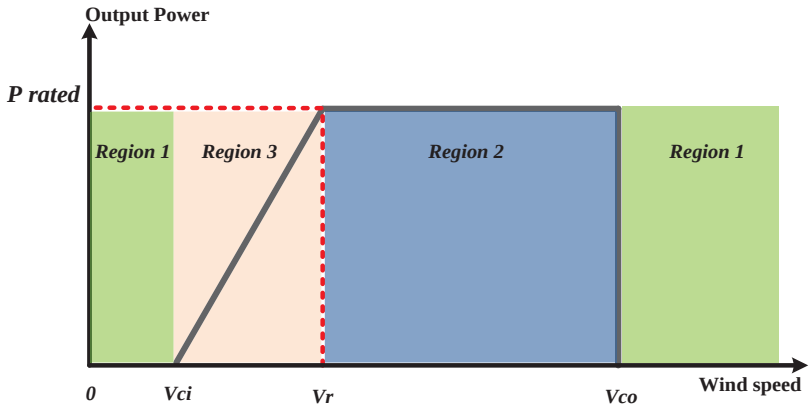

Figure 3.4 Wind energy approximate conversion curve.

Hence, with the wind speed represented with a Weibull PDF, the generated output power will be modelled with a Weibull PDF only in the linear region. Conversely, all of the speed probabilities in region 1 are combined into a single point with high probability and zero output power. Similarly, all the speed probabilities in region 2 are integrated into a single point with high probability and rated output power. Thus, to model the output power from wind, a mixed random variable that is neither continuous nor discrete should be used. This variable does not have a continuous PDF or CDF which is not recommended in power system studies. The Monte Carlo simulations usually involve the use of random numbers which are uniformly distributed over the interval [0, 1]. These uniformly distributed

random numbers are used for the generation of probabilistic variables from various continuous probability distributions. The probabilistic variables can then be used to study the behavior of other important power system variables. Atwa et al. [27] suggested dividing the wind speed into 10 states, converting these states into output power, and finding the probability of each state to model wind power probabilistically. Although this approach is suitable for the planning applications presented in their work, more samples [74] are required for probabilistic power flow to obtain accurate results that reflect the behaviour of the system. Similarly, for much of the day, there is very low solar irradiance, which results in high probability low irradiance. Thus, a bi-modal beta PDF is usually used to model the solar irradiance.

In this section, instead of modelling wind speed and solar irradiance as a random variable, the historical data for wind speed and solar irradiance at the same site (for a certain number of years) is used to calculate the historical per-unit output power from wind and solar DGs. The per-unit output power is clustered into an appropriate number of clusters (scenarios). The goodness-of-fit tests K-S [75] and A-D [76], as described earlier, are then used to find the best-fit PDF to model the per-unit output power. The goodness-of-fit tests will reveal the PDF that has minimum mismatch compared to the historical data. Hence, for each scenario, a continuous single PDF is used to model the per-unit output power from wind- or solar-based DGs, and thus MCS techniques can easily be implemented.

3.3.1 Probabilistic Wind Model

In order to accurately model the output power from wind-based generators, real historical data for three successive years of wind speed at a specific site are converted into output power using WECS characteristics. With P_{rated} considered as 1 per unit, the wind speed is now converted into per-unit output power with the power base equalling the rated power of the wind-based generator. These historical per-unit powers are clustered into four clusters (scenarios) representing the four seasons. For each cluster, the best-fit PDF of all the per-unit power data belonging to that cluster is used to model the output power from wind-based DGs. Goodness-of-fit tests are used for the determination of the best PDF; if the available wind data points exceed 2,000, the (K-S) and (A-D) tests are used, as expressed by Equations (3.2) and (3.3), respectively.

The results obtained from these tests are presented in Table 3.5. The PDFs presented here are the most common ones in the power system studies (Normal, Weibull, and Beta), in addition to the one showing minimum error (Johnson SB). As the goodness-of-fit tests calculate the error between real and hypothetical CDFs, the less the error value, the better the fit to the real data [68]. It can be seen from

the data in Table 3.5 that the best PDF for the wind output power data during all seasons is the Johnson SB distribution, expressed by Equations (3.6) and (3.7). The next best-fit PDF is the well-known Weibull PDF.

$$f(x) = \frac{\delta}{\lambda\sqrt{2\pi}z(1-z)} exp\left(-\frac{1}{2}\left(\gamma + \delta \ln\left(\frac{z}{1-z}\right)\right)^2\right) \tag{3.6}$$

$$z \equiv \frac{x-\xi}{\lambda} \tag{3.7}$$

Table 3.5 Goodness-of-Fit Test Results for Wind at Each Season

	Distribution							
	Normal		Johnson SB		Beta		**Weibull**	
	K-S	A-D	K-S	A-D	K-S	A-D	K-S	**A-D**
Spring	0.12714	71.088	0.03198	4.5135	0.1623	115.69	0.07846	**247.56**
Fall	0.08715	49.691	0.03395	7.1416	0.15671	114.28	0.09065	**190.33**
Summer	0.10693	55.584	0.02604	2.7687	0.15562	93.358	0.06007	**169.09**
Winter	0.08894	46.181	0.03228	18.196	0.08885	49.029	0.10157	**111.98**

A Johnson distribution is a 4-parameter distribution that is related to a normal distribution through a transformation (bounded transformation for Johnson SB) [77]. Because it has four parameters (δ, λ, γ, ζ), this distribution is very flexible for fitting empirical data. Figure 3.5 shows Johnson SB PDFs for differently shaped parameters. As can be seen from the figure, a Johnson SB has a high degree of flexibility for fitting a variety of empirical data shapes.

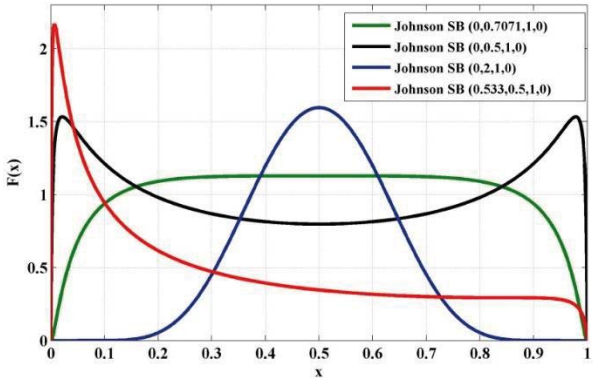

Figure 3.5: Johnson SB PDFs for a variety of parameters.

Thus, the probabilistic model for the per-unit output power from wind-based DGs is a Johnson SB PDF for each season, and hence there are four models (W1-W4), with the parameters provided in Table 3.6.

Table 3.6 Wind Models

Model	W1	W2	W3	W4
Season	Spring	Fall	Summer	Winter
γ	0.40832	0.1866	0.48423	-0.0199
δ	0.46673	0.49059	0.55561	0.48906
λ	0.97881	0.98015	0.97956	0.95746
ζ	-0.0765	-0.00616	-0.00874	0.005568

Figure 3.6 compares both the histogram and fitted PDF for two wind models. The graphs show the closeness between the fitted PDF and the historical data. Thus, a continuous single PDF is used to model the output power from wind and was successful in capturing the exact behaviour.

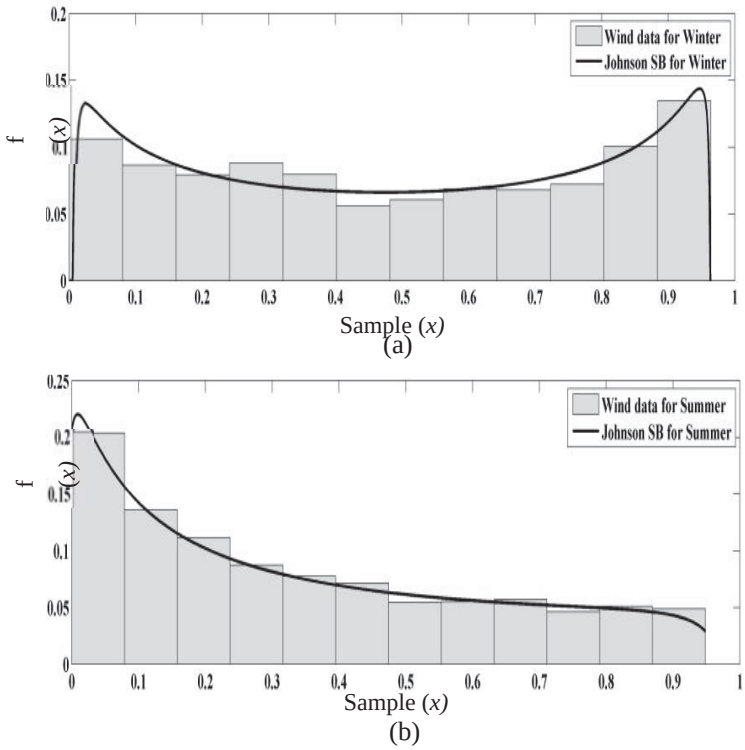

Figure 3.6: Historical data for wind per-unit power and fitted PDF for (a) winter and (b) summer.

The same modelling approach used for wind data is adopted for the historical data of solar irradiance at the same site. The data for three successive years was used as an input to Equation (3.6) [70] to calculate the solar output power per unit.

$$
\begin{aligned}
T_c &= T_A + s_a\left(\frac{N_{OT} - 20}{0.8}\right) \\
I &= s_a[\, I_{sc} + K_i(\, T_c - 25)] \\
V &= V_{oc} - K_v \times T_c \\
P(s_a) &= N \times FF \times V \times I \times \frac{1}{P_{rated}} \\
FF &= \frac{V_{MPP} \times I_{MPP}}{V_{oc} \times I_{sc}}
\end{aligned}
\qquad (3.8)
$$

The historical data for the per-unit solar output power are investigated to select the best-fit PDF that models the solar per unit output power. Similar to wind modelling, the year is divided into four seasons, and for each season, only the non-zero power periods are considered. As shown in Figure 3.7, periods from 5h to 20h are the only ones considered because the solar output power is zero outside this time window.

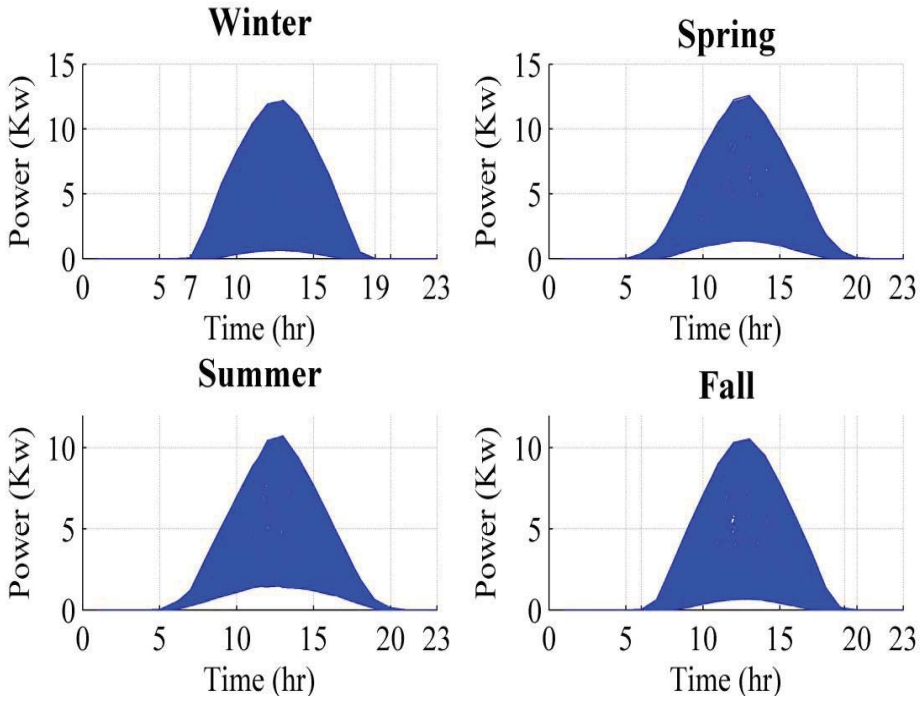

Figure 3.7: Solar power profiles during different seasons.

Same as for the wind model, K-S and A-D goodness-of-fit tests are used to select the best PDF fits the historical nonzero solar power data. The test results are presented in Table 3.7.

Table 3.7 Goodness-of-Fit Test Results for Solar at Each Season

	Johnson SB		**Beta**	
	K-S	A-D	K-S	**A-D**
Spring	0.06268	35.18	0.02561	**24.542**
Fall	0.06035	26.643	0.02418	**23.535**
Summer	0.06218	19.953	0.03934	**17.414**
Winter	0.06917	46.287	0.04097	**46.216**

The results show that the Johnson SB approach, as described by Equations (3.6) and (3.7), is the best-fit PDF. The parameters of Johnson SB PDF that model each season S1-S4 are shown in Table 3.8 and graphed in Figure 3.8. Hence, solar is modelled using five models (S1-S5) with S5 equal to zero (for periods outside the 5h to 20hr window).

Table 3.8 Solar Models

Model	S1	S2	S3	S4	S5
Season	Spring (5h-20h)	Fall (5h-20h)	Summer (5h-20h)	Winter (5h-20h)	Otherwise
γ	0.0925	0.1635	-0.18985	0.44519539	
δ	0.47215	0.44444	0.61823	0.47877	No output power (P=0)
λ	0.7118	0.64843	0.63197	0.731273	
ζ	0.92239	0.39591	0.79265	0.28251	

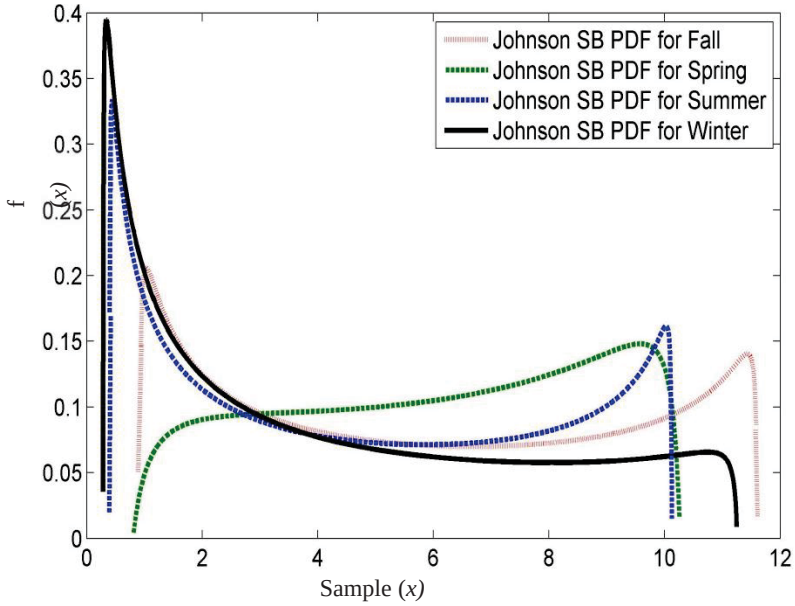

Figure 3.8: Johnson SB PDF for solar output power during each season.

3.4 Probabilistic Load Flow

The literature refers to a number of methods for determining the PPF, such as MCS and the two-point estimate method (2PEM) [74], [78]. MCS is an accurate and simple technique, but it requires a large number of samples (tens of thousands) in order to obtain accurate results [78]. In this work, MCS with 10,000 samples was selected for developing the PPF. It is important to mention here that computational time is not critical in planning studies such as the one we are considering in this thesis. However, if need be, this time can be reduced by setting a stopping criteria for the MCS instead of using a fixed number of iterations (i.e., terminate if the variance-to-mean ratio is less than a small value ε).

The MCS is integrated with the well-known forward backward sweep (FBS) power flow to create a PPF tool. MCS is selected for its simplicity and FBS is also selected as it is derivative-free and matrix inversion-free. A sample will be taken randomly from the load and generation PDFs. Hence, the solar, wind and load power value is known, and a power flow problem can be solved using FBS. The results are then analyzed in order to determine the PPF in the lines. The process of MCS consists of four steps, as detailed in Figure 3.9. Step 1, which is the modelling of input variables, is carried out in the previous sections, as the input variables are the renewable generation and load powers. The obtained models have these random variables represented with continuous PDFs as required for applying MCS. In this section, the sampling for random variables (step 2) is presented in section 3.4.1, while the FBS power flow technique that represents the numerical experimentation (step 3) is described in section 3.4.2. The output of step 3 is samples of the output variable which is the power flow in our study. Finally, step 4 is applying statistical analysis on the output to obtain the output's probabilistic characteristics. Thus, the PPF in the lines will be calculated by selecting the best-fit PDF for the lines power flow data using the same tests described earlier in this chapter.

3.4.1 MCS Samples for the Input Random Variables

Generating samples from random variables represents step 2 of the MCS process shown in Figure 3.9. The general sampling process from a random variable defined with a PDF $f(x)$ can be summarized by the following steps:

- $f(x) \rightarrow F(x)$: Convert the PDF into CDF
- $F(x) \rightarrow F^{-1}(x)$: Find the inverse CDF
- $u \leftarrow \mathrm{U} \in [0,1]$: Sample u from the uniform distribution on [0, 1]
- $x = F^{-1}(u)$: Find the required sample x using the inverse CDF

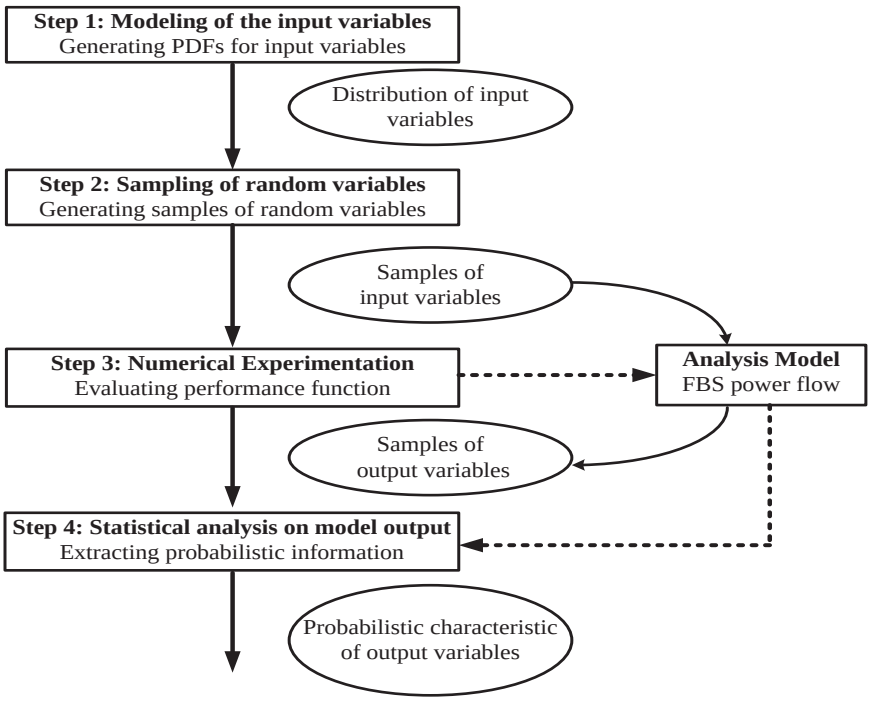

Figure 3.9: Monte Carlo Simulation process.

Although this method is simple and straight-forward, computing the CDF and the inverse CDF for the Johnson SB distribution expressed earlier is challenging. Thus, another approach can be used to simplify the MCS sampling process. This approach is based on transforming the desired distribution to a simple and well-known one using a defined transformation. Then, the sampling process for the simple distribution is carried out using the inverse of the transformation returned to the original distribution. This process is described in detail in the following subsections.

3.4.1.1 MCS samples for Weibull distribution

As explained earlier, the load is modelled with a Weibull PDF with parameters (α, β, γ), as expressed in Equation (3.4). To generate random samples from a Weibull distribution, first the CDF for the Weibull distribution can be expressed as follows:

$$F(x) = 1 - e^{[-\left(\frac{x-\gamma}{\beta}\right)^{\alpha}]} \tag{3.9}$$

Then the pseudo code presented in Figure 3.10 will be used to generate M random samples x from a Weibull distribution following the general steps explained previously.

For i = 1: M
Generate Uniform (0,1) → R
Calculate $\boldsymbol{x} = \gamma + \beta\ (-\ln(1 - R))^{\frac{1}{\alpha}}$
End

Figure 3.10: Algorithm used for generating random samples from Weibull PDF.

3.4.1.2 MCS samples for the Johnson SB distribution

It is essential to use a simple method to carry out the MCS for the Johnson SB distribution because following the general steps will be complicated. This simple method is performed by transforming the Johnson SB PDF to a normal distribution through a bounded transformation, as follows:

$$z = \gamma + \delta\, T(x) \tag{3.10}$$

where transformation T(x) for the Johnson SB distribution is defined as

$$T(x) = \ln\left(\frac{x - \zeta}{\lambda + \zeta - x}\right) \tag{3.11}$$

Based on (3.10) and (3.11), the algorithm required for performing the MCS for the Johnson SB PDF with parameters (δ, λ, γ, ζ) is as shown in Figure 3.11 [77]. This algorithm generates M random samples, x, from the Johnson SB PDF through the transformation of a normal random variable, R, to a Johnson SB random variable x.

For i = 1: M
Generate Normal (0,1) → R
Calculate $E = e^{\frac{R-\gamma}{\delta}}$
Calculate $x = \zeta + \lambda\ (\frac{E}{1+E})$
End

Figure 3.11: Algorithm used for generating random samples from Johnson SB PDF.

3.4.2 Forward Backward Sweep Power Flow

The numerical experimentation in this study is solving the load flow, which represents step 3 in the MCS process shown in Figure 3.9. Considering an existing system which is grid-connected, the well-known forward/backward sweep (FBS) power flow technique is used for solving the power flow problem in distribution systems because FBS can very effectively handle systems which are characterized by high R/X ratio (such as distribution systems). This intrinsic characteristic of distribution systems hinders the convergence of derivative-based load flow analysis such as Newton-Raphson and NTR. Moreover, as MCS was adapted for the PPF analysis, numerous runs of the power flow algorithm are expected. This fact makes the execution time a crucial factor in selecting the load flow technique.

Conversely, the forward-backward sweep technique is based on the iterative solution of the basic KCL and KVL network laws [79], with no power flow equations derivative or inverse of the Jacobian matrix. Thus, the computational burden and the execution time per solution are less compared to other techniques. Consequently, FB load flow techniques are candidates for the study presented in this work. The FBS can be done through sweeps of current, impedance or power. As shown in Figure 3.12, the power sweeps are adopted for this work, as active and reactive powers can be decoupled and run as real numbers instead of complex ones. FBS solution starts from load points and sweeps forward towards the PCC, at which point the grid acts as a slack bus with a known voltage. During this forward sweep, lines active and reactive power flow and losses are calculated. Afterwards, the solution switches to the forward direction starting from the PCC, calculating voltage magnitude and angle at all system buses. The forward and backward sweeps are repeated until convergence.

The flow chart for carrying out the forward/backward sweep algorithm is shown in Figure 3.14. The detailed equations used in forward and backward sweeps are described in the following subsections.

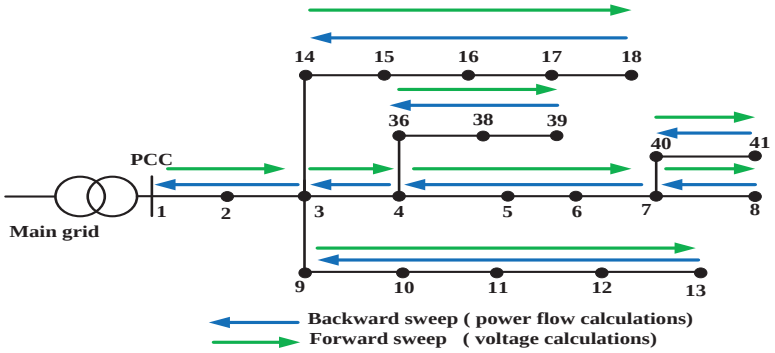

Figure 3.12: Illustrative diagram for carrying out FBS power flow.

3.4.2.1 Backward sweep

Starting from the last load points and sweeping towards the PCC, Equations (3.12 – 3.17) are used to calculate the power flows in the lines considering the line active and reactive losses. Then, considering the generic two-bus system shown in Figure 3.13, the calculations in the backward sweep start at j and go towards i. $P_{j,k}$ and $Q_{j,k}$ are known, while $P_{i,k}$ and $Q_{i,k}$ are unknown.

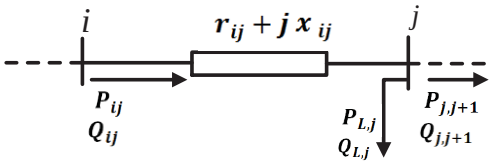

Figure 3.13: Generic 2-bus system.

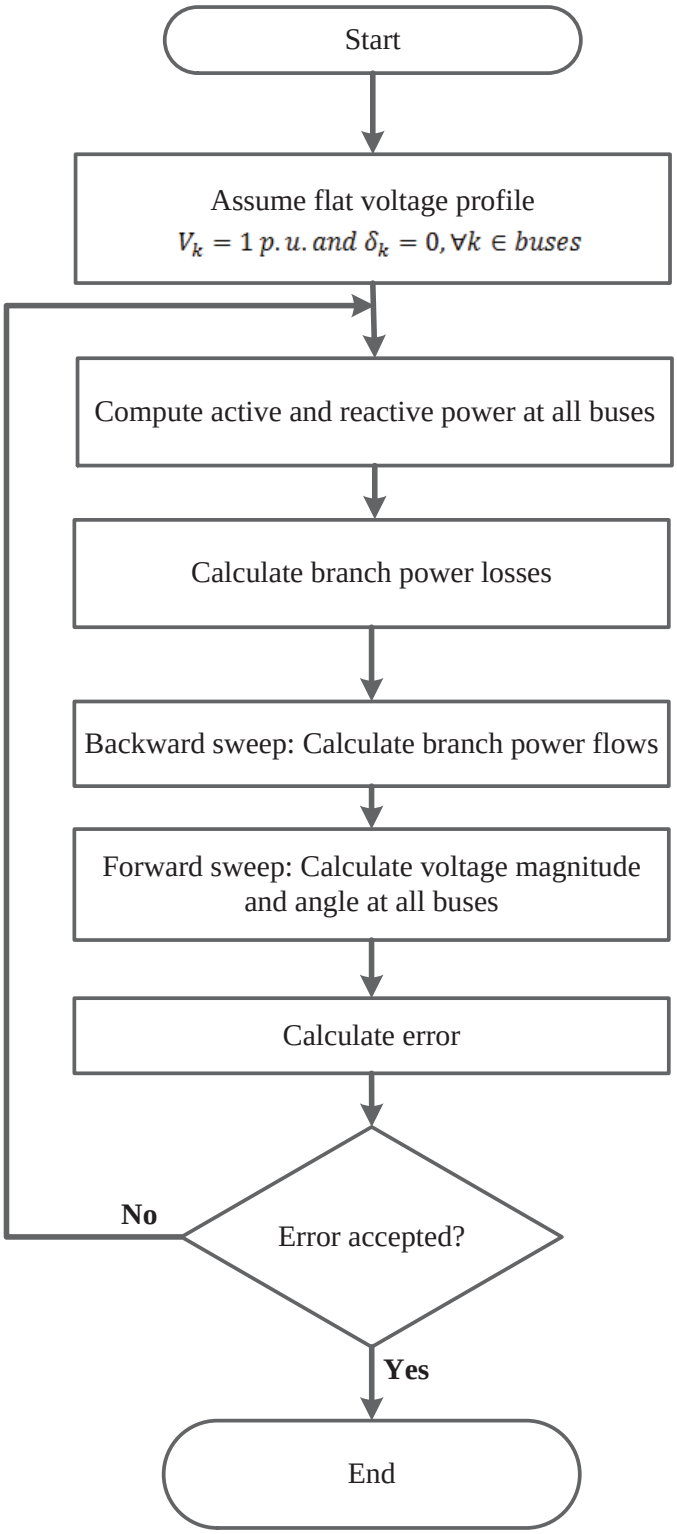

Figure 3.14: Flowchart for FBS power flow.

$$P_{i,j,k} = P_{j,k} + P_{Loss(i,j,k)} \quad (3.12)$$

$$Q_{i,j,k} = Q_{j,k} + Q_{Loss(i,j,k)} \quad (3.13)$$

$$P_{j,k} = P_{j,j+1,k} + P_{L,j,k} \quad (3.14)$$

$$Q_{j,k} = Q_{j,j+1,k} + Q_{L,j,k} \quad (3.15)$$

$$P_{Loss(i,j,k)} = r_{ij} \frac{(P_{j,k})^2 + (Q_{j,k})^2}{|V_{j,k}|^2} \quad (3.16)$$

$$Q_{Loss(i,j,k)} = x_{ij} \frac{(P_{j,k})^2 + (Q_{j,k})^2}{|V_{j,k}|^2} \quad (3.17)$$

3.4.2.2 Forward sweep

Starting from the PCC where the voltage magnitude and angle are known, we can use (3.18 - 3.21) to calculate the voltage magnitude and angles at all other system buses. For the generic two-bus system shown in Figure 3.11, the calculations in the forward sweep start at i and go towards j with $P_{i,k}$, $|V_{i,k}|$, $\delta_{i,k}$. $Q_{i,k}$ are known, while $V_{j,k}$ and $\delta_{j,k}$ are unknown.

$$|V_{j,k}| = \sqrt{|V_{i,k}|^2 - 2(r_{ij}P_{i,j,k} + x_{ij}Q_{i,j,k}) + |I_{i,j,k}|^2 |Z_{i,j}|^2} \quad (3.18)$$

$$|I_{i,j,k}|^2 = \frac{(P_{i,j,k})^2 + (Q_{i,j,k})^2}{|V_{i,k}|^2} \quad (3.19)$$

$$|Z_{i,j}|^2 = (r^2{}_{ij} + (x_{ij})^2) \quad (3.20)$$

$$\delta_{j,k} = \delta_{i,k} + \tan^{-1} \frac{r_{ij}Q_{i,j,k} - x_{ij} P_{i,j,k}}{|V_{i,k}|^2 - (r_{ij}P_{i.j.k} + x_{ij} Q_{i,j,k})} \quad (3.21)$$

The presented FBS power flow represents the analysis model for step 3 in Figure 3.9. The inputs for this model are sampled load and generation power and the output are the probabilistic line load flows. The final stage is to find the PPF in the lines. Similar to the methodology explained for modelling of wind and solar data, the goodness-of-fit tests are used to determine the best-fit PDF for the resultant line flows.

3.5 Discussion

This chapter has presented a probabilistic load flow algorithm to calculate probabilistic loading in network lines considering the probabilistic nature of load and generation. The tool is intended for studying existing grid-connected distribution systems with allocated DGs. The chapter developed the analysis tool required for the operational planning framework presented in Chapter 4. The initial and mandatory step in this type of probabilistic load flow analysis is developing an accurate model for load and renewable-based generation. To have accurate results, the developed model should appropriately reflect the probabilistic behavior of the modelled variable. A novel probabilistic model for wind-based DGs is presented which provides a continuous PDF that represents per-unit output power. The PDF is determined using goodness-of-fit tests that examine the inconsistency between the fitted PDF and the actual data, and selects the one with minimum deviation. Although, the same modelling approach is adopted for solar-based DGs and load, the developed scenarios for each variable were different and were selected based on the variables' characteristics. This approach revealed new PDFs which are not common in the power system research area; nevertheless, they are the best fit to the probabilistic behavior of wind and solar powers.

Thus, the following step was presenting a sampling methodology to perform MCS analysis for the obtained PDFs. To this end, two approaches were adopted based on the complexity of generating a random variable from a given distribution. The following step was using the well-known FBS power flow analysis technique as a means of carrying the steady-state analysis of the system. The results from applying the FBS and using the probabilistic model of load and renewable-based generation give the probabilistic load flow in the system lines. The final step is to fit a PDF to the obtained line flow using the goodness-of-fit tests. The integration of all steps presented in the chapter forms a PPF analysis tool that can be used for a wide range of power system studies and applications. The tool is mainly developed in this work to facilitate the operational planning study presented in detail in Chapter 4, and to realize the adaptive-self adequate operational planning philosophy.

Chapter 4
Adaptive Self-adequate Microgrids Using Dynamic Boundaries

4.1 Introduction

As mentioned in the introductory chapter, intensive research is being directed at microgrids because of their numerous benefits, such as their ability to enhance the reliability of a power system and reduce the environmental impact from these systems. Past research has focused on microgrids that have predefined boundaries. However, a recently published methodology suggested the determination of fictitious boundaries that divide existing bulky grids into smaller microgrids [80], thereby facilitating the use of a smart grid paradigm in large-scale systems. These boundaries are fixed and do not change with the power system operating conditions. We showed in Chapter 3 that both load and renewable generation have probabilistic natures and are continuously changing with time. Thus, operating the microgrid with a fixed boundary will not guarantee generation-load balance across all operating scenarios.

In this chapter, we propose a new concept for microgrid boundaries that incorporates flexible fictitious boundaries; we call this concept "dynamic microgrids". The proposed method is based on the allocation and coordination of agents and switches in order to achieve boundary mobility. The probabilistic behavior of loads and renewable-based generators are considered in the construction of these boundaries. The proposed framework is an operational planning approach for an existing distribution system that has allocated DGs and loads. This framework carries out a PPF study for the system and, based on the results, selects the virtual boundaries of feasible self-adequate microgrids. The PPF tool developed in Chapter 3 is used in this chapter as a means of calculating line flows for assessing self-adequacy. Compared to fixed boundary microgrids, our results show the superior performance of the dynamic microgrid concept for addressing the self-adequacy of microgrids in the presence of probabilistically varying loads and generation.

The remainder of the chapter is organized as follows. Section 4.2 includes a comprehensive explanation of the dynamic microgrid concept and the design steps required for dividing existing bulky grids into self-adequate microgrids. Section 4.3 discusses a number of system operating scenarios and also introduces a PPF algorithm for calculating the PPF for each operating scenario based on models presented in Chapter 3. Section 4.5 describes the use of the PG&E 69-bus system for demonstrating the

effectiveness of the proposed dynamic microgrid boundary design. The advantages of dynamic boundaries over static boundaries with respect to maintaining the self-adequacy of the constructed microgrids at all times are explained in section 4.4, while the final section presents the conclusions.

4.2 Microgrid Overview and Dynamic Microgrid Concept

4.2.1 Microgrid Overview

Investors and electrical suppliers are becoming increasingly interested in distributed generators (DGs) because of their associated technical and economic benefits. The growing awareness of their positive environmental impact is also stimulating additional research focused on renewable-based DGs. However, the intermittent nature of renewable resources still entails technical challenges, especially those related to the current power system infrastructure, which imposes limitations on the DG penetration level permitted in a power system. However, microgrids may provide a suitable environment for the deployment of renewable resources at high penetration levels [81]. Microgrid paradigms also represent a natural step in the evolution to future smart grids because they offer an appropriate confined environment for the implementation of techniques based on the use of smart technology for the optimal monitoring and management of a power system.

According to the US Department of Energy (DOE), a microgrid can be defined as "a group of interconnected loads and distributed energy resources (DERs) within clearly defined electrical boundaries that acts as a single controllable entity with respect to the grid and that connects [to] and disconnects from such [a] grid to enable it to operate in both grid-connected and island mode." [82] Based on this definition, microgrids are characterized by the following properties:

- They have clearly defined electrical boundaries.
- They act as a single controllable entity.
- They can connect to/disconnect from the grid.
- They comprise loads and DGs.

To divide existing bulky grids into microgrids, electrical boundaries for sub-microgrids should hence be clearly defined: each microgrid inside the defined boundaries should be controlled as a single entity that keeps its generation and load balanced so that it can connect to or disconnect from the grid keeping the total load supplied. Consideration of both the load and the probabilistic behaviour of renewable DG must therefore be incorporated.

In previous research, methods of determining microgrid boundaries were typically based on supply adequacy [80], [83] and reliability [84], and the boundaries obtained were fixed. Because renewable-based DGs and loads are probabilistic in nature, a fixed-boundary concept is inadequate for efficient and reliable microgrid operation. To overcome this deficiency, the present research work proposes a paradigm based on dynamic microgrids that have flexible boundaries. The following subsection introduces the microgrid boundary as a new control variable for achieving self-adequacy.

4.2.2 Dynamic Microgrid Concept

A dynamic microgrid can be defined as "a microgrid with flexible boundaries that expand or shrink to keep the balance between generation and load at all times." It is clear from this definition that the trigger for changing the boundaries of such a microgrid is an imbalance between the local generation available from DGs on the one hand and the loads on the other. Greater DGs or loads will thus be added to the microgrid coverage area in order to maintain self-adequacy at all times (adaptive self-adequacy). For ultimate flexibility, as shown in Figure 4.1(a), each node must be controlled through an agent, which enables the size of the microgrid to be increased by the addition of the nearest node under the control of that microgrid's agent in order to maintain the local generation-load balance. However, assigning an agent for each node and then controlling all the agents independently complicates power system operation and increases costs. A controllable switch must also be installed at each node so that the clustered microgrids can island at specific times in case of emergencies, an arrangement that is economically unfeasible.

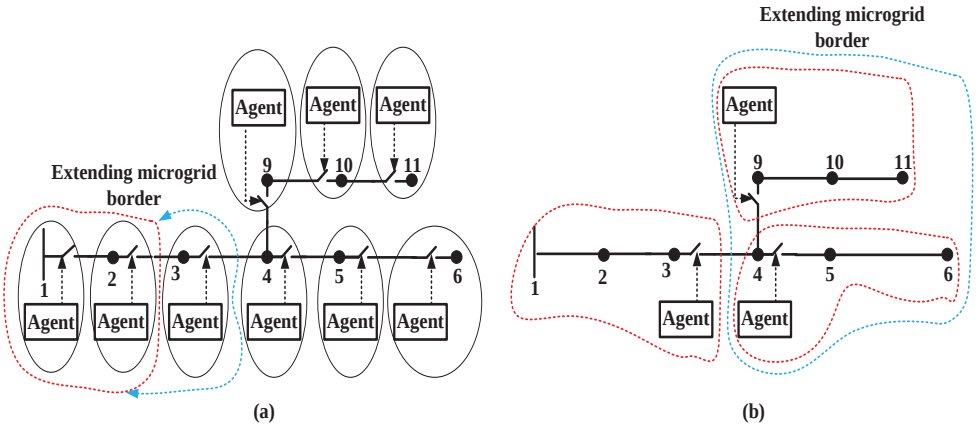

Figure 4.1: Different strategies for microgrids with variable boundaries: (a) ultimate flexibility (b) limited flexibility.

Conversely, as shown in Figure 4.1 (b), the suggested design of dynamic microgrid will set the minimum required agents and switches by setting clusters of nodes called the building clutters or

building microgrids, and thus the flexibility is limited. As shown in Figure 4.2, the proposed design framework can be divided into two stages:

- **Stage 1** is an operational planning stage: Given an existing system with allocated DGs and loads, all possible power system operating scenarios (section V) are defined based on the variability associated with the loads and generation output discussed in Chapter 3. Rather than controlling each node, as previously reported in the literature, clusters of nodes (building clusters) are then selected to be controlled. The selection of these clusters is based on an assessment of self-adequacy during each operating scenario. Each cluster of nodes is surrounded by isolation switches, and each cluster is assigned a controlling agent.

- **Stage 2** is an operational stage: Self-adequate microgrids are formed for each specific operating scenario. These microgrids are created from the building clusters identified in stage 1. Groups of clusters are merged to form the desired microgrids; which means that the building clusters set the available degree of freedom. In this stage, the operation of assigned agents in stage 1 is set to achieve self-adequacy at the operating scenario.

The steps involved in dividing existing bulky grids into adaptive self-adequate microgrids are presented in the flowchart shown in Figure 4.2. It is important to mention that the optimal mix, size, and allocation of DGs in the power system have already been examined in depth, as reported in the literature [5-10], and this chapter considers the operational planning of an existing distribution system with already allocated resources. A discussion of these issues of DGs sizing and sitting is therefore not repeated in this chapter, and an explanation of this step in the proposed design approach is thus omitted. Hence, DG sizes and locations are considered given as an input stage to the algorithm. Steps 1 to 6, as described in Figure 4.2, determine the building clusters and assign the required agents. These steps represent stage 1 of the proposed design framework. In steps 2 and 3, because of the probabilistic nature of both the loads and renewable-based DGs, the year is divided into appropriate representative operating scenarios (section V) based on the load and generation models obtained in Chapter 3. Moreover, for step 4, the PPF tool also developed in Chapter 3 is used for the calculation of PPF in power system lines for each scenario. In step 5, each scenario is also examined in order to identify lines that are weakly loaded, which represent a possible virtual boundary for self-adequate clusters of nodes during that scenario. The union of the self-adequate clusters identified for all scenarios determines the building clusters. An agent will be allocated for each cluster of the building clusters identified in step

5, in addition to an isolation switch at the boundary bus which represents step 6 of the proposed framework. The final step – step 7 – represents stage 2 of the framework and aims at setting the operational strategy for the allocated agents to realize the dynamic boundary concept to achieve self-adequacy at different operating scenarios.

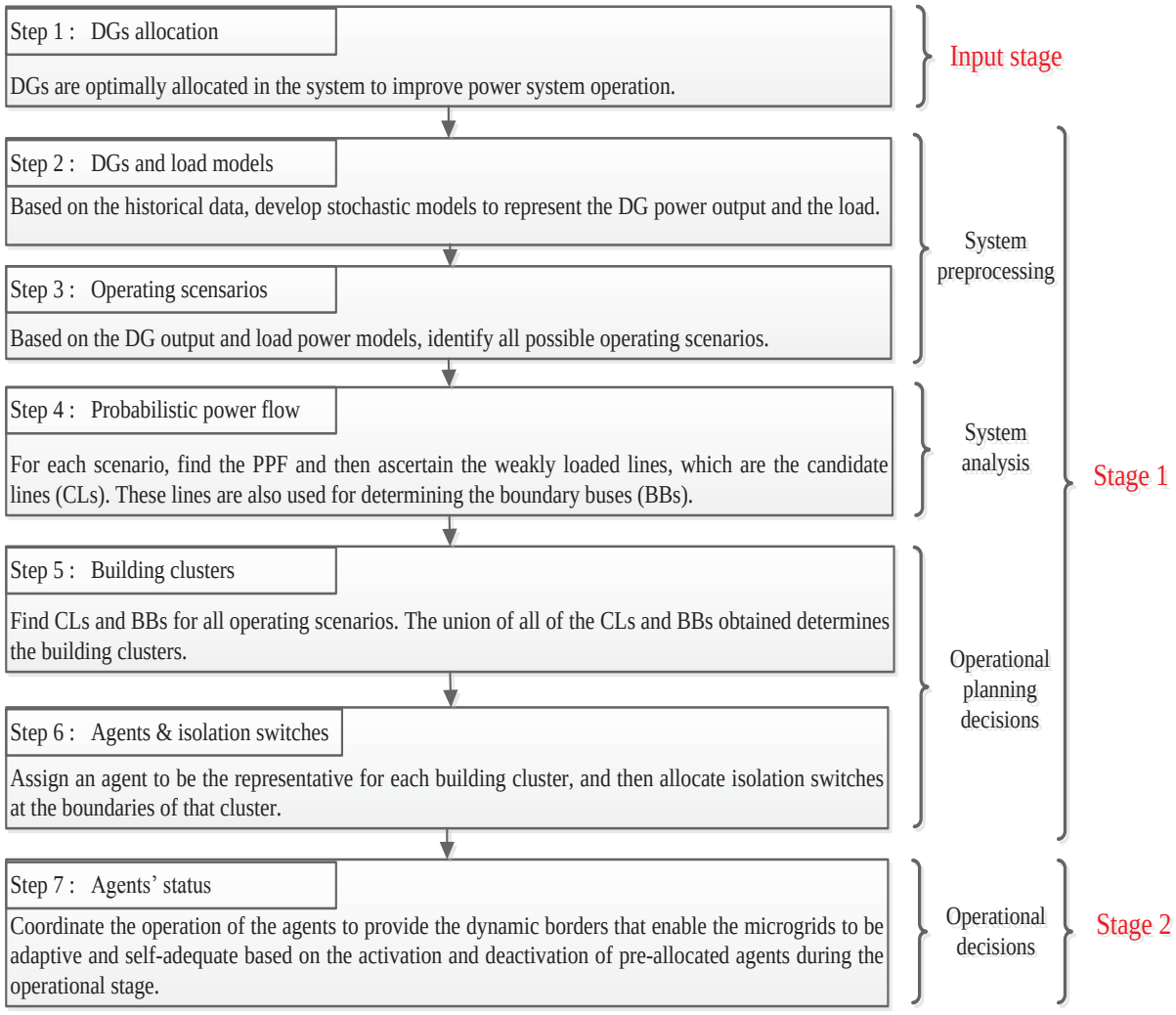

Figure 4.2: Steps to divide bulky grids into adaptive self-adequate microgrids.

4.2.2.1 Building clusters and cluster agents

Building clusters represent all possible self-adequate clusters of nodes that can be formed from all operating scenarios. Thus, a building cluster is part of the system that contains nodes with connected loads and DGs that have their power balanced; hence, the cluster is a self-adequate microgrid during certain operating scenarios. Each building cluster is assigned a communicable agent, as shown in

Figure 4.3. Therefore, the building cluster contains lines, connected loads and DGs, an isolation switch, a communication link, and an agent. This agent represents the cluster of nodes and performs the following functions:

- Supervisory control of all the DGs within the cluster boundaries.
- Two-way communication with the customers' smart meters within the cluster boundaries.
- Communication with neighbouring clusters' agents.
- Control of the clusters' isolation switches.

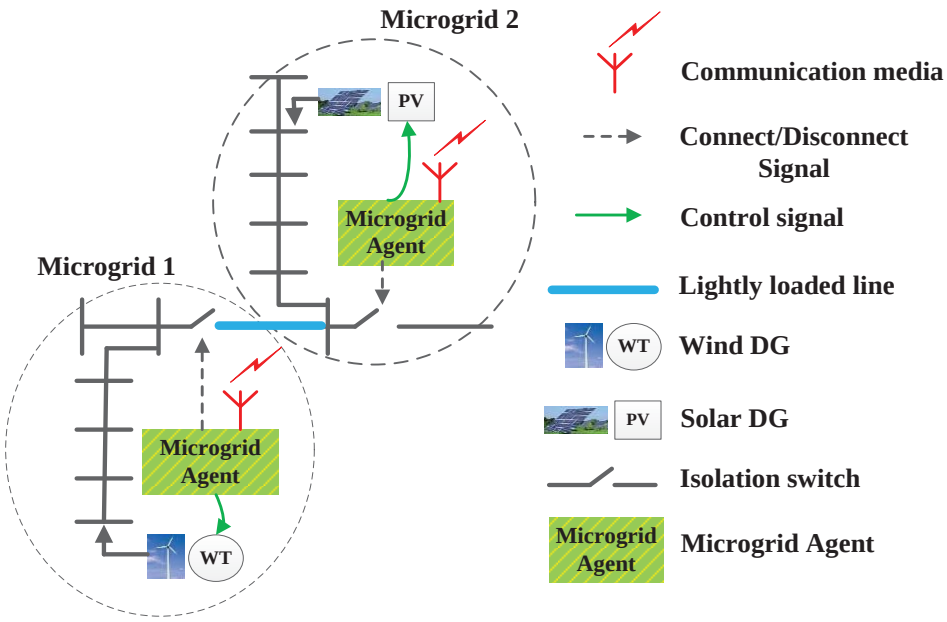

Figure 4.3: Functions of microgrid agent.

The agent can also be deactivated, which means that although it is still performing all other agent functions, it no longer has control over the isolation switch. Figure 4.4 shows an example of the modification of the boundaries through the activation/deactivation of the agents to merge/demerge microgrids. In Figure 4.4 (a), two microgrids are depicted with two independent agents and isolation switches. However, these two microgrids can be merged to form one larger microgrid if one of the agents is deactivated (Figure 4.4 [b]). The active agent is then representative of the entire microgrid and controls the isolation switch.

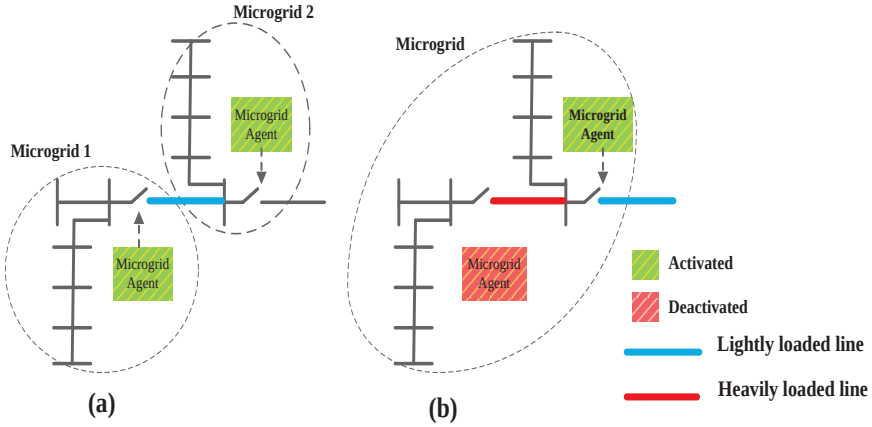

Figure 4.4: Dynamic microgrid borders produced for two operating scenarios.

However, even though an agent has been deactivated, it is still responsible for collecting data from and distributing commands to/from all components under its control umbrella so that data privacy is maintained and the number of managed nodes is limited. Each agent knows all of the information about the components under its control, e.g., customer loads, generation ratings, available generation, types of generation, and location of generation. When the agent is deactivated, it gives control to the active agent, which now knows only the aggregated generation and loads associated with the components that have been newly added under its umbrella, and thus privacy is maintained.

4.3 Operating Scenarios and Probabilistic Power Flow

Step 2 of the proposed framework was explained in Chapter 3, where probabilistic models for load and renewable-based generation were developed. Therefore, this section discusses steps 3 and 4 of the proposed methodology. In this part, we will identify the possible operating scenarios based on the probabilistic load and DG models discussed in Chapter 3, and will also calculate the PPF for each scenario. Based on the models developed to represent generation and loads, as explained in Chapter 3, the year is divided into four seasons to enable an examination of all possible operating scenarios. Each season is represented by two days: a weekday and a weekend day. Each day is then divided into two time periods: day and night. The entire year is thus represented by 16 different operating scenarios (4 seasons/years * 2 days/season * 2 scenarios/day), as shown in Table 4.1. The parameters for load, wind, and solar models are presented in Table 3.4, Table 3.6, and Table 3.8, respectively. For each scenario, an MCS is employed as a means of finding the PPF in the lines, as explained in Chapter 3. The lines with the minimum flows are selected as candidate lines (CLs), and their buses become the boundary buses (BBs) for self-adequate microgrids.

Table 4.1 Operating Scenarios for the Year, with Corresponding Wind, Solar, and Load Models

Scenario	Season	Day	Time	Solar	Wind	Load	Load-generation Model
1	Summer	Weekday	Day	S1	W1	L1	S1-W1-L1
2			Night	0		L1	0-W1-L1
3		Weekend	Day	S1		L2	S1-W1-L2
4			Night	0		L2	0-W1-L2
5	Winter	Weekday	Day	S2	W2	L3	S2-W2-L3
6			Night	0		L3	0-W2-L3
7		Weekend	Day	S2		L4	S2-W2-L4
8			Night	0		L4	0-W2-L4
9	Fall	Weekday	Day	S3	W3	L5	S3-W3-L5
10			Night	0		L5	0-W3-L5
11		Weekend	Day	S3		L6	S3-W3-L6
12			Night	0		L6	0-W3-L6
13	Spring	Weekday	Day	S4	W4	L7	S4-W4-L7
14			Night	0		L7	0-W4-L7
15		Weekend	Day	S4		L8	S4-W4-L8
16			Night	0		L8	0-W4-L8

These CLs represent the location at which the isolation switches should be installed and controlled. The union of all possible self-adequate microgrids can be performed during all scenarios and represents the building microgrids required to achieve the dynamic boundaries concept. The pseudo code to execute the proposed framework is presented in Figure 4.5.

1	Set MCS counter to zero
2	Set scenario counter to 1
3	Sample load, solar and wind according to the methodology and models explained in Chapter 3.
4	Assume flat start $V_k = 1\ p.u. and\ \delta_k = 0, \forall k \in buses$
5	Calculate $P\ and\ Q$ at all buses
6	Calculate branch power losses
7	Calculate branch power flow (backward sweep)
8	Calculate buses voltage and angle (forward sweep)
9	Calculate error; if not accepted, go to 5
10	Increase the MCS counter; if not reaching maximum, go to 3
11	Calculate PPF in the lines
12	Display all voltages, angles, active power and reactive power for this scenario
13	Select CLs and BBs
14	If the scenarios counter is less than 16, increase it and go to 3
15	Find the building microgrids (the union of all scenarios)
14	End

Figure 4.5 Pseudo code for the determination of building microgrids.

at the candidate buses indicated in Table 4.2 is used as a demonstration system. The supply mix contains wind, solar and biomass DGs. The system was modelled and biomass-based DGs are represented using constant output power [80], [84]. The PPF algorithm was applied using the proposed wind, solar, and load probabilistic models, and then calculated for the 16 different operating scenarios listed in Table 4.1. Samples are taken from the load and renewable generation models as described in the previous chapter. The power flow problem is then solved using a forward/backward sweep, following which the results are analyzed in order to determine the PPF in the lines. Weakly loaded lines that have minimum flows are then selected as CLs, and their buses become the BBs for the simulated scenario (steps 3 and 4, Figure 2.4). To ensure self-adequacy, the loading of selected CLs should not exceed a certain threshold, which is considered as 5% of the rated value of each line in this work (the rated values of the lines are found from the deterministic power flow in these lines considering data presented in [91]).

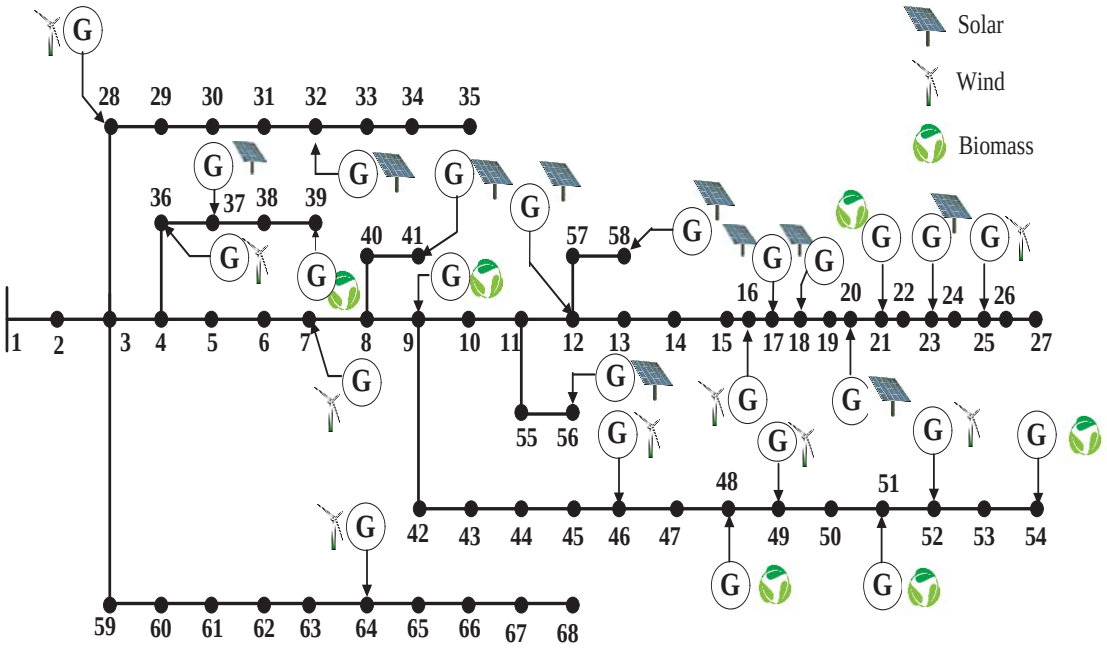

Figure 4.6: PG&E 69-bus system with DGs allocated at candidate buses.

Table 4.2 DG Ratings, Types and Locations

DG Type	Wind	Solar	Biomass
Buses	7,16,25,28,36,46,49,52,64	12,17,18,20,23,32,37,41,56,58	9,21,39,48,51,54
Ratings (KW)	50,25,75,75,100,25,50,50,50	25,25,50,75,25, 25,50,50,50,25	50,200,200, 125,175,200

For example, during scenarios 7 and 8 (Table 4.1), the proposed framework is executed. After the MCS counter reaches the maximum number, the PFF load flow in the lines is computed using the best-

fit PDF technique explained earlier. The convergence of the MCS for one of the links (link 16) is presented in Figure 4.7. The results show that, the solution converges and settles after almost 200 samples. However, 10,000 samples were used to ensure accurate results, especially since the planning problem is not time-critical. The fitted PDF for the PPF loading of this link during scenarios 7 and 8 is presented in Figure 4.7. From the deterministic power flow, the loading of link 16 is 29.69 KW, which is considered the rated value of this link, while the average PPF loading of this link is 1.478 KW, which is 4.98% from the rated value (29.69 KW). Thus, this link is considered a candidate link for a self-adequate microgrid during these scenarios and its associated buses are the BBs.

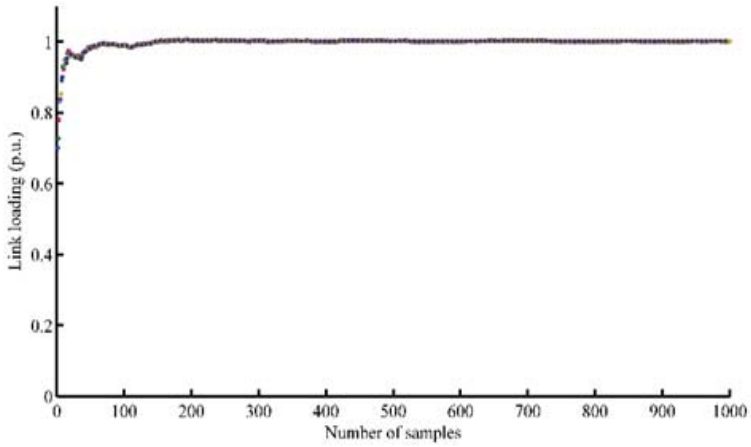

Figure 4.7: Convergence of PPF in link 16 with number of iterations during scenarios 7 and 8.

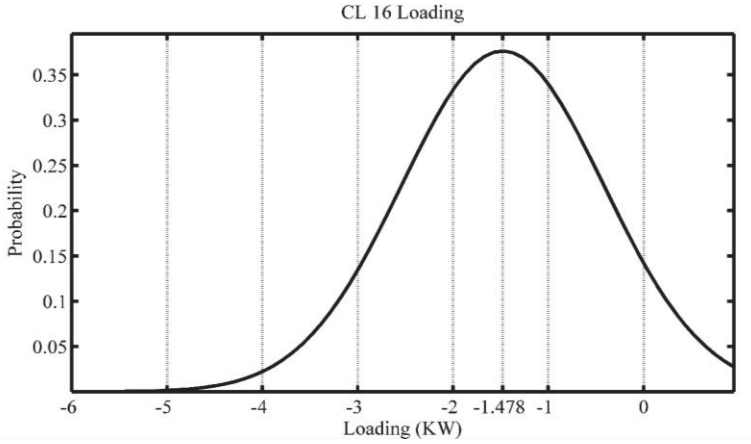

Figure 4.8: Fitted PDF for the PPF in link 16 during scenarios 7 and 8.

Similarly, the convergence of the MCS for link 58 is presented in Figure 4.9. The results show that the solution converges and settles after almost 300 samples. The fitted PDF for the PPF loading of link 58 during scenarios 7 and 8 is presented in Figure 4.10. From the deterministic power flow, the loading

of link 58 is 93 KW, which is considered the rated value of this link, while the average PPF loading of this link is 2.08 KW, which is 2.24% from the rated value (93 KW). Thus, this link is also considered a candidate link for a self-adequate microgrid during these scenarios, and its associated buses are the BBs. This framework is executed for all scenarios, and all the links were investigated to select the CLs and the BBs. The total computation time to run the entire algorithm for all scenarios is 54381.822 seconds or 15.106 hours on a CPU with the following specifications: Intel core i7 860 @2.8GHz, RAM 8GB, 64 bits.

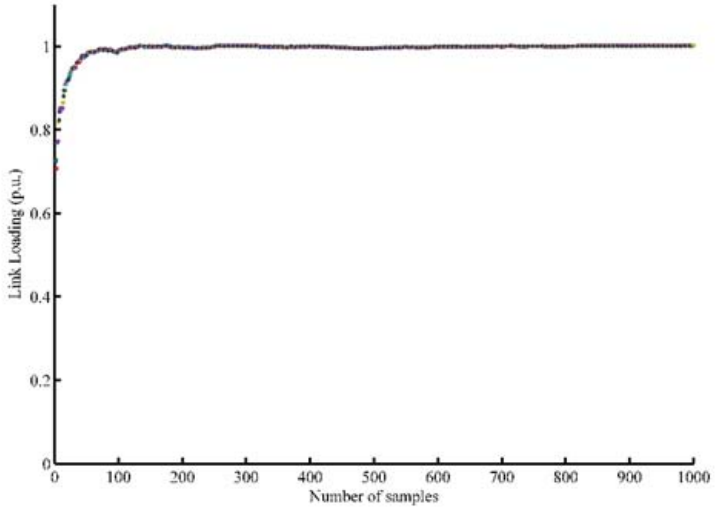

Figure 4.9: Convergence of PPF in link 58 with number of iterations during scenarios 7 and 8.

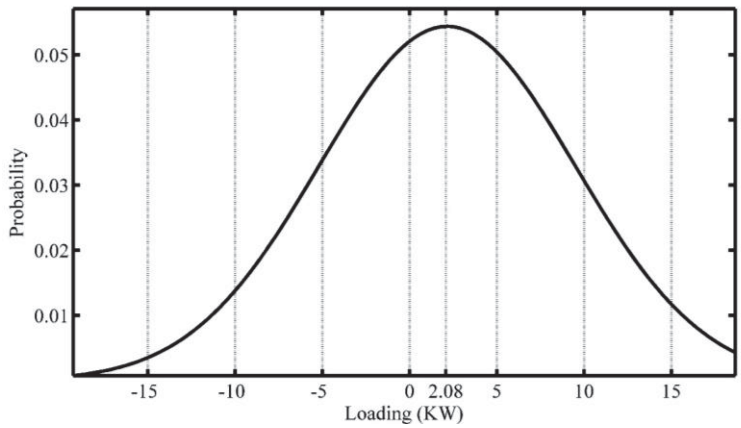

Figure 4.10: Fitted PDF for the PPF in link 58 during scenarios 7 and 8.

Table 4.3 shows the CLs and BBs obtained for all the operating scenarios. Based on the results of the 16 different operating scenarios, the minimum number of CLs required to realize all scenarios is found from taking the union of all obtained CLs. The union of these CLs and the BBs obtained for all

scenarios are shown in Table 4.4. These CLs and BBs then determine the building clusters (or microgrids) available, as shown in Figure 4.11. However, the borders are factious and will be utilized during emergencies. In case of an emergency, such as a fault in the lines, the system will be divided into the islands determined by the factious boundaries, even though during normal operations the system is interconnected. Hence, these factious boundaries are changed during normal operation (system is interconnected) based on the operating scenario and will be used during emergencies. Moreover, during normal operation, the agents of each cluster will optimally manage the components under its control umbrella.

Table 4.3 Boundary Lines for Different Operating Scenarios

Scenario	CLs	BBs
1	16,67	16-17,12-57
2	16,67	16-17,12-57
3	58,67	47-48,12-57
4	58,67	47-48,12-57
5	67	12-57
6	67	12-57
7	16,21,27,32,40,46,50,58, 65,67	16-17,21-22,3-28,31-32, 63-64,4-36,8-40,47-48, 11-55,12-57
8	16,21,27,32,40,46,50,58, 65,67	16-17,21-22,3-28,31-32,63-64,4-36,8-40,47-48, 11-55,12-57
9	15,67	15-16,12-57
10	15,67	15-16,12-57
11	11,21,27,32,40,46,50,52, 56,58,65,67	11-12,21-22,3-28,31-32,63-64,4-36,8-40,9-42, 45-46,47-48,11-55,12-57
12	11,21,27,32,40,46,50,52, 58,65,67	11-12,21-22,3-28,31-32,63-64,4-36,8-40,9-42, 47-48,11-55,12-57
13	15,67	15-16,12-57
14	15,67	15-16,12-57
15	11,15,21,27,32,40,46,50,52, 58,65,67	11-12,21-22,3-28,31-32,4-36, 63-64,8-40,9-42,45-46,47-48,11-55,12-57
16	11,15,21,27,32,40,46,50, 52,65,67	11-12,15-16,21-22,3-28,31-32, 63-64,4-36,8-40, 9-42,47-48,11-55,12-57

Table 4.4 CLs and BBs for All Scenarios

CLs	BBs
11, 15, 16, 21,27, 32, 40, 46, 50, 52, 56, 58,65, 67	11-12, 15-16, 16-17, 21-22,3-28, 31-32, 63-64, 4-36, 8-40, 9-42, 45-46, 47-48,11-55, 12-57

According to the CLs and the BBs obtained, as presented in Figure 4.11, there are 14 CLs that create 15 building clusters (step 5). These building clusters and their virtual borders are shown in Figure 4.12. The number of agents that must be allocated is 15 (A1 to A15), as described in Figure 4.1 (step 6). The

locations for the isolation switches are also determined based on the CLs selected. The activation and deactivation of the agents during the operation stage then forms the self-adequate microgrids; this feature preserves self-adequacy during a variety of operating conditions.

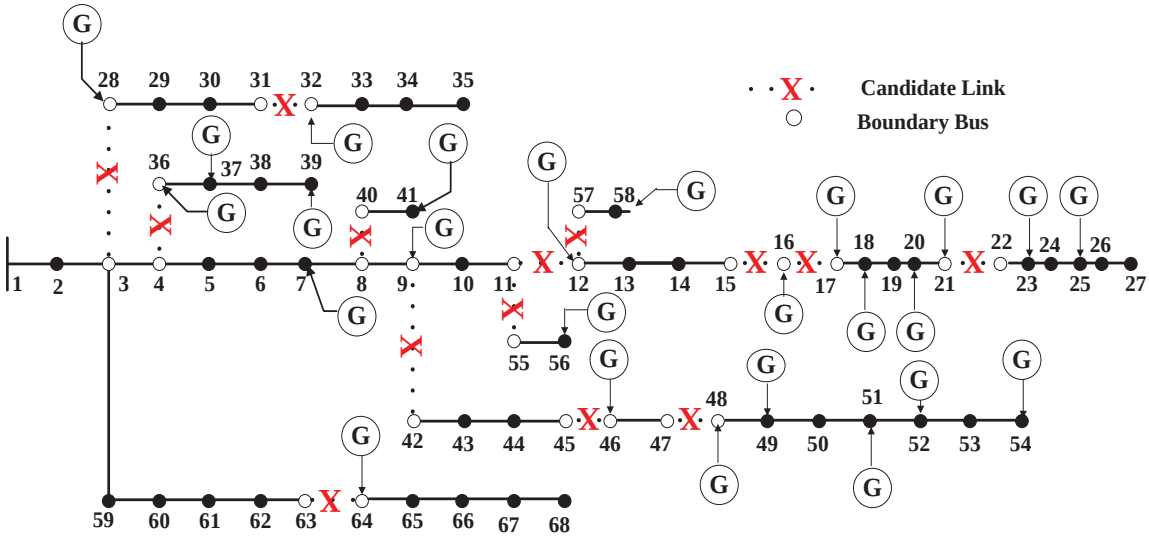

Figure 4.11: PG&E 69-bus system with CLs and BBs.

Adaptive self-adequate microgrids are produced by merging/demerging the building clusters. The size of the microgrids therefore cannot be changed by a node step because the step size is limited by the size of building clusters available (Figure 4.12). However, to provide the ultimate degree of freedom and a minimum step size, an agent and an isolation switch should be allocated for each node, as explained in Figure 4.1, which is unacceptable in practical applications.

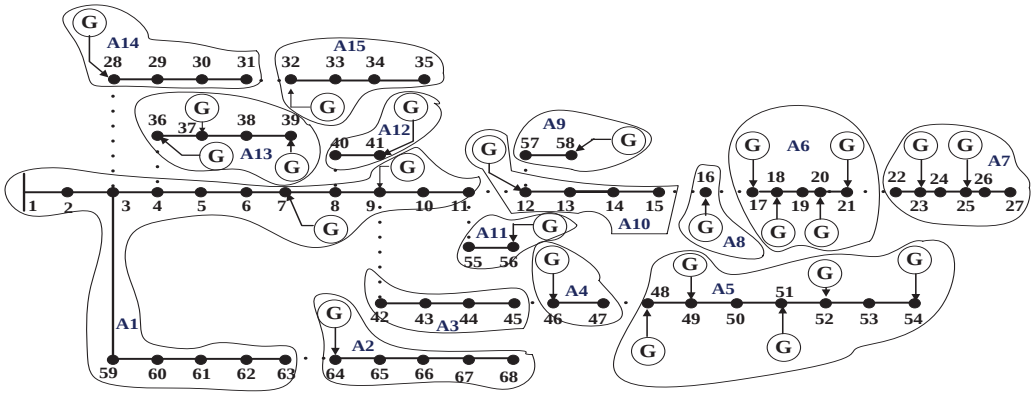

Figure 4.12: Allocated agents and building cluster boundaries.

I r of isolation switches and agents (compared to adding a switch and agent for each node) to represent the system with a limited degree of freedom that is determined based on the number of building clusters. The system under study has 16 operating scenarios (Table 4.1). For each scenario, the status of the

agents (A1 to A15) determines the borders of the feasible self-adequate microgrids. The status for each agent is set so that self-adequate microgrids are formed for that scenario. However, the agents allocated provide the operator with the ability to maneuver by overriding the status of an agent in order to change the borders and produce a specific layout. During the operating stage, the status of the allocated agents determines the fictitious boundaries of the microgrids, as illustrated by the example presented in section 4.2 for the assumed two scenarios (Figure 4.4). Table 4.5 shows the CLs and the BBs for each scenario; the agent status during each scenario has been selected to achieve the results listed in this table. For example, during scenarios 7 and 8, there are 9 CLs and hence there are 10 self-adequate microgrids that can be formed (10 active agents), as shown in Figure 4.13.

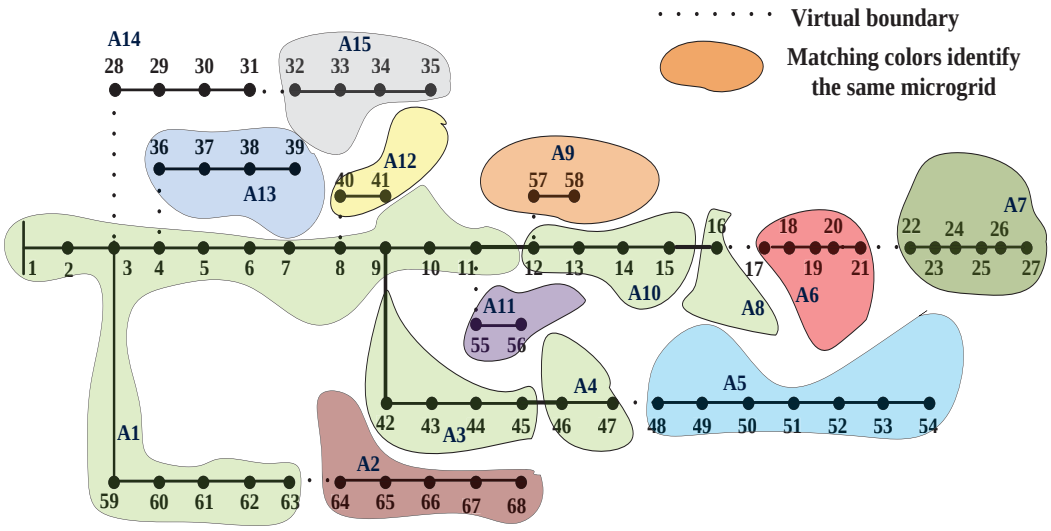

Figure 4.13: Microgrid boundaries during scenarios 7 and 8.

The building clusters represented by A1 to A4, A8, and A10 should be merged to form a self-adequate microgrid. Therefore, only one of these agents is activated, and all of the others are deactivated. The remaining building clusters are self-adequate during these two scenarios, and their agents are thus active. Table 4.5 indicates the status of the agents (step 7) during each operating scenario. The boundaries are consequently flexible and not fixed: dynamicity is achieved through the activation/deactivation of the allocated agents, and self-adequacy is preserved during all operating scenarios.

Table 4.5 Status of Agents for Different Operating Scenarios

Scenario	Agents to Be Merged	Active Agents
1	(A6→7), (A1→5, A8, A10→15)	A6, A10, A9
2	(A6→7), (A1→5, A8, A10→15)	A6, A10, A9

3	(A1→4, A6→8, A10→15)	A10, A5, A9
4	(A1→4, A6→8, A10→15)	A10, A5, A9
5	(A1→8, A10→15)	A10, A9
6	(A1→8, A10→15)	A10, A9
7	(A1, A3, A4, A8, A10)	A10, A2, A5→7, A9, A11→15
8	(A1, A3, A4, A8, A10)	A10, A2, A5→7, A9, A11→15
9	(A6→8), (A1→5, A10→15)	A6, A10, A9
10	(A6→8), (A1→5, A10→15)	A6, A10, A9
11	(A10, A6, A8)	A10, A1→5, A7, A9, A10→15
12	(A3→4), (A10, A6, A8)	A3, A10, A1→2, A5, A7, A9, A11→15
13	(A6→8), (A1→5, A10→15)	A6, A10, A9
14	(A6→8), (A1→5, A10→15)	A6, A10, A9
15	(A3→4), (A6, A8)	A3, A6, A1→5, A7, A9→13
16	(A3→5), (A6, A8)	A3, A6, A1→4, A7, A9→13

4.5 Dynamic Microgrid Boundaries Versus Static Boundaries

This section demonstrates the superiority of adaptive self-adequate microgrids with dynamic boundaries compared to static microgrids. Figure 4.13 shows the fitted PDFs for the PPF results at line 58, which connects buses 47 and 48. It is clear from the curves that during scenarios 1 and 5 (Table 4.1) there is a high probability that line 58 is heavily loaded; conversely, during scenarios 3 and 7 (Table 4.1), the probability is high that this line is weakly loaded. For the proposed methodology presented in this paper, line 58 is thus a CL only during scenarios 3 and 7. However, during scenarios 1 and 5, the microgrid represented by A5 in Figure 4.12 is no longer self-adequate. As a result, A5 needs to be merged with A4, which contains a generator connected to bus 46 and has a surplus generation for producing a generation-load balance inside the new microgrid boundary. However, if line 58 is considered a CL for all scenarios, as in the fixed boundary method, then during specific scenarios (e.g., 1 and 5) self-adequacy is not maintained because the line is heavily loaded. The microgrid boundaries selected based on the fixed boundary paradigm are therefore ineffective, since these microgrids have no generation-load balance and hence cannot supply the load during islanded conditions.

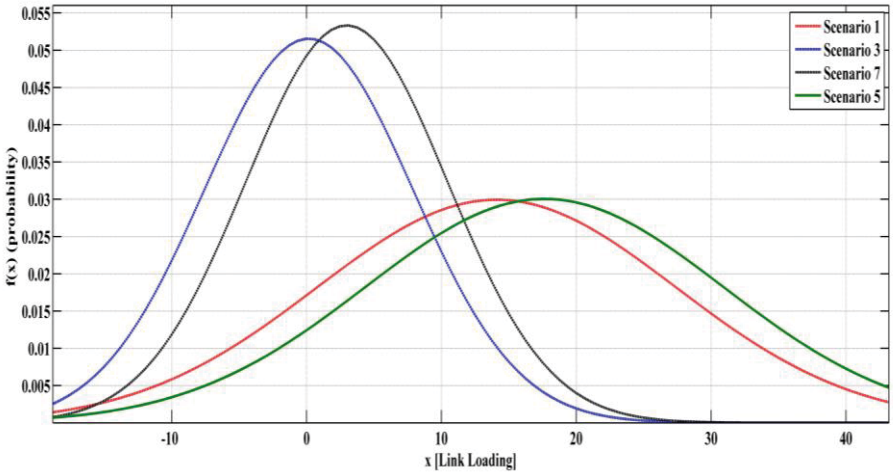

Figure 4.14: PDF for line 58 power flows during a variety of scenarios.

4.6 Discussion

This chapter has presented a novel design approach for dividing bulky existing grids into adaptive self-adequate microgrids. The proposed dynamic microgrid paradigm ensures self-adequacy at all times, taking into consideration the probabilistic nature of loads and renewable-based DGs. An appropriate number of isolation switches are allocated in order to allow the constructed microgrids to island during contingencies while supplying their loads; this feature improves reliability and prevents the spread of disturbances. The use of the proposed paradigm results in constructed microgrids that have clearly defined electrical borders, islanding capability (isolation switches and self-adequacy at all times), and single-entity controllability. None of these properties can be achieved based on the previously published static boundary paradigm. An additional benefit is that adaptive self-adequate microgrids also provide a suitable environment for the application of smart grid features, such as self-healing. The results of this study clearly demonstrate the superiority of the proposed dynamic boundary technique compared to the static boundary paradigm described in the literature. The simplicity of the proposed framework and the minimal switches and agents associated with implementation constitute key positive features that will facilitate practical implementation.

On the other hand, if the system is to be extended or a new system planned, a comprehensive planning framework is needed. Such a framework should be capable of planning the system as clusters of self-adequate microgrids to continue the proposed transition from bulky systems to smart self-adequate microgrids. This planning framework is presented in Chapter 5 and illustrated using multiple case studies.

Chapter 5
Optimal Configuration of Isolated Hybrid AC/DC Microgrids

5.1 Introduction

In Chapter 4, the adaptive self-adequate microgrid concept is presented and applied to divide existing distribution systems with allocated resources into clusters of controlled microgrids. However, neither the planning of new networks as clusters of self-adequate microgrids or the allocating of required resources to achieve the adequacy were not considered. Moreover, as presented in Chapter 1, dc distribution is coming around again with the advances of power electronics and the advantages offered by dc systems for integrating renewable resources and supplying modern loads such as high-efficiency dc lighting and plug-in electric vehicles (PEV). The number of conversion stages required for the interconnection of renewable-based DGs and modern loads to dc systems is fewer than those needed for ac systems; thus, the conversion efficiency is highly improved and the cost minimized. In addition, dc systems are free of reactive power and frequency stability issues. The dc system represents an option that should be considered when planning new systems or extensions of existing systems by looking at the type of the system as a decision variable and expecting a hybrid ac-dc system configuration. The future distribution system will likely be formed from clusters of hybrid ac-dc self-adequate microgrids with interconnection convertors for power exchange.

The planning of such hybrid microgrids to minimize investment cost and improve system efficiency has not yet been considered in the literature, nor has configuration of such hybrid ac/dc microgrids. This planning framework complements our proposed vision for the power system. In this vision, the system will be constructed as clusters of self-adequate microgrids rather than bulk generation and transmission. Therefore, in Chapter 5, an efficient and generic planning model is proposed for these new systems as self-adequate isolated microgrids. The objective of the formulation is to minimize the total planning cost, i.e., the investment cost of the DER mix and the associated electronic converters, and the operational cost of the resultant microgrid. Due to the high deployment of renewable DER in self-adequate microgrids, combined renewable generation-load probabilistic scenarios are introduced to capture the intermittent nature of the load and generation in the planning model.

Meanwhile, the detailed operational philosophy and power loss of each component is considered to present actual daily power schemes at the planning stage. The outcome of this formulation not only defines the boundaries of the ac and ac microgrids (zones), but assigns the capacity of each DER in the zones as well as the capacity of the ICs between the different type zones. The term ‘zones’ will be used here instead of microgrids, as the planned zones can be operated as one microgrid or divided into several adaptive microgrids during the operation stage, using the operational planning framework presented in Chapter 4.

The remainder of this chapter is organized as follows: section 5.2 introduces an overview of the presented problem. The modelling approach of the load and renewable DER which is suitable for a planning approach is provided in section 5.3. Section 5.4 demonstrates the detailed planning formulation for the hybrid ac/dc zones, and section 5.5 highlights the numerical results for a number of different planning approaches, such as restricting the type of zones or restricting the type of DERs to show the flexibility of the proposed framework in addressing different planning situations. In addition, different topologies are studied to prove that the obtained design, with no restrictions being imposed, offers the minimum levelized cost. Finally, section 5.6 discusses the main findings of the chapter.

5.2 Statement of Problem

The rationale behind the work presented in this chapter is to optimize the configuration of newly constructed systems as isolated hybrid ac/dc zones with the consideration of comprehensive models for loading, generation, and electronic converters. In the planning model provided in [92], the active distribution system could be entirely constructed as an ac or dc network. The reactive component of the ac loads was not considered. In addition, renewable resources were neglected due to the existence of a main substation in the system. In general, isolated systems structures can be divided into zones based on ownership, load profiles (such as residential, military, and industrial), the load type majority (ac or dc) [93]–[95], and adequacy. This work employs an approach to represent the isolated system as a set of mutually exclusive zones, as illustrated in Figure 5.1. The set of neighboring zones that can exchange power with zone z is denoted as $\mathcal{N}_z$, for instance, $\mathcal{N}_{z_2} = \{z_1, z_3\}$. With the absence of a main grid, this work provides a viable tool for defining the type of different zones (ac or dc) and the installed capacity of each DG type, the ESS, and the ICs between neighboring zones with different types.

Thus, the inputs to the planning framework form a number of neighbour zones to be constructed with certain available connection links, in addition to the loading profiles for ac and dc loads in each zone. The planning framework output will be the type of each zone, size of ICs, and the required size

and mix of DER to achieve load-generation balance. The proposed planning formulation aims at minimizing the total planning cost, including the operational cost as well as the investment cost of the different DER resources. For the sake of simplicity, other costs associated with distribution network upgrades and installation of additional transformers, switches, measurement devices, and controllers are ignored in this framework since these costs will be similar in both types of zones [92].

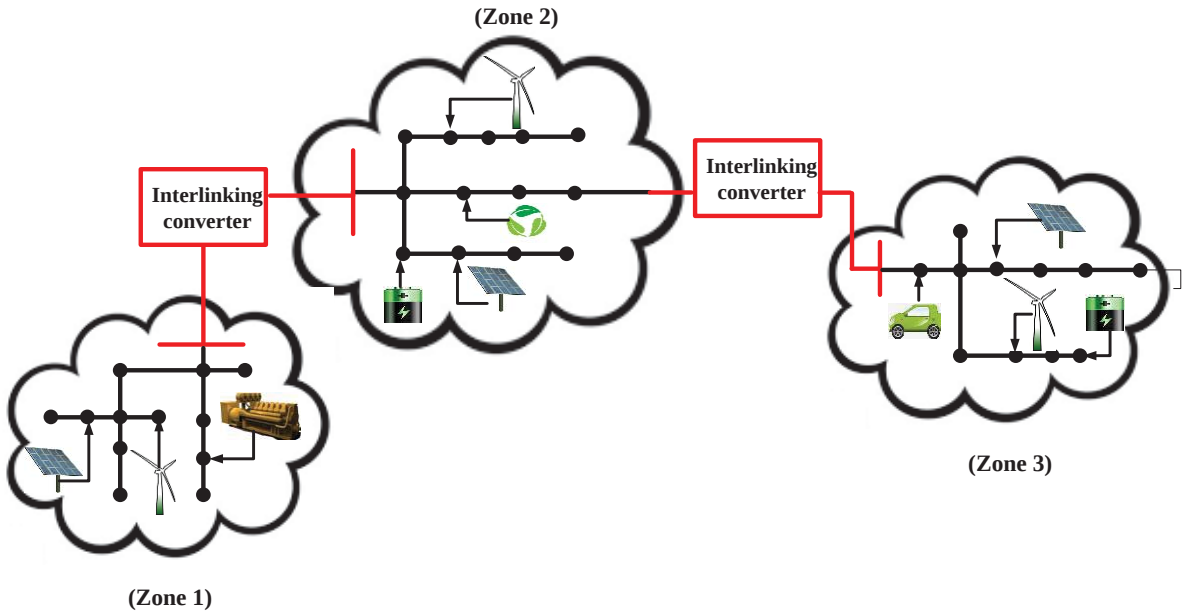

Figure 5.1 : Microgrids as mutually exclusive zones.

In order to provide a reliable planning scheme, the intermittency nature of the load demand and renewable resources is considered via different probabilistic scenarios, as demonstrated in the following section. The probabilistic scenarios used for the planning framework are based on dividing load and generation PDFs into states with certain probabilities, which is different from the MCS used for the operational planning study in Chapter 4. It is worth mentioning that the planning of hybrid ac/dc systems is a sophisticated process. On the one hand, the deployment of a specific DG type may incur additional power electronic conversion device(s) with associated power loss, according to the zone type in which the DG is installed. Figure 5.2 highlights the conversion stages to integrate DG units and loads with ac vs. dc systems (e.g., connecting an ac load in a dc zone requires an inverter). On the other hand, due to the probabilistic nature in the load and generation profiles, the adjacent zones may exchange their available excess active power. If the zones are defined with different types (i.e., ac and dc), the power transfer would be throttled by the installed IC capacity set by the planning framework.

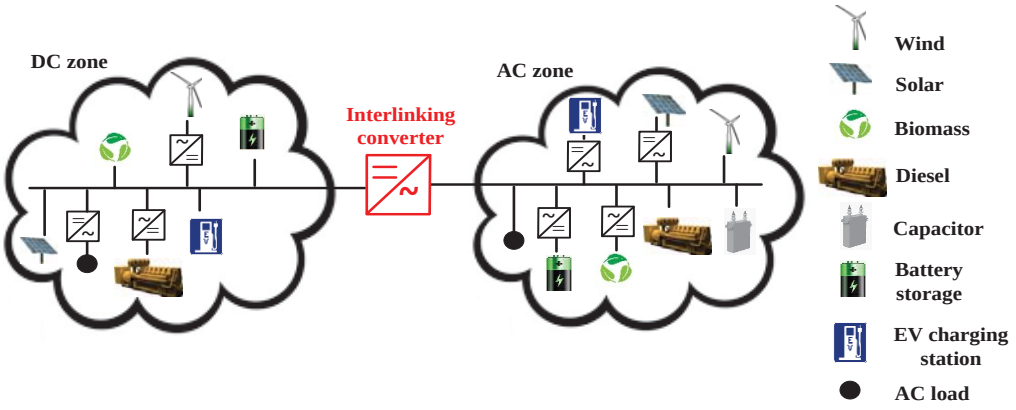

Figure 5.2: Conversion stages required to integrate DG units and loads to AC and DC zones

5.3 Probabilistic DG and Load Modelling

A successful planning strategy for isolated systems should take into consideration the probabilistic nature of both the rene`wable resources and loads. This section explains the analytical development of a combined generation-load scenario suitable for planning studies and describes all possible system states and their respective probabilities. In general, the generation states model for variable power DG units is calculated by dividing the continuous probability distribution function (PDF) into several states. These continuous PDFs are already obtained in Chapter 3. For example, the generation states model of wind-based DG units can be extracted by dividing the wind power PDF into several states with a step of 0.05 per unit. The probability of a wind state "st" can then be calculated as follows:

$$\Omega_{wind}^{st} = \int_{P_{st,min}}^{P_{st,max}} f(P)\, dv \tag{5.1}$$

where $f(P)$ is the distribution probability of wind power and P_{min}^{st} and P_{max}^{st} are the minimum and maximum power limits of state "st," respectively. Similar approaches can be used for other variable power sources. The planning studies in [26] revealed no significant differences between the results obtained using this analytical approach and those obtained using MCS.

Accordingly, the normalized power for each renewable source is divided into discrete states. The number of states for each component should be carefully selected so that the simplicity and accuracy of the analysis are not compromised: a large number of states increases accuracy but at the expense of also adding to the complexity, whereas a small number of states has the opposite effect. In this analysis, the year is represented by eight days, a weekday and a weekend for each season. At each of the presented 384 hours (2 days × 4 seasons× 24 hours), a probability $\Omega_{g,d,h}^{st}$ is defined for the states of intermittent generated power, based on the historical available data. In order to consider the correlation

between the generated powers at successive time segments, a finite-state Markov model is utilized [96]. Thus, the probability of a daily generation scenario could be calculated as

$$\Omega_{g,d}^{st} = \Omega_{g,d,1}^{st} \prod_{h=1}^{23} \Omega_{g,d,h+1|h}^{st} \tag{5.2}$$

A similar approach is applied in order to obtain the probabilities of the daily load states as

$$\Omega_{l,d}^{st} = \Omega_{l,d,1}^{st} \prod_{h=1}^{23} \Omega_{l,d,h+1|h}^{st} \tag{6.3}$$

Different loads and intermittent generation sources are uncorrelated; thus, the joint probability of a daily generation-load scenario Ω_d^{st} , describing a possible combination of generation and load states in the zone, is obtained as

$$\Omega_d^{st} = \prod_{g\epsilon\{W\}} \Omega_{g,d}^{st} \quad \prod_{l\epsilon L} \Omega_{l,d}^{st} \tag{5.4}$$

5.4 Planning Formulation for the Hybrid system

The proposed formulation is a nonlinear mixed integer problem, according to which the system designer could assign the ac and dc zones and the capacity of the capacitors, rectifiers, inverters, ESS and DG units. For each zone, a set of decision variables is defined as follows: the zone type (ac or dc), sizes of the ESS and different DG units, and sizes of the installed rectifiers and inverters in the zone. The sizes of the ICs connection between the neighboring zones are introduced as well. The zone type is defined as a binary variable and takes a value of zero for the dc option and a value of one for the ac option. By considering single-step price curves, which could be simply extended to multistep price curves, the other control variables are continuous, with values higher than or equal zero.

5.4.1 Problem Objective

The objective of this work is to minimize the microgrid total levelized planning cost (5.5), which comprises the levelized investment and operational costs:

$$\min\ IC + \sum_{d} \mathrm{u_d} \sum_{st} \Omega_d^{st}\ OC_{st,d} \tag{5.5}$$

The levelized investment cost, the first term in (5.5), represents the annual investment cost of the DG, ESS and the electronic power converters. More details regarding these items are provided in the following subsection. The second term in (5.5) represents the levelized operational cost for a year. As stated above, the year is represented by eight days with different scenarios. The first summation

contemplates the occurrence probability of the different scenarios, while the second considers the weight of the day during the year. The constant u_d for each of the eight days takes a value of 65.22 (365.25/4 day/season × 5/7 weekdays/week) for weekdays and a value of 26.089 (365.25/4 day/season × 2/7 weekends/week) for weekends.

5.4.1.1 Levelized investment costs

It is important to recall that the investment costs are levelized in this analysis to be represented on an annual basis for the various microgrid components. The levelized cost is related to the net present value of the total investment cost, which includes capital, installation and maintenance costs, as follows [97]:

$$Levelized\ Cost = Total\ invest\ ment\ cost\ \times CRF\ (i, y) \tag{5.6}$$

with

$$CRF\ (i, y) = \frac{i\ (1+i)^y}{(1+i)^y - 1} \tag{5.7}$$

where CRF is the capital recovery factor, y is the lifetime of the component, and i is the discount rate.

The type of the zone within the microgrid (i.e., either ac or dc) would impact the components to be installed in this zone and alter the investment cost accordingly. However, both ac and dc microgrids still have the same basic costs for the ESS and DG components. The levelized investment cost could thus be divided into four items (5.8-5.12): the basic installation costs (IC'_z), costs associated with ac zones ($IC_{ac,z}$), costs associated with dc zones ($IC_{dc,z}$), and ICs cost (IC_t).

$$IC = \sum_z \left(IC'_z + M_z IC_{ac,z} + (1 - M_z)\ IC_{dc,z}\right) + \sum_t (M_z - M_{z'})^2\ IC_t \tag{5.8}$$

$$IC'_z = \sum_{g \in \{F,W\}} \left(CP_{zg} P_{zg}^{cap}\right) + CP_{zB} P_{Bz}^{cap} + CE_{zB} SoC_{Bz}^{cap} \tag{5.9}$$

$$IC_{ac,z} = \sum_{g \in \left\{ \substack{F_{dc'} \\ W_{dc'B}} \right\}} CI\ P_{zg}^{cap} + \sum_{l \in L_{dc}} CR\ P_{zl}^{max} + CQ\ Q_z^{cap} \tag{5.10}$$

$$IC_{dc,z} = \sum_{g \in \{F_{ac}, W_{ac}\}} CR\ P_{zg}^{cap} + \sum_z \sum_{l \in L_{ac}} CIS_{zl}^{max} \tag{5.11}$$

$$IC_t = \ CT\ S_{t,zz'}^{cap}, \tag{5.12}$$

The basic installation cost comprises the levelized investment cost of the DG and ESS units in different zones, disregarding the zone type (5.9). It is worth noting that the ESS levelized investment cost is defined according to its maximum power and maximum state of charge (SoC). The installation

cost of an ac zone ($IC_{ac,z}$) incurs the levelized investment cost of power conversion units (5.10): inverters to adapt the output power of the ESS and dc-based DG units and rectifiers to feed the dc loads. The costs of the additional capacitors, which provide the system with the VAR required in heavy loading conditions, are included as well in (5.10). Since $IC_{ac,z}$ is defined only for ac systems, this term is excluded from the total investment cost for dc zones through multiplying $IC_{ac,z}$ by M_z in (5.8). In contrast, the installation of rectifiers and inverters is mandatory for the energy conversion of ac-based DG units and loads, respectively, in dc zones (5.11). The levelized investment cost of these devices is multiplied by $(1 - M_z)$, to exclude the ac zones, and is then added to the total investment cost (5.8). Finally, the levelized costs of interlinking converts between the neighboring zones are only considered for the ones that connect ac and dc zones (5.12).

5.4.1.2 Daily operational costs

For each daily scenario, a twofold operational cost is defined in (5.13). The first term represents the operational cost of the fuel-based DG units, while as the second incorporates the cost of unserved energy, which reflects the users' willingness to pay in order to avoid power interruptions.

$$OC_{st} = \sum_{z}\sum_{h}\sum_{g\epsilon F} CF_g P_{zgh} + \sum_{z}\sum_{h}\sum_{l} \alpha_{zhl}\, \beta_{zhl}^{st}\, P_{zl}^{max}\, CC \qquad (5.13)$$

5.4.2 Problem Constraints

The necessary constraints are defined in this subsection. These constraints must be fulfilled for the solution of each daily scenario.

5.4.2.1 Active and reactive power sufficiency constraints

For each zone, the net summation of DG output powers, ESS injection, and imported active power from the neighboring zones must meet the load active power after considering the system power loss and spare capacity (5.14). The spare capacity is introduced to guarantee the microgrid's ability to compensate for the sudden and unpredicted increase in its local power demand (i.e., spinning reserve) [98] [99]. For an isolated microgrid, different alternatives can reflect the concept of spare capacity. In this analysis, the spare capacity is represented as a specific percentage of the load demand; 5% of the total demand is a reasonable value in isolated microgrids [99]. It is worth noting that the power loss in the system feeders is also presented as a percentage of the total demand (5% as well) [98] [26].

Similar to the active power constraints, the load reactive power must be supplied via the DG reactive

powers, the ESS inverter, the installed capacitors and the imported reactive power from neighboring zones (5.13). Since this condition is only applicable in the case of ac zones, the equation is multiplied by the integer variable M_z to relax the condition for the dc zones.

$$\sum_{g} P_{hzg}^{net} + \left(P_{hzB}^{dis\_net} - P_{hzB}^{ch\_net}\right) + \sum_{z' \in \eta_z} P_{t,zz'} = \sum_{l} \sigma_z \, \rho_z \, P_{hzl} \qquad \forall h, z \tag{5.14}$$

$$M_z Q_{hzV} + M_z \sum_{g} Q_{hzg} + M_z Q_{hzB} + M_z \sum_{z' \in \eta_z} Q_{t,zz'} = M_z \sigma_z \, \rho_z Q_{hzl} \qquad \forall h, z \tag{5.15}$$

5.4.2.2 DG constraints

The installed DG units must fulfill a set of equality and inequality constraints. It is important to highlight that if the DG type, ac or dc, does not match the zone type, additional conversion loss will be considered. According to [100], [59], the loss of power electronic converts could be represented as a quadratic function in the ac apparent power (5.16), (5.17). Thus, Equation (5.18) indicates the conversation loss in dc and ac DG units if installed in ac and dc.

$$F_c(S) = C_2 \, S^2 + C_1 S + C_0 \tag{5.16}$$

$$S_{hzg}^{net\,2} = P_{hzg}^{net\,2} + Q_{hzg}{}^{2} \qquad \forall h, z, g \tag{5.17}$$

$$P_{hzg}^{loss} = \begin{cases} M_z \, F_c\left(S_{hzg}^{net}\right) & \forall h, z, g \in \{F_{dc}, W_{dc}\} \\ (1 - M_z) F_c\left(P_{hzg}\right) & \forall h, z, g \in \{F_{ac}, W_{ac}\} \end{cases} \tag{5.18}$$

$$P_{hzg} = P_{hzg}^{loss} + P_{hzg}^{net} \qquad \forall h, z, g \tag{5.19}$$

$$P_{zg}^{min} \leq P_{hzg} \leq P_{zg}^{cap} \qquad \forall h, z, g \in \{F\} \tag{5.20}$$

$$0 \leq P_{hzg} \leq \gamma_{hg}^{st} \, P_{zg}^{cap} \qquad \forall h, z, g \in \{W\} \tag{5.21}$$

$$S_{hzg}{}^{2} = P_{hzg}{}^{2} + M_z Q_{hzg}{}^{2} \qquad \forall h, z, g \tag{5.22}$$

$$0 \leq Q_{hzg}, S_{hzg} \leq P_{zg}^{cap} \qquad \forall h, z, g \tag{5.23}$$

5.4.2.3 Capacitors constraints:

The output reactive power of the capacitors must be less than their installed capacity:

$$0 \leq Q_{hzV} \leq Q_{hzV}^{cap} \qquad \forall h, z \tag{5.24}$$

5.4.2.4 Load constraints

The following load constraints count for the load curtailment and power loss in electronic converters, if implemented. In considering the load curtailment ratio (5.27), the net supplied active and reactive powers are indicated in (5.25) and (5.26), and the net apparent power is calculated in (5.28). The active power supplied by the system is obtained in (5.30) by adding the net load power to the power loss associated to the power conversion (5.29).

$$P_{hzL}^{net} = (1 - \alpha_{zhl})\beta_{zhl}^{st}\, P_{zl}^{max} \qquad \forall h, z, l \qquad (5.25)$$

$$Q_{hzL} = (1 - \alpha_{zhl})\beta_{zhl}^{st}\, Q_{zl}^{max} \qquad \forall h, z, l \in \{L_{ac}\} \qquad (5.26)$$

$$0 \leq \alpha_{zhl} \leq 1 \qquad \forall h, z, l \qquad (5.27)$$

$${S_{hzl}}^2 = {P_{hzL}^{net}}^2 + {Q_{hzl}}^2 \qquad \forall h, z, l \in \{L_{ac}\} \qquad (5.28)$$

$$P_{hzL}^{loss} = \begin{cases} M_z\, F_c(P_{hzl}) & \forall h, z, l \in \{L_{dc}\} \\ (1 - M_z)F_c\left(S_{hzg}\right) & \forall h, z, l \in \{L_{ac}\} \end{cases} \qquad (5.29)$$

$$P_{hzL} = P_{hzL}^{net} + P_{hzL}^{loss} \qquad \forall\, h, z, l \qquad (5.30)$$

5.4.2.5 ESS Constraints

The net charging and discharging power of the installed ESS are related via complementary constraints (5.31) because the ESS could only charge or discharge at any time segment. For ac zones, an additional inverter is installed to adapt the ESS output power to ac. This inverter could support the system reactive power, so the net apparent power of the ESS is calculated in (5.32). The inverter loss could be due either to charging or discharging the ESS in the ac zones only, as demonstrated in (5.33). Relating the ESS power to the net power with the consideration of the inverter loss requires a careful understanding. In other words, a power loss due to discharging does not represent the difference between the ESS charging and the net charging powers. Complementary constraints are utilized to handle the problem (5.34), (5.35). In (5.36), the maximum limit of the ESS active, reactive, and apparent powers are maintained. The change in the SoC is calculated, as indicated in (5.37), based on the charging and discharging powers, where the efficiency of charging and discharging cycles is manipulated through η_{ch} and η_{dis} terms. Finally, the SoC for the ESS must be within a permissible minimum; 30% of the installed capacity is considered in the work, along with the ESS maximum SoC capacity.

$$0 \leq P_{Bzh}^{ch\_net} \perp P_{Bzh}^{dis\_net} \geq 0 \qquad \forall h, z \qquad (5.31)$$

$${S_{hzB}^{net}}^2 = \left(P_{hzB}^{dis\_net} - P_{hzB}^{ch\_net}\right)^2 + {Q_{hzB}}^2 \qquad \forall h, z \qquad (5.32)$$

$$P_{hzB}^{loss} = M_z\, F_c\left(S_{hzg}^{net}\right) \qquad \forall h, z \qquad (5.33)$$

$$0 \le P_{Bzh}^{ch} \perp -P_{hzB}^{ch,net} + P_{hzB}^{loss} + P_{hzB}^{ch} \ge 0 \qquad \forall h, z \qquad (5.34)$$

$$0 \le P_{Bzh}^{dis} \perp P_{hzB}^{dis,net} + P_{hzB}^{loss} - P_{hzB}^{dis} \ge 0 \qquad \forall h, z \qquad (5.35)$$

$$0 \le P_{Bzh}^{ch}, P_{Bzh}^{dis}, Q_{hzB}, S_{hzB}^{net}, \le P_{zB}^{cap} \qquad \forall h, z \qquad (5.36)$$

$$SoC_{Bzh+1} = SoC_{Bzh+}\left(P_{Bzh}^{ch}\eta_{ch} - P_{Bzh}^{dis}/\eta_{dis}\right) \qquad \forall h, z \qquad (5.37)$$

$$SoC_{zB}^{min} \le SoC_{hzB} \le SoC_{zB}^{cap} \qquad \forall h, z \qquad (5.38)$$

5.4.2.6 Power transfer between neighboring zones

It is important to note that an IC is assumed between each two neighboring zones. Based on the zonal type, this IC may or may not affect the power transfer between the zones. For each zone, the apparent power imported from its neighbor is calculated as illustrated in (5.39). The power loss in the IC is represented using (5.40); the multiplication by zone type is necessary, since the loss is a function in the apparent power in the ac side of the converter [100], [59]. In (5.41), the IC loss is incorporated to the active power transfer between the neighboring zones if defined with different types; otherwise, no power loss is considered. On the other hand, the reactive power transfer between the zones is applicable only if both zones are ac (5.42). If any of the two-neighboring zone is dc, (5.42) is relaxed, since one of the zonal types takes a zero value. The set of equations in (5.43-5.45) governs the maximum active, reactive and apparent power that a zone could exchange with its neighbor through an IC. This set of equations is not applied, i.e. relaxed, for neighboring zones of similar type.

$${S_{ht,zz'}}^2 = {P_{ht,zz'}}^2 + {Q_{ht,zz'}}^2 \qquad \forall h, t \qquad (5.39)$$

$$P_{ht,zz'}^{loss} = M_z\, F_c\left(S_{ht,zz'}\right) + M_{z'} F_c\left(S_{ht,z'z}\right) \qquad \forall h, t \qquad (5.40)$$

$$P_{ht,zz'} + P_{ht,z'z} + (M_z - M_{z'})^2 P_{ht,zz'}^{loss} = 0 \qquad \forall h, t \qquad (5.41)$$

$$\left(Q_{t,zz'} + Q_{t,zz'}\right) M_z M_{z'} = 0 \qquad \forall h, t \qquad (5.42)$$

$$-S_{t,zz'}^{cap} \le (M_z - M_{z'})^2 P_{ht,zz'} \le S_{t,zz'}^{cap} \qquad \forall h, t \qquad (5.43)$$

$$-S_{t,zz'}^{cap} \le (M_z - M_{z'})^2 Q_{ht,zz'} \le S_{t,zz'}^{cap} \qquad \forall h, t \qquad (5.44)$$

$$0 \le (M_z - M_{z'})^2\, S_{ht,zz'} \le S_{t,zz'}^{cap} \qquad \forall h, t \qquad (5.45)$$

5.5 Case Studies

The illustrative system shown in Figure 5.1 is used to validate the proposed planning framework. This system is comprised of three zones with two available interconnection ties. Each zone has combined ac and dc loads. The load normalized power profiles are known in addition to the wind and solar profiles. However, the type of the microgrid (i.e., ac or dc) as well the type of the intertie (i.e., IC or direct connection) will be determined by the planning framework.

In addition, the generation mix for each microgrid will be set by the framework. The generation mix means the size of dispatchable and renewable DGs of ac and dc types. As shown in Figure 5.2, the type of zone determines the way the load and generation are connected, which is reflected in the proposed planning framework by the added converter stages cost. Similarly, the type of neighbor microgrids will set the type of the intertie connection, whether a direct link or an IC, while the framework will set the size of the IC based on the power interchange capacity.

The probabilistic nature of load and renewable-based generation is a critical factor in the results obtained from the planning problem. This probabilistic nature necessitates the optimization formulation of the problem, as the design is not straightforward. The historical data for wind speed and solar irradiance [101] are used to calculate the normalized power profiles for renewable-based generation in different microgrids (zones). In addition, the residential, commercial and industrial load profiles [102] are combined and used to represent the ac and dc load profiles inside the different zones. A typical one-day profile for different loads and generations of normalized power is shown in Figure 5.3. These profile data will be used to model the probabilistic behavior of load and generation as described in section 5.4.

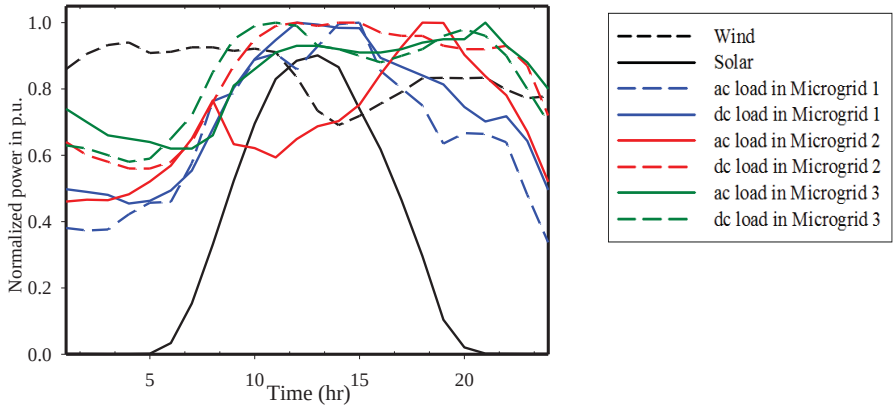

Figure 5.3 Typical daily profiles for renewable and zones loads

In addition, the capital and O&M costs [103] for different types of generation presented in Table 5.1 are used for sizing the units allocated in any of the zones.

Table 5.1 Levelized Costs for Different Types of Generation

Generation Type	Capital $/MWh	Fixed O&M $/MWh	Variable O&M $/MWh
Wind	42.1	13.4	NA
Solar	66.9	9.9	NA
AC Dispatchable	12.3	1.4	35.2
DC Dispatchable	36.3	6.5	50.2

The optimal configuration of the system presented in Figure 5.1 is investigated using the proposed planning framework. The resulting optimal configuration with the minimum investment and O&M cost is M_z ={0, 1, 1}. This optimal configuration sets the first zone as dc with IC connection to zone 2, while both zones 2 and 3 are of ac type with direct link connections. The proposed framework outputs the optimal energy resources mix (i.e., generation, energy storage and capacitor) that satisfy the load generation balance for both active and reactive power. Figure 5.4 shows the optimal energy resources mix for each zone. In order to study the effectiveness of the proposed planning framework, two other configuration scenarios are examined. To this end, the system layout is assumed to be either all dc (scenario a, Mz ={0, 0, 0}) or all ac (scenario b, Mz ={1, 1, 1}).

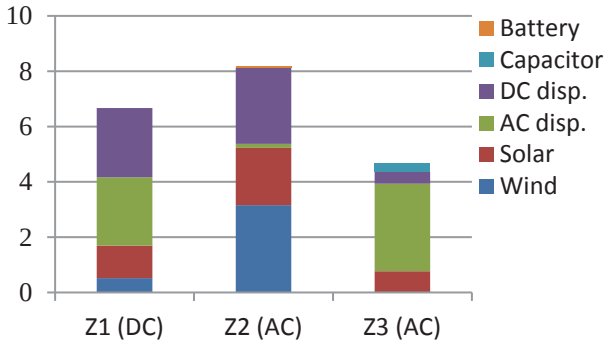

Figure 5.4: Optimal energy resource mix for different zones loads.

For each scenario, the planning framework will set the optimal energy resource mix to satisfy the adequacy constraints with minimal investment and O&M cost. The costs of these scenarios are compared to those of the optimal system configuration obtained previously, as presented in Table 5.2.

Table 5.2 Levelized Investment and O&M Costs for Different System Configurations

Optimal [M_z ={0,1,1}]	Scenario a [M_z ={0,0,0}]	Scenario b [M_z ={1,1,1}]
$1.3319 M	$1.5221 M	$2.4439 M

The results show the effectiveness of the proposed planning framework in obtaining the minimal cost system configuration. Moreover, the optimal energy resources mix to achieve load generation balance for both active and reactive power during each scenario is shown in Figure 5.5.

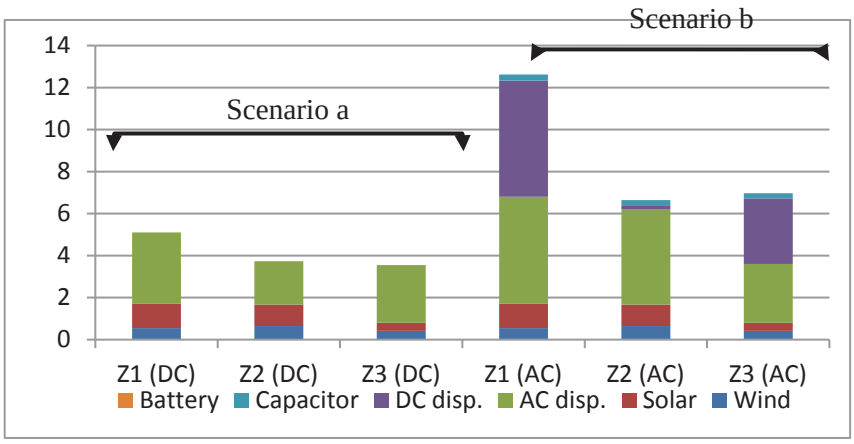

Figure 5.5: Optimal energy resources mix for different system configurations.

As is evident from the results obtained in Figure 5.5, the optimal energy resources mix for a defined system configuration remains challenging and depends on the probabilistic nature of load and generation as well as capital and O&M costs. For scenario a, although all the microgrids are dc, the ac dispatchable DGs were found to be less costly compared to dc dispatchable. Moreover, in order to verify the obtained findings, the planning framework was applied to the system with all zones being forced to be of ac type, while the size of dc resources was forced to zero by added constraints (scenario c). The optimal ac energy resources mix obtained for this case is shown in Figure 5.6. The levelized investment and O&M cost for such an energy mix is found to be 2.9798M$ compared to the optimal case of $2.4439 M, as presented in Table 5.2.

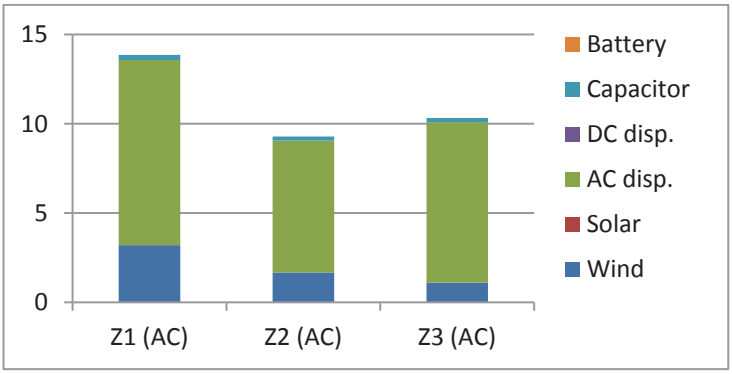

Figure 5.6: Optimal ac energy resource mix for scenario c.

Isolated zone case

To prove the flexibility of the proposed planning framework in planning an isolated system which has interconnected zones as well as totally isolated zones, a system with an isolated zone and two interconnected zones is assumed, as shown in Figure 5.7. The proposed planning framework was applied to the system and the optimal energy resources mix for this layout is presented in Figure 5.8. The levelized investment and O&M cost associated with this design is $2.3617 M. The battery storage became more feasible in the case of isolated zones, as shown from the obtained results for this case study, with a battery sized only for zone 1 to achieve self-adequacy. The interconnection allows for shared supply assets between zones and interchange power for balancing load and generation instead of installing energy storage, if the investment cost for added generation is cheaper.

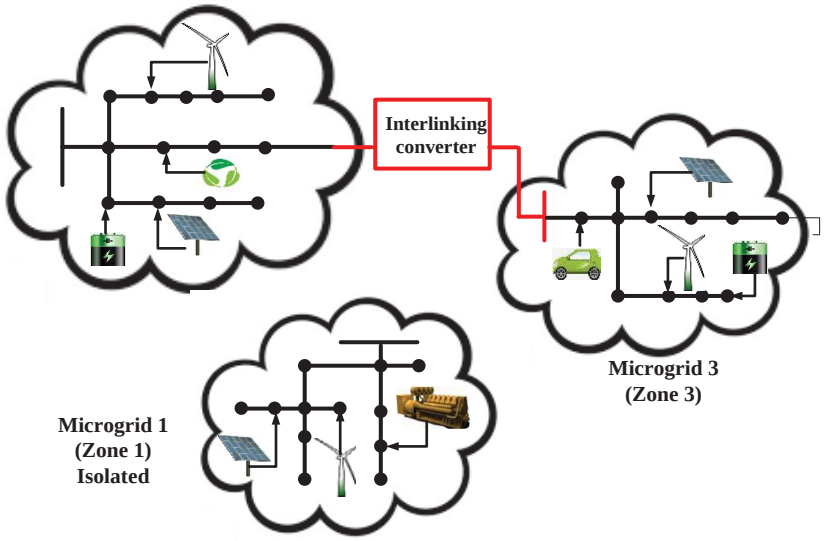

Figure 5.7: System with an isolated zone.

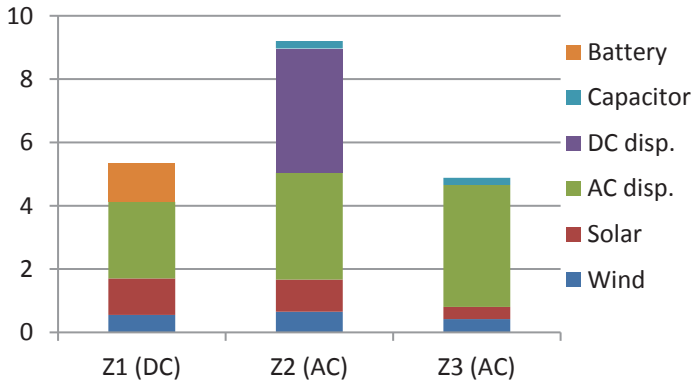

Figure 5.8: Optimal energy resources mix for the system with zone 1 isolated.

5.6 Discussion

In Chapter 5, a planning framework for hybrid an ac-dc isolated system composed of a number of interconnected zones was demonstrated. The proposed framework considers the probabilistic characteristics of both load and renewable generation. The inputs for the framework are the historical load and renewable generation data, capital cost of energy resources, O&M cost of energy resources, and the available interconnections between zones. This planning scheme aims broadly at satisfying the power balance constraints with minimum levelized costs. The control variables of the framework are the energy resources mix, type of microgrid, size of energy storage size, size of capacitors, and size of IC. It is noteworthy that all of the components' practical constraints, such as those related to DGs, battery energy storage, capacitors, etc., were modelled and considered in the framework. At the same time, the installation and running costs were considered when defining the objective function.

As well in this chapter, several case studies were investigated to show the effectiveness of the proposed planning scheme in configuring hybrid microgrids. Evident by the obtained results, these case studies imply the importance of formulating the planning problem as an optimization problem rather than setting zone type and energy mix based on the type of aggregated load and generation regardless of their intrinsic probabilistic behavior. The planning framework proposed here considers a newly constructed system to be self-adequate and isolated. This framework plans the system as interlinked hybrid zones. Therefore, the operational planning of Chapter 4 can be used to operate these zones as clusters of self-adequate microgrids during different scenarios. Applying these approaches for existing systems and the newly constructed system will achieve the transition from bulky grids to smart microgrids.

Chapter 6

Branch-Based Power Flow Algorithm for Islanded AC and Hybrid AC/DC Microgrids

6.1 Introduction

Chapter 4 addresses the formation of self-adequate microgrids for an existing system and the main challenges that may arise in operating the clustered microgrids as a single entity in either islanded or grid-connected modes. The increasing interest in dc distribution as a candidate host for a variety of different types of renewable energy generation, energy storage and load technologies necessitated the consideration of planning hybrid ac/dc microgrids over ac only. Chapter 5 discusses the planning of new hybrid self-adequate microgrids with the minimum levelized cost. However, in addition to these planning scenarios, the operation of the constructed microgrids is still a challenging task, especially with the proposed distributed agents and changeable boundaries accompanied these planning models. Therefore, developing a novel load flow analysis tool that is compatible with the proposed microgrid planning strategies to ensure the proper operation of these microgrids is required. If the clustered microgrids operate in a grid-connected mode, the conventional branch-based load flow analysis can be used, as discussed in Chapter 3. However, if the connection with main grid is lost, the clustered microgrids will operate in islanded mode to supply most of the load, based on the available generation capacities.

In islanded microgrids, dispatchable DGs are droop-controlled to ensure proper load-sharing among DGs. For ac microgrids clustered from existing systems (as discussed in Chapter 4), active power is controlled through a frequency signal, while a voltage signal is used to control reactive power. Accordingly, the appropriate load flow analysis tool for such microgrids should consider the following: the variable microgrid frequency, the absence of a slack bus, and the shared DGs' responsibility for reactive power. In addition, this tool should be simple, decentralized, and fast in order to fit the proposed operational strategy. Moreover, the tool should be extended to handle the islanded hybrid microgrid case to accommodate the evolving dc distribution systems.

In dc microgrids, similar to ac microgrids, DG injected power is controlled via a voltage signal. On the other hand, the interconnection between dc and ac microgrids is done through an IC. The IC is

usually controlled to mimic a droop control characteristic to allow load-sharing between the DGs located in both the dc and ac microgrids. This behavior is achieved through linking the frequency of the ac microgrid to the voltage of the dc microgrid. Therefore, this chapter describes a branch-based power flow for islanded ac and hybrid ac-dc microgrids. Unlike the Newton-Raphson (NR) methods, the proposed algorithm is derivative-free and matrix-free, and thus is simple, fast, and does not suffer the high R/X ratio ill-condition effects in the calculations of inverse Jacobian.

Moreover, the proposed algorithm eliminates the dependency of branch-based techniques on having a slack bus and considers droop-controlled DGs in both ac and dc microgrids. A forward/backward sweep-based algorithm is developed for the ac microgrids and dc microgrids, and then extended to the hybrid ac-dc microgrids. For the hybrid case, the solution is divided into two sub-problems solved sequentially and considering the characteristics of the IC. The proposed algorithm inherits the superiority of branch-based techniques over NR in convergence, computational burden, and execution time. The application of the proposed algorithm for the adaptive self-adequate microgrid is discussed in the following sections.

The remainder of the chapter is organized as follows. Section 6.2 provides a detailed overview of the problem description and challenges. The novel FBS power flow for ac microgrids is provided in sections 6.3 and then generalized in section 6.4 to handle large systems. The algorithm execution is illustrated with a case study that considers the typical IEEE 38-bus system in section 6.5. In section 6.6, the proposed power flow algorithm is extended for the islanded hybrid ac-dc microgrid case. Section 6.7 describes the application of the proposed algorithm in studying the number of case studies, specially the application to the adaptive-self adequate microgrids case, and section 6.8 discusses the chapter's findings.

6.2 Problem Definition

With the well-known forward/backward sweep (FBS), the existence of a slack bus is a prerequisite for calculating the voltages – and hence the power flows – in a system. The voltage magnitude of the slack bus is known and constant, and the system frequency is thus also known and constant. The voltages at the remaining buses are then updated (in the backward sweep calculations) according to this slack bus voltage, which modifies the voltages of all the other buses based on the drop resulting from the flows in the lines calculated in the forward sweep.

To solve the power flow for microgrids in grid-connected mode, the PCC is used as the slack bus.

This point is considered the reflection point – that is, the point at which the algorithm switches from backward to forward calculations. It is also the pivot point, or the point that modifies the system voltages. However, during islanded mode, no slack bus is available to provide either a reflection point during the forward phase of the calculations or a pivot point in the voltage calculations. In addition, the microgrid's frequency is unknown.

The novelty of the proposed FR-FBS technique is based on the use of the PCC as the reflection point, with any point connected to a droop-controlled DG being employed as the pivot point for the purpose of voltage calculations in the absence of a conventional slack bus. The active and reactive power calculated at the PCC should be zero during islanded operating mode because no power is being exchanged with the grid. The reactive power at this point is hence the reactive power mismatch Q_{err} and is related to the error in bus voltages. This mismatch can therefore be used to update the voltage of the pivot point accordingly, based on the $V - Q$ droop. The active power mismatch P_{err} can also be applied for modifying the frequency of the islanded microgrid using the $\omega - P$ droop. It should be noted that P_{err} and Q_{err} are assumed to be injected from the microgrid to the grid and hence are negative if the total supply from the DGs is less than the total consumption. The main advantages of the proposed methodology can be summarized in the following:

- The dealing of the unknown microgrid frequency in the presence of droop-controlled DGs.
- The handling of the absence of a slack bus for the voltage calculations in the presence of droop-controlled DGs sharing the reactive power.
- The formulation of simple power flow equations in frequency dependent forms suitable for smart micrgrid applications.
- The designing of a novel directed solution algorithm in order to facilitate the application of the FBSs concepts in the isolated microgrid case and the proposal of the inter-iteration variables update methodology to guarantee convergence.

The proposed methodology for addressing these challenges is explained in the following subsections.

6.2.1 Frequency Calculations

As presented in (6.1), for steady-state analysis, the frequency is related to the active power P with the slope m_p, which is dependent on the DG rating:

$$\omega_i = \omega_{ref,i} - m_{p,i} P_i \tag{6.1}$$

In the case of multiple DGs, at the operating point, all of the DGs operate at the same frequency.

$$P_{total} = \sum_{i=1}^{N_{dg}} (\omega_{ref,i} - \omega) \frac{1}{m_{p,i}} = \sum_{i=1}^{N_{dg}} (1 - \omega_{cor,i}) \frac{\omega_{ref,i}}{m_{p,i}} \quad (6.2)$$

$$\omega_{cor,i} = \frac{\omega}{\omega_{ref,i}} \quad (6.3)$$

Because all DGs usually have the same reference frequency ω_{ref} and hence the same ω_{cor}, the equations can be simplified as follows:

$$P_{total} = (1 - \omega_{cor}) \frac{\omega_{ref}}{m_{p,eq}} \quad (6.4)$$

$$m_{p,eq} = \frac{1}{\sum_{i=1}^{N_{dg}} \frac{1}{m_{p,i}}} \quad (6.5)$$

where P_{total} is the total active power from droop-based DGs, ω_{ref} is the reference frequency, $m_{p,eq}$ is the equivalent droop slope, ω is the operating frequency, ω_{cor} is the frequency correction ratio, and N_{dg} is the total number of droop-based DGs. Equations (6.4) and (6.5) thus show the relation between the total active power injected from the DGs into the microgrid and the operating frequency. If the DGs have different reference frequencies, (6.2) can be used in the algorithm instead. However, because $\omega_{ref,i}$ is known for all DGs, this change has no effect on the solution approach.

In the context of the iterative solution,

$$\omega_{cor,k} = \frac{\omega_k}{\omega_{ref}} \quad (6.6)$$

Figure 6.1 illustrates the relation between the total power and the operating frequency when DGs with different droop characteristics are considered. The active power mismatch calculated at the reflection point is the error between the total DG supply and the total microgrid consumption. This P_{err} is used for updating the frequency during the solution iterations, as follows:

$$\omega_{err,k} = m_{p,eq} \, P_{err,k} \quad (5.7)$$

$$\omega_{cor,k+1} = \omega_{cor,k} + \frac{\omega_{err,k}}{\omega_{ref}} \quad (5.8)$$

At the operating point, P_{err} converges to zero so that ω_{err} is zero and the microgrid frequency is known.

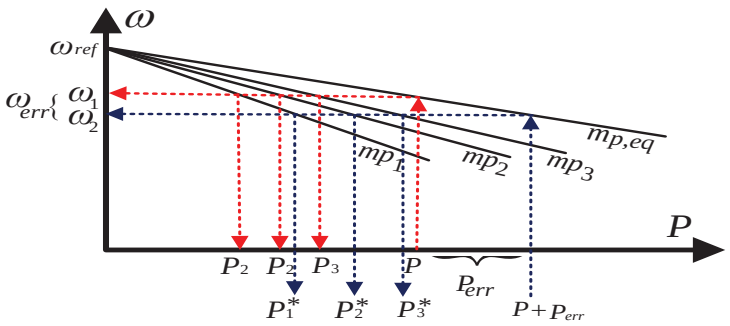

Figure 6.1: Relation between the active power mismatch and the error in the angular frequency of the microgrid.

6.2.2 Voltage Calculations

In (6.9), the voltage droop relates the voltage magnitude to the reactive power Q with the slope m_q, which is dependent on the DG rating:

$$V_i = V_{ref,i} - m_{q,i} Q_i \tag{6.9}$$

In the case of multiple DGs, the total injected reactive power from the DGs can be calculated as:

$$Q_{total} = \sum_{i=1}^{N_{dg}} \frac{(V_{ref,i} - V_i)}{m_{q,i}} \tag{6.10}$$

With respect to the calculation of the voltage at the operating point, the voltages at the DG terminals are not identical, due to network impedances and flows. The calculation of the voltages is therefore not as straightforward as that of the frequency, and thus the handling of the $Q - V$ droop is challenging and different from the $P - \omega$ droop.

$$\frac{\partial \omega}{\partial \mathrm{P_i}} = -\mathrm{m_{p,i}} \tag{6.11}$$

$$\frac{\partial \mathrm{V_i}}{\partial \mathrm{Q_i}} = -\mathrm{m_{q,i}} \tag{6.12}$$

Based on (6.10) and (6.11), the frequency can be regulated by an active power signal and the voltage can be regulated with a reactive power signal. However, ω can be updated globally, while V should be updated locally at each bus. Added to this is the fact that the bus voltages are related to each other through the KVL and KCL equations (network equation), so updating one voltage will eventually update all others. In this case, controlling the voltage with a reactive power signal is correct, but the challenge is how to handle this control: This is where the novelty of the proposed algorithm lies.

The proposed methodology aims to select only one DG point, called the pivot point, to be updated based on the reactive power mismatch. Updating one point and sweeping FB will update all the other

points and hence calculate the voltages at all buses. Afterwards, when the voltages are known, the $Q - V$ droop at each node can be used to calculate the reactive value locally and then sweep back.

The pivot point voltage is updated according to ρ $Q_{mismatch,k}$. This ρ factor is a ratio factor and is calculated based on the rating of the pivot point DG with respect to other DGs in the system (equation 6.14). In essence, a portion of the mismatch is added to the pivot point voltage. However, if one DG voltage converges to the operating point, all of the other voltages will converge, as in a traditional forward-backward sweep with a slack bus. Based on this consideration, the reactive power mismatch at the reflection point is used for updating the voltage of one bus connected to a droop-controlled DG; this point is the pivot point that will change all of the system voltages accordingly. If the pivot point voltage converges to the operating point, the reactive power mismatch converges to zero.

$$V_{pivot,k+1} = V_{pivot,k} + \rho\, m_q Q_{err,k} \tag{6.13}$$

where the DG at the pivot point has a reactive power share ratio ρ and is calculated as follows:

$$\rho = \frac{S_{pivot,max}}{\sum_{i=1}^{N_{dg}} S_{i,max}} \tag{6.14}$$

6.2.3 Power Flow Calculations

In the proposed FR-FBS, the active and reactive branch power flows rather than the currents or impedances are employed for the FBS calculations [104]. The power flow equations are formulated in a simple way without any complex number calculations, matrix formulation, or matrix inversion. Hence, it is suitable for smart grid applications with distributed agents that have limited computational capabilities.

For the simple two-bus system shown in Figure 6.2, (6.15)−(6.20) are used to calculate the active and reactive line flows as a function of the starting bus voltage magnitude, the line impedance, the microgrid frequency, and the loading of the starting bus (*j* in this case). In contrast, (6.21)−(6.24) are used for calculating the bus voltage magnitude and angle, given the active and reactive line flows and the voltage magnitude at the starting bus (*i*, in this case).

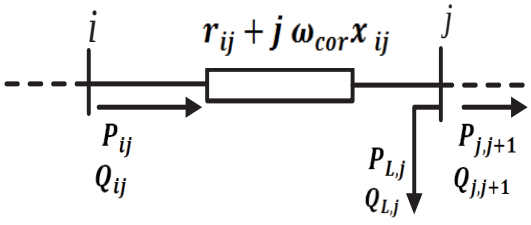

Figure 6.2: Simple two-bus network.

$$P_{i,j,k} = P_{j,k} + P_{Loss(i,j,k)} \quad (6.15)$$

$$Q_{i,j,k} = Q_{j,k} + Q_{Loss(i,j,k)} \quad (6.16)$$

$$P_{j,k} = P_{j,j+1,k} + P_{L,j,k} \quad (6.17)$$

$$Q_{j,k} = Q_{j,j+1,k} + Q_{L,j,k} \quad (6.18)$$

$$P_{Loss(i,j,k)} = r_{ij} \frac{(P_{j,k})^2 + (Q_{j,k})^2}{|V_{j,k}|^2} \quad (6.19)$$

$$Q_{Loss(i,j,k)} = \omega_{cor,k}\, x_{ij} \frac{(P_{j,k})^2 + (Q_{j,k})^2}{|V_{j,k}|^2} \quad (6.20)$$

$$|V_{j,k}| = \sqrt{|V_{i,k}|^2 - 2(r_{ij}P_{i,j,k} + x_{ij}\omega_{cor}Q_{i,j,k}) + |I_{i,j,k}|^2 |Z_{i,j,k}|^2} \quad (6.21)$$

$$|I_{i,j,k}|^2 = \frac{(P_{i,j,k})^2 + (Q_{i,j,k})^2}{|V_{i,k}|^2} \quad (6.22)$$

$$|Z_{i,j,k}|^2 = (r^2{}_{ij} + (\omega_{cor,k}x_{ij})^2) \quad (6.23)$$

$$\delta_{j,k} = \delta_{i,k} + \tan^{-1} \frac{r_{ij}Q_{i,j,k} - x_{ij}\omega_{cor,k}\, P_{i,j,k}}{|V_{i,k}|^2 - (r_{ij}P_{i.j.k} + x_{ij}\omega_{cor,k}\, Q_{i,j,k})} \quad (6.24)$$

These equations are used alternatively in the forward and backward calculations, depending on which variables are known and which are unknown.

6.3 FR-FBS Algorithm

The conventional backward/forward sweep starts the backward sweep until it reaches the slack bus, which has a known voltage, and then solves the forward sweep. This process is iterated backward and forward until convergence is reached. The process is solely based on having a slack bus. For isolated microgrids, in the absence of a slack bus, a new methodology is needed to apply the FBSs concepts. Additionally, a complementary inter-iteration variables update methodology needs to be developed, which together forms the proposed novel FR-FBS algorithm. A detailed explanation and implementation of the FR-FBS algorithm can be illustrated with the use of the six-bus system shown in Figure 6.3.

This simple system was selected for the following reasons:

1- It is easy to demonstrate the proposed algorithm and its execution flow.

2- It can be built in a time-domain platform in order to compare the results. Although the system is only 6-bus, it requires extensive work and takes a long time to be built in time-domain platforms

(e.g., PSCAD/EMTDC). However, this effort can be reduced by using the proposed power flow algorithm if the required output calculates the steady-state operating point.

In this simple example, B6 is selected as the pivot point, while the virtual bus (i.e., the PCC) is chosen as the reflection point. The active and reactive power flows from B1 to the virtual bus are the active and reactive power mismatches P_{err} and Q_{err} , respectively. The microgrid is supplied from three identical DGs connected to buses B4 to B6 and has two loads connected to buses B1 and B3. The loads in this system are modelled as constant impedance loads. The parameters of the electric network, the DGs, and the load are all listed in Table 6.1.

To illustrate the FR-FBS concept, a simple graph representation of the six-bus system was developed, as shown in Figure 6.4. The graph indicates the different types of nodes (pivot, DG, reflection, and joint) and their interconnections. The arrows on the graph denote the steps of the execution of the FR-FBS methodology for this microgrid. The solution approach is based on starting from B6 (pivot node) and sweeping towards B1 (reflection node) where the mismatches are calculated, and then returning to B6 with an updated system frequency and pivot voltage based on the mismatches. These steps are repeated until the solution converges (when $P_{err,k}$ and $Q_{err,k}$ < tolerance). At the return instant, $P_{err,k}$ is used for updating the frequency of the microgrid globally and $Q_{err,k}$ is used for updating the pivot point voltage based on the droop characteristics locally. At joint nodes, an FBS is executed before the calculations are continued towards the reflection point to update bus voltages based on the iteration's pivot voltage.

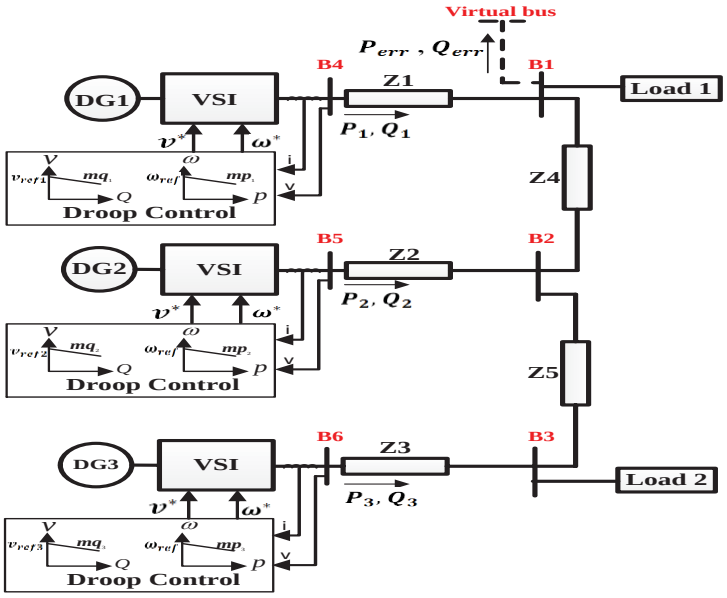

Figure 6.3: A 6-bus microgrid.

Table 6.1 Data for 6-bus Microgrid

Parameters	Value
Network data	$Z_1 = 0.3 + j\,(0.35 \times 10^{-3} \times \omega)\ \Omega$ $Z_2 = 0.2 + j\,(0.35 \times 10^{-3} \times \omega)\ \Omega$ $Z_3 = 0.05 + j\,(0.35 \times 10^{-3} \times \omega)\ \Omega$ $Z_4 = 0.43 + j\,(0.35 \times 10^{-3} \times \omega)\ \Omega$ $Z_5 = 0.15 + j\,(0.35 \times 10^{-3} \times \omega)\ \Omega$
Load data	Load 1: $6.95 + j\,(12.2 \times 10^{-3} \times \omega)\ \Omega$ Load 2: $0.43 + j\,(0.318 \times 10^{-3} \times \omega)\ \Omega$
DG data	$m_p = 9.4 \times 10^{-5}, m_q = 1.3 \times 10^{-3}, V_{ref}, \omega_{ref}$

As explained in Figure 6.4, the algorithm starts from the pivot point (B6) and solves forward towards the reflection point, at which point the mismatches are calculated and used to update the system frequency and pivot voltage in the return phase. At each branch, i.e., at B2-B5 and B3-B4, forward/backward calculations (6.15-6.24) are carried out. This process is detailed in the pseudocode shown in Figure 6.5.

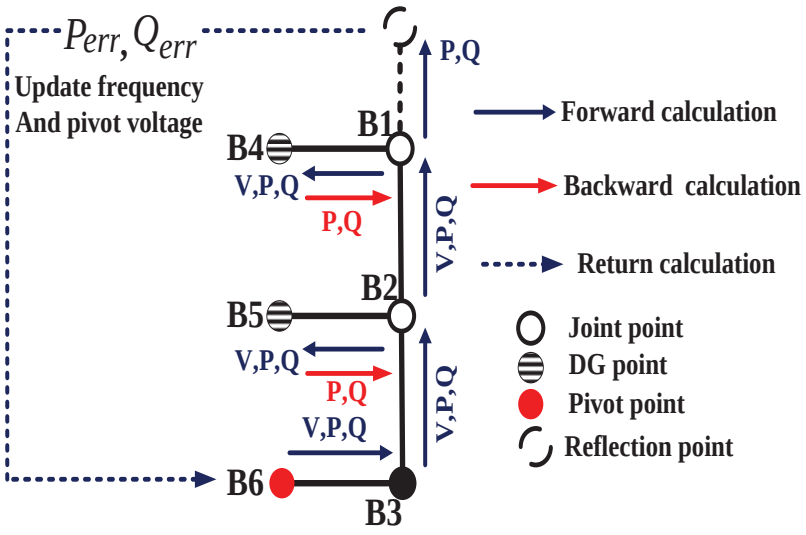

Figure 6.4: Graph representation of 6-bus system in FR-FBS context.

The proposed FR-FBS algorithm outlined in Figure 6.5 was used for solving the six-bus system, and the results obtained were compared to the PSCAD/EMTDC time domain solution, as shown in Table 6.2. The algorithm was implemented on a CPU with the following specifications: Intel core i7 860 @2.8GHz, RAM 8GB, 64 bits. The time required for running the entire algorithm was 0.72967 msec.

FR-FBS Algorithm for 6-bus Microgrid

Input DG data ($N_{dg}, m_{p,i}, m_{q,i}, Q_{i,max}, V^*, \omega^*$)) and
Network data ($z_{i,j}, A_{i,j}, N$)
Set $Pflow_{i,j,0}$, $Qflow_{i,j,0}$ to zero
$k \leftarrow 1$
Calculate initial ($P_{dg,i,k}, Q_{dg,i,k}, V_{dg,i,k}, \omega_{corr,k}$) at Pivot (B6)
Repeat{
Calculate $Pflow_{6,3,k}$, $Qflow_{6,3,k}$, $Ploss_{6,3,k}$, $Qloss_{6,3,k}$
Calculate $V_{3,k}$
Calculate $Pflow_{3,2,k}$, $Qflow_{3,2,k}$, $Ploss_{3,2,k}$, $Qfoss_{3,2,k}$
Calculate $V_{2,k}$
Calculate $Pflow_{2,5,k}$, $Qflow_{2,5,k}$, $Ploss_{2,5,k}$, $Qloss_{2,5,k}$ considering $Pflow_{2,1,k-1}$, $Qflow_{2,1,k-1}$
Calculate $V_{5,k}$
Calculate $Pflow_{5,2,k}$, $Qflow_{5,2,k}$, $Ploss_{5,2,k}$, $Qloss_{5,2,k}$
Calculate $Pflow_{2,1,k}$, $Qflow_{2,1,k}$, $Ploss_{2,1,k}$, $Qloss_{2,1,k}$
Calculate $V_{1,k}$
Calculate $Pflow_{1,4,k}$, $Qflow_{1,4,k}$, $Ploss_{1,4,k}$, $Qloss_{1,4,k}$
Calculate $V_{4,k}$
Calculate $Pflow_{4,1,k}$, $Qflow_{4,1,k}$, $Ploss_{4,1,k}$, $Qloss_{4,1,k}$
Calculate $P_{err,k}, Q_{err,k}$
$k \leftarrow k + 1$
Update $\omega_{corr,k}$ according to $P_{err,k}$
Update $V_{6,k}$ (Pivot) according to $\alpha\ Q_{err,k}$
}Until ($P_{err,k}$ **AND** $Q_{err,k}$) < tolerance
Calculate Voltage angle at B1-B6
Display Voltages, Power flows, Frequency, and DG active/reactive loading

Figure 6.5: Pseudocode for executing the FR-FBS for 6-bus microgrid.

Table 6.2 Results from FR-FBS and PSCAD/EMTDC

Bus	PSCAD/EMTDC		FR-FBS	
	Mag. (p.u.)	Ang. (degree)	Mag. (p.u.)	Ang. (degree)
1	0.9605	0.0000	0.96002	0.00000
2	0.973	-0.5270	0.97253	-0.52128
3	0.9643	-2.6850	0.96387	-2.66899
4	0.9877	-0.0725	0.98725	-0.07329
5	0.9906	-0.4520	0.99009	-0.44544
6	0.9698	-2.8690	0.96937	-2.85212

The convergence of the solution variables versus the iteration number for this 6-bus system is shown in Figure 5.6.

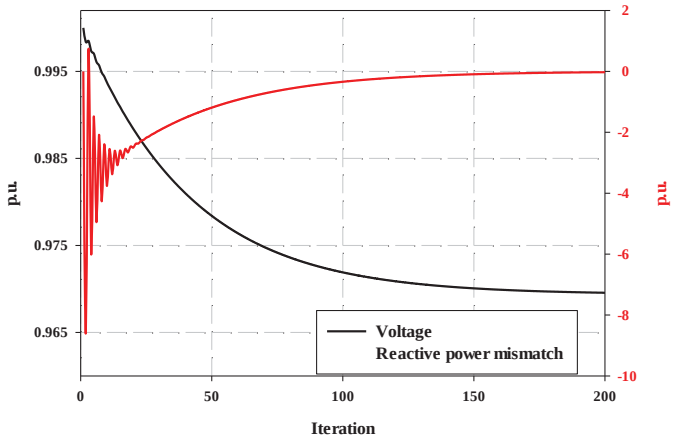

a) Voltage at pivot point and reactive power mismatch at reflection point.

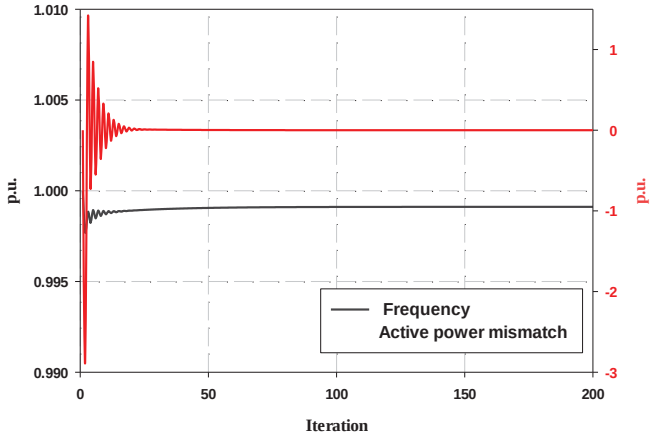

b) Frequency of microgrid and active power mismatch at reflection point.

Figure 6.6: Convergence of solution variables versus iteration number for 6-bus system.

The active and reactive power supplied from the DGs, along with the operating frequency of the microgrid, is presented in Table 6.3. Since the DGs are identical, they share the active power equally, while the reactive power share varies, since the DG terminal voltages differ according to network parameters. This proves the success of the proposed algorithm in handling the $Q - V$ droop intrinsic feature of reactive power-sharing considering different bus voltages.

Table 6.3 Active and Reactive Power Share and Microgrid Frequency

DG	Active Power (p.u.)	Reactive Power (p.u.)
1	0.35625	0.176102
2	0.35625	0.136894
3	0.35625	0.423200
	ω = 0.999112 p.u.	

6.4 Generic FR-FBS Algorithm

For large networks, it becomes more challenging to determine the way in which the algorithm should scan the network in order to execute the FR-FBS. Based on the discussion for the 6-bus example provided above, a generic technique was developed to provide solutions for large networks. The technique is based on the exploring the network and dividing it into different categorized sections, which are then used to form specific network matrices. The following three types of network sections are considered:

1. Branch section: Starts at a leaf point and ends at a joint point.
2. Main trunk section: Starts at a joint point and ends at a joint point or at the point directly connected to the reflection point.
3. Pivot branch section: Starts at the pivot point and ends at a joint point.

In addition, system points (nodes) are also categorized into the following four types:

1. Reflection point: Usually the PCC, with only one reflection point selected.
2. Pivot point: Any point connected to a DG, with only one point selected as the pivot.
3. Leaf point: Terminal point of a branch.

$$i \in Leaf \ \ iff \sum_{j=1, j\neq i}^{N} A_{ij} = 1 \ \ \forall j \in N \tag{6.25}$$

4. Joint point: Joins more than one branch and/or trunk section.

$$i \in Joint \ \ iff \sum_{j=1, j\neq i}^{N} A_{ij} > 2 \ \ \forall j \in N \tag{6.26}$$

where A is the network connectivity matrix, and $A_{ij} = 1$ if nodes i and j are interconnected.

After the network sections and the system points (nodes) have been classified, the FR-FBS is executed through the application of the algorithm outlined in the flowchart shown in Figure 6.7. As the flowchart indicates, the flow of the FR-FBS solution is directed through the microgrid described by the previously mentioned network matrices. As explained in Figure 6.8, the algorithm solves forward from the pivot point towards the reflection point through the main trunk. Whenever a joint point is reached, the algorithm solves these branches in forward and backward directions before resuming the forward calculations.

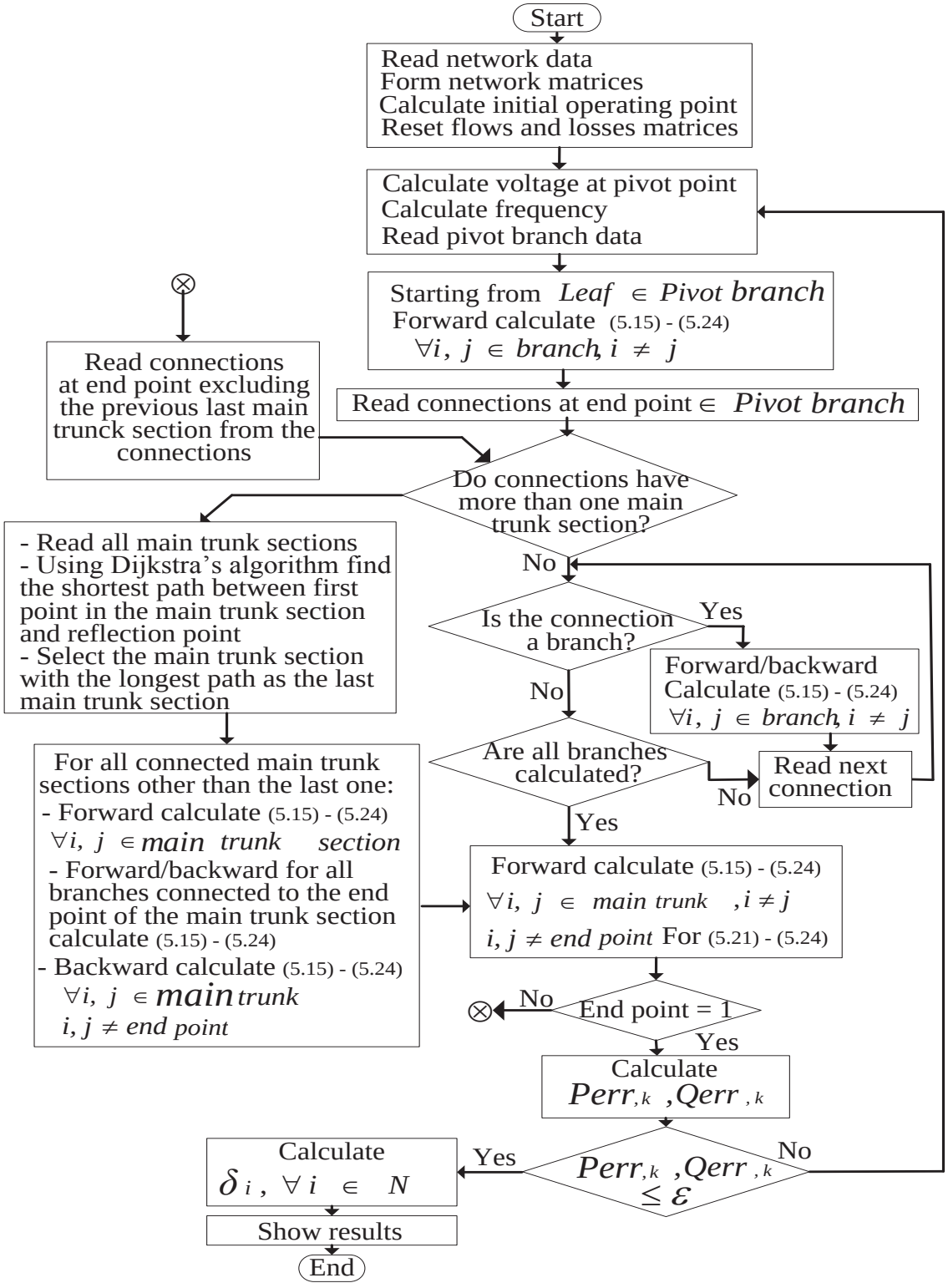

Figure 6.7: Flowchart for generic FR-FBS algorithm.

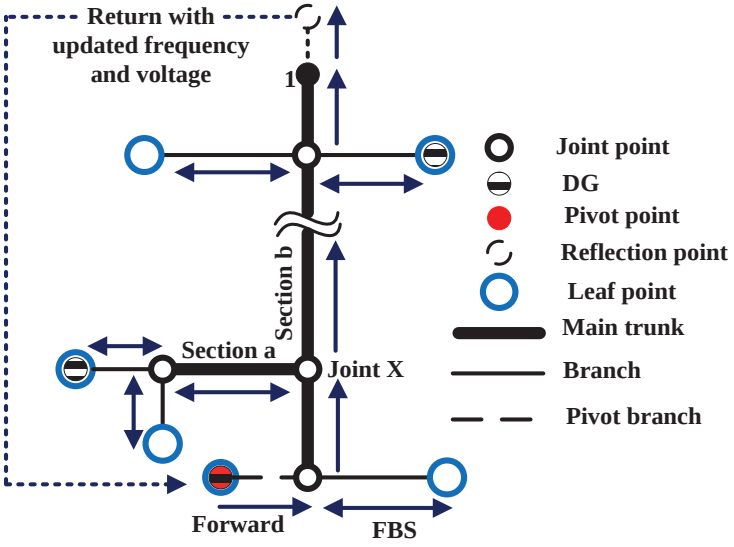

Figure 6.8: Generic representation of categorized network.

If more than one main trunk section is connected to the joint point, as denoted by joint X in Figure 6.8, the algorithm solves the section that has the largest distance to the reflection point first (i.e., section a) before resuming the forward calculation. Dijkstra's shortest-path algorithm [105] was adopted for this flowchart as a means of determining the shortest path between the selected nodes and the reflection point. It is worth mentioning that any other algorithm can be used to find the shortest path. In addition, the shortest path algorithm will be run just once at the categorization stage.

6.5 Case Study for Islanded AC Microgrid

The IEEE 38-bus system [106] shown in Figure 6.9 was used for testing and validating the proposed FR-FBS power flow algorithm for isolated ac microgrids. The system was modified to include additional DGs at the candidate buses [59]. Table 6.4 shows the different ratings and droop characteristics of the DGs installed in the IEEE 38-bus system. As an alternative to the constant impedance load model considered in section 6.3, The voltage- and frequency-dependent load models (6.27)−(6.28) developed in [106] were adopted for use with this system in order to confirm the ability of the proposed algorithm to handle a variety of load models. The load data, $P_o, Q_o, \alpha, K_{pf}, K_{qf}$, and β , were also adopted from [106]. The voltage- and frequency-dependent load models are

$$P_{L,i} = P_{o,i}|V_i|^{\alpha}(1 + K_{pf}\Delta\omega) \quad (6.27)$$

$$Q_{L,i} = Q_{o,i}|V_i|^{\beta}(1 + K_{qf}\Delta\omega) \quad (6.28)$$

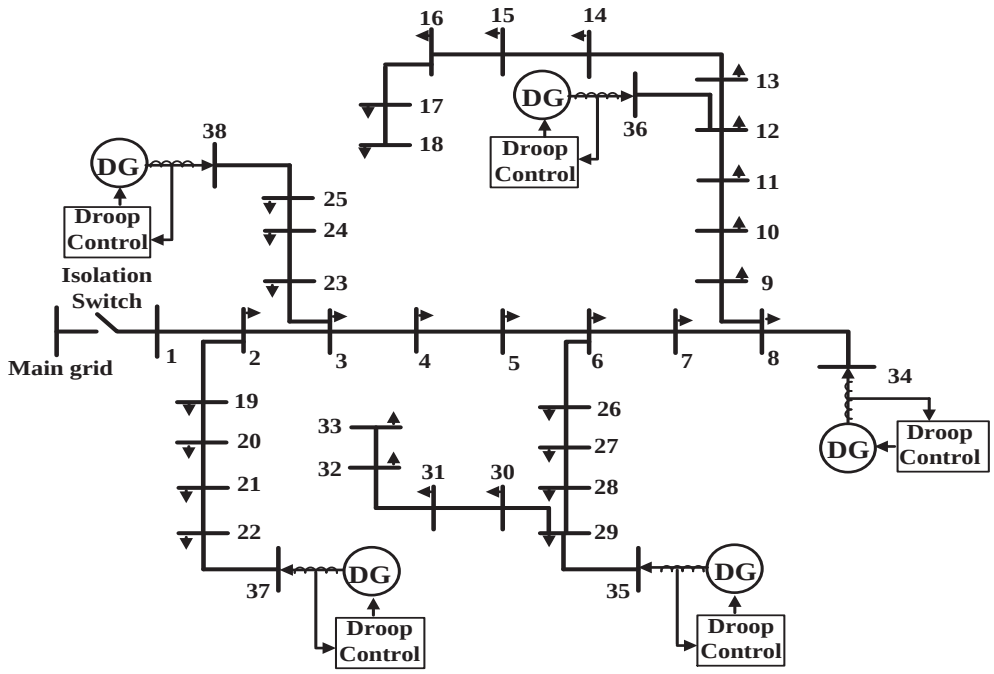

Figure 6.9: A 38-bus system with DGs placed at candidate locations.

Table 6.4 DG Data for 38-bus System

Node	m_p (p.u.)	m_q (p.u.)	ω_{ref} (p.u.)	V_{ref} (p.u.)	S_{max} (p.u.)
34	0.751×10^{-3}	0.01667	1	1.01	3
35	1.501×10^{-3}	0.03333	1	1.01	1.5
36	4.504×10^{-3}	0.01000	1	1.01	0.5
37	2.252×10^{-3}	0.05000	1	1.01	1.0
38	4.504×10^{-3}	0.01000	1	1.01	0.5

The 38-bus system is considered to form an isolated ac microgrid with an open isolation switch connecting it to the main grid, as shown in Figure 6.9. The system sections and the nodes are categorized based on the formation of the network matrices described earlier. Based on the definitions of the section and the node categories, the network matrices are formed as shown in Table 6.5. These sections are represented graphically on the network graph shown in Figure 6.10, with the arrows on the graph indicating the execution sequence of the FR-FBS algorithm outlined in the flowchart provided in Figure 6.7. As mentioned earlier, any node with a DG can be selected as a pivot node. In this case study, node 36 is selected as the pivot point and the connection to the main grid is the reflection point.

Table 6.5 Network Matrices for 38-bus System

Category	Matrix
Main trunk sections	[{1,2},{2,3},{3,4,5,6},{6,26,27,28,29}, {6,7,8},{8,9,10,11,12}]
Branch sections	[{38,25,24,23,3},{18,17,16,15,14,13,12},{33,32,31,30,29}, {35,29},{34,8},{36,12},{37,22,21,20,19,2}]
Pivot branch section	[{38,12]]
Pivot point	[36]
Leaf points	[38,18,33,34,35,36,37]
Joint points	[2,3,6,8,12,29]
DG	[34,35,36,37,38]

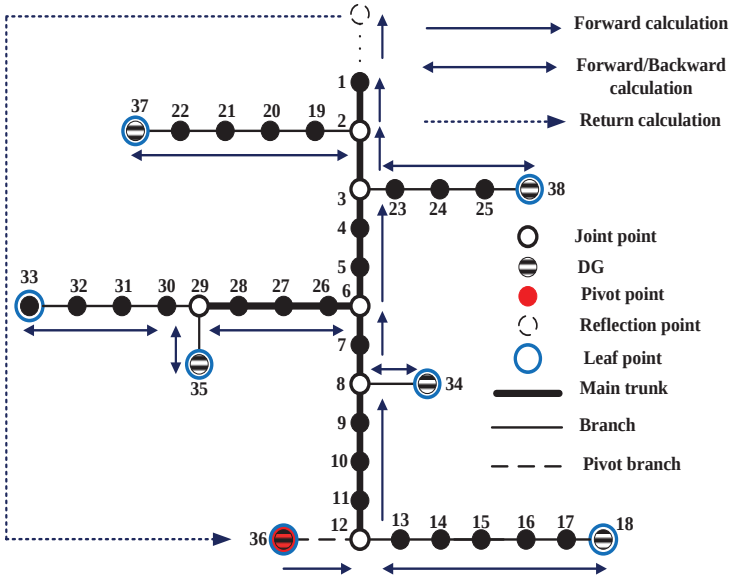

Figure 6.10: A 38-bus system with DGs placed at candidate locations.

The FR-FBS was used to provide a solution for the 38-bus system, and the results are shown in Table 6.6. The bus voltage magnitudes and angles, the load active and reactive power, the DG active and reactive power, and the microgrid frequency were calculated. Line flows, line losses, and the total active and reactive power were also calculated during the execution of the algorithm, which was implemented on the same CPU. The time required for running the complete algorithm was 5.92 msec. The convergence process of the proposed algorithm for solving the 38-bus system is demonstrated in Figure 6.11. The figure shows the convergence process of the coupled variables, indicating that the voltage at the pivot point and the reactive power mismatch are correlated, as described in (6.13).

The change in these variables at different iterations is shown in Figure 6.11.a. Similarly, the frequency of the microgrid and the active power mismatch are correlated, as described in (6.7). Figure 6.11.b shows the change in these variables with different iterations. As described in the flowchart

presented in Figure 6.7, the active and reactive power mismatches are selected as the stopping criteria. These curves prove the efficiency of the proposed methodology in the inter-iteration variables updating strategy, and the linking of the microgrid frequency to the active power mismatch and the pivot voltage to the reactive power mismatch. Thus, the load flow problem of an isolated ac microgrid was solved by using a branch-based technique without a slack bus and by considering the variable frequency resulting from the droop-controlled DGs operation.

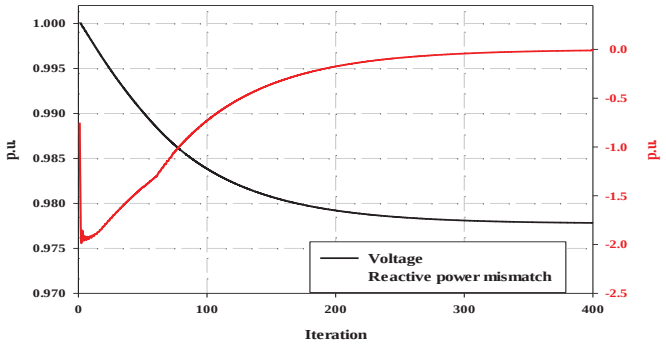

a) Voltage at pivot point and reactive power mismatch at reflection point.

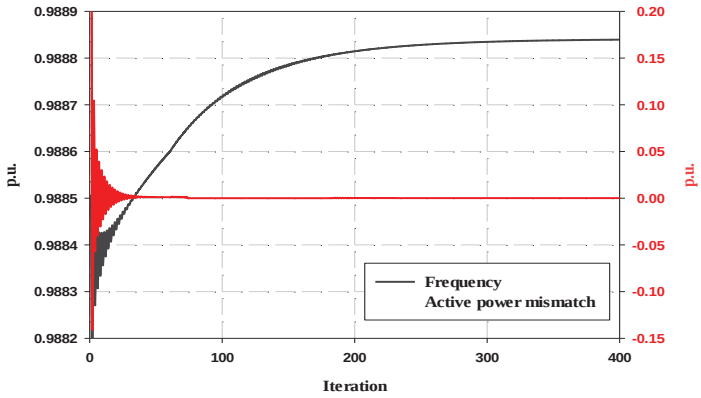

b) Frequency of microgrid and active power mismatch at reflection point.

Figure 6.11: Convergence of the solution variables versus the iteration number for 38-bus system.

The results obtained from the proposed algorithm for bus voltages magnitudes and angles, active and reactive power loading and active and reactive power injected from DGs are presented in Table 6.6. The obtained results are the exact same as those of the NTR, as presented in [59], when it was used and implemented on the same CPU to solve the studied system and it converged in 7.426 seconds (compared to the present method where the solution is obtained in 0.00592 second). It worth mentioning that in many power system on-line applications, load flow problem solutions are executed numerous times, which makes the time-per-solution a crucial aspect of solving this application. An example of an

application that requires many load flow solutions is MCS for a probabilistic load flow, which needs approximately 10,000 solution points [78][74] to converge. For such an application, the proposed algorithm will require less than one minute to find the probabilistic load flow, while the NTR will need 20.62 hours to complete this load flow study.

The results presented in Table 6.6 can be interpreted to understand the microgrid operation. For example, DG 3 and DG5 have the same active and reactive droop parameters, i.e., they have the same rating. This can be seen from the results, as they inject the same active power to their buses. However, they have unequal reactive power share, with DG 5 injecting almost 50% more reactive power compared to DG 3, despite being equally rated. This problem was explained in the voltage calculation part of the problem description section. Based on (6.4) and (6.10), active power share is proportional to the droop parameter only because all DGs are operating at the same frequency, whereas reactive power share is dependent on both the droop parameter and the bus voltage.

In addition, the support of DGs to the bus voltage can be noted from the bus voltage magnitude presented in Table 6.6. The proposed algorithm has enabled the branch-based technique to solve the load flow problem without assuming a slack bus or approximating the DG reactive power to be proportional to droop parameters only. These assumptions were the main drawback of the conventional methods. The loading percentage of the microgrid was changed and the voltage profile at all buses was examined. This study can be used as an investigation tool for the microgrid load-ability limits. Figure 6.12 presents the voltage profiles for three loading condition levels: normal loading (λ =100%), light loading (λ = 50%), and heavy loading (λ = 120%). The results show that buses with DGs experience higher voltage, which can lead to over-voltage during light loading conditions. In addition, during heavy loading, the load buses experience voltage dips, which can be improved by readjusting the DG droop parameters.

Figure 6.13 presents generation-sharing between micrgrid DGs at different loading conditions. As shown in the results, DG1 is the most loaded DG. This was expected according to the DG parameters presented in Table 6.4. The DG with the least active power droop slope will be the one which is most loaded. Figure 6.13.b shows DGs' contribution to the total power supply of the microgrid at the different percentage loading conditions. The contribution ratios are constant and depend on the droop parameters. These can be calculated based on (6.5), as follows:

$$\text{Contribution of } DG_i = \frac{\frac{1}{m_{p,i}}}{m_{p,eq}} \tag{6.29}$$

Table 6.6 Power Flow Results for 38-Bus System Using FR-FBS

Bus No.	Voltage (p.u., degree)		Load (p.u.)		Generation (p.u.)	
	Mag.	Ang.	P_{Load}	Q_{Load}	P_G	Q_G
1	0.95642	0.0000	0	0	—	—
2	0.95642	0.0000	0.095619	0.052363	—	—
3	0.95635	-0.0197	0.088398	0.03236	—	—
4	0.95757	-0.0014	0.112389	0.071591	—	—
5	0.9662	0.0159	0.057481	0.026402	—	—
6	0.9696	0.1365	0.058999	0.016804	—	—
7	0.9712	0.3165	0.189223	0.091556	—	—
8	0.9764	0.2868	0.190755	0.093233	—	—
9	0.9738	0.1690	0.059045	0.017246	—	—
10	0.9716	0.0607	0.056802	0.018337	—	—
11	0.9712	0.0493	0.042575	0.027467	—	—
12	0.9707	0.0258	0.057727	0.031385	—	—
13	0.9651	-0.0697	0.046858	0.031365	—	—
14	0.9629	-0.1441	0.1146	0.069438	—	—
15	0.9615	-0.1808	0.055913	0.008848	—	—
16	0.9601	-0.2058	0.058895	0.01584	—	—
17	0.9578	-0.2792	0.055588	0.017466	—	—
18	0.9571	-0.2905	0.098103	0.069956	—	—
19	0.9648	-0.0166	0.086106	0.034996	—	—
20	0.9704	-0.1484	0.085045	0.03652	—	—
21	0.9725	-0.1617	0.088546	0.034216	—	—
22	0.977	-0.1458	0.106464	0.082843	—	—
23	0.9619	-0.0756	0.083922	0.044305	—	—
24	0.9592	-0.2012	0.389978	0.175533	—	—
25	0.9596	-0.2778	0.390224	0.175782	—	—
26	0.9694	0.1410	0.056608	0.022745	—	—
27	0.9692	0.1480	0.058995	0.020954	—	—
28	0.9683	0.1854	0.056511	0.018126	—	—
29	0.9681	0.2235	0.112987	0.063396	—	—
30	0.965	0.3009	0.187402	0.537503	—	—
31	0.9613	0.2138	0.143031	0.060351	—	—
32	0.9605	0.1909	0.20009	0.085926	—	—
33	0.9603	0.1839	0.055808	0.035244	—	—
34	**1.002**	1.1047	0	0	1.6739	0.4051
35	**0.9862**	0.2899	0	0	0.8369	0.6067
36	**0.9777**	0.0105	0	0	**0.279**	**0.2737**
37	**0.9803**	-0.1534	0	0	0.558	0.5039
38	**0.9618**	-0.2818	0	0	**0.279**	**0.4091**

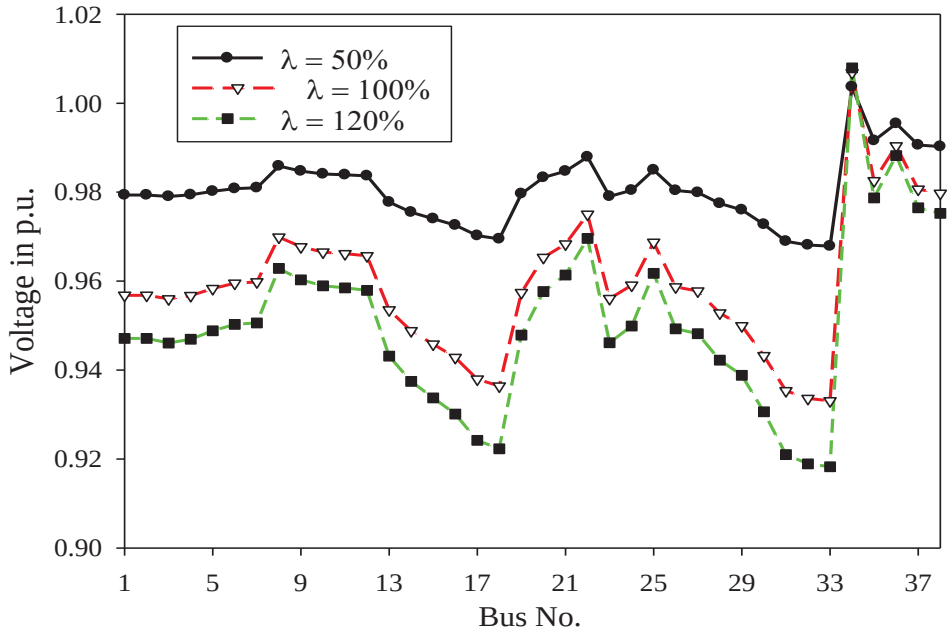

Figure 6.12: Voltage profiles at different loading conditions (λ).

According to Table 6.4 for DG 1, the contribution factor =0.46 coincides with the results obtained in Figure 6.13.b.

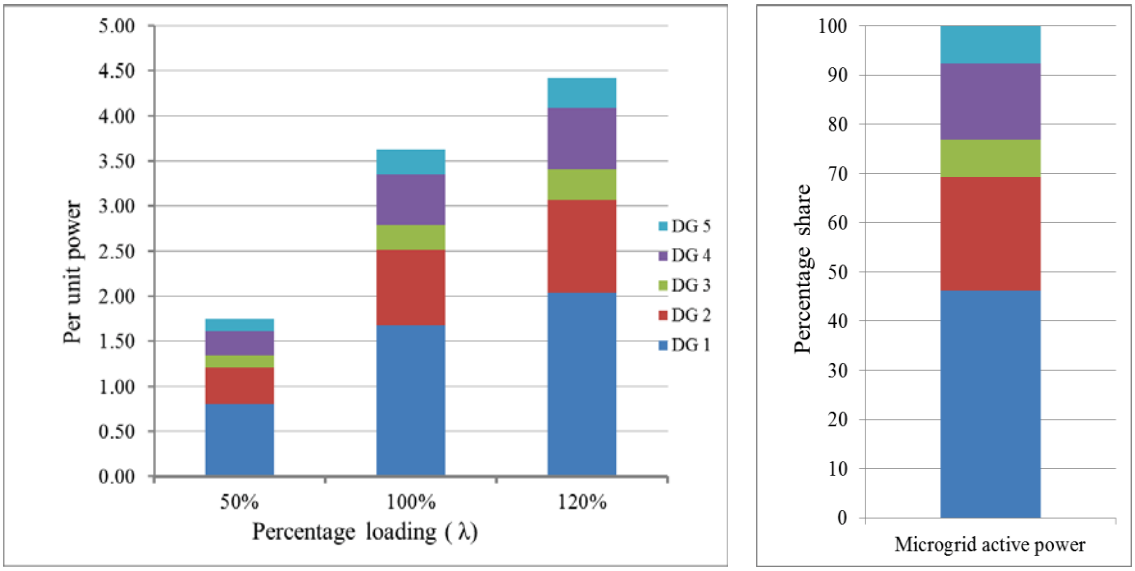

(a) Output power from DGs at different percentage loading

(b) DG percentage contributions

Figure 6.13: DG loadings at different percentage loading conditions.

6.6 The FR-FBS Algorithm for Hybrid Microgrids

The recent penetration of DGs into the existing electricity grids and the consequent development of active distribution networks (ADNs) have prompted an exploration of power distribution in a dc microgrid paradigm. Compared to traditional ac networks, dc microgrids offer numerous advantages, including:

1) Higher system efficiency due to a reduced number of conversion stages required for connecting electronic and nonlinear loads.

2) Cost-effective accommodation of energy storage and dc-based DG units, such as solar PV, type-4 wind turbines, and fuel cells.

3) Efficient and compatible platform for dc loads, such as dc LED lights and PEVs.

4) Less interference with ac grids because of the absence of synchronization problems.

5) Flexible energy paradigm for future expansion [107].

A number of dc networks have already been established as expansions of conventional ac distribution systems [108], and a new hybrid configuration of ac and dc microgrids is now a paradigm whose realization is very viable in the near future [109]. The planning framework for these hybrid microgrids was discussed in Chapter 5. Installation of distributed generators (DGs) within hybrid distribution systems could provide highly reliable service based on their ability to maintain the load supply to different ac and dc microgrids, even in the case of interruptions at the main substation. In an islanded mode of operation, reliability would be reinforced by the implementation of droop characteristics to coordinate the DG output power in a decentralized manner [47]. The layout of a hybrid microgrid is shown in Figure 6.14 with an IC used for connecting both ac and dc microgrids.

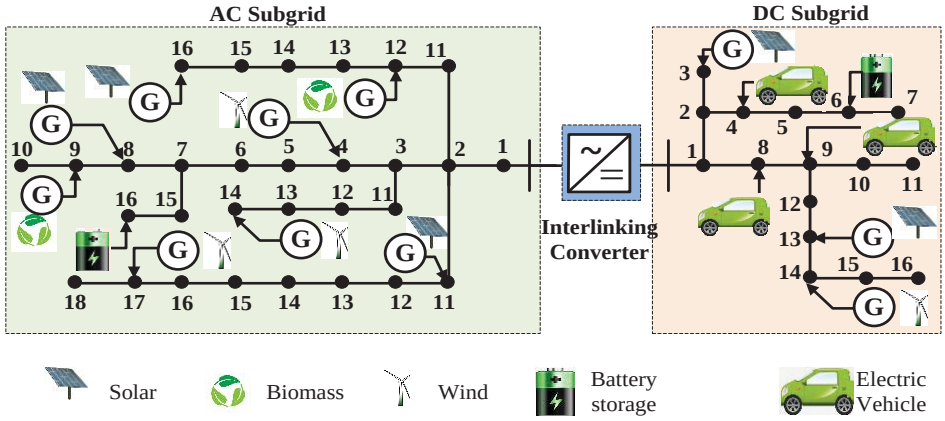

Figure 6.14: Layout of hybrid microgrids.

As discussed earlier, DGs in an ac microgrid employ the appropriate system frequency and voltage that will enable the respective active and reactive power of the microgrid to be shared. In a similar manner, the DGs adapt the system voltage in order to share the load power in a dc microgrid. At the same time, the IC between the ac and dc microgrids works to equalize the loading levels of the ac and dc microgrids by relating the ac frequency to the dc voltage [58], [110], [111]. The coupling between the ac frequency and the dc voltage is a feature unique to hybrid microgrids. This feature allows ac and dc microgrids to share the overall loading without the presence of a slack bus in either microgrid. The operational scheme incurs variations in system frequency and voltage level with the change of system loading. However, the implementation of a non-critical secondary control (with a minimum communication requirement) will be sufficient to maintain this sharing of power between DGs, since load and generation are always balanced by the primary control. The secondary control maintains the system frequency and voltage very close to the nominal values and can also achieve additional operational objectives as stated in [14].

The practical implementation of this operational philosophy in large-scale hybrid microgrids is established on a profound understanding of the system behavior learned from comprehensive steady-state analysis for a variety of loading and generation levels. To this end, an accurate and reliable load flow algorithm is essential for the performance of a number of planning and operational studies. These studies include but are not limited to an examination of DG allocation and sizing, VAr planning and control, optimum power management, and protection design and contingency analysis [14], [112], [113]. Although several load-flow algorithms have been proposed for MTDCs, which are hybrid ac/dc systems at the transmission level, these formulations are unsuitable for microgrids. Frequency variations, coupling between the ac and dc variables and lack of a slack bus are key features that characterize islanded ac/dc microgrids and distinguish them from MTDCs. For distribution systems, load flow is formulated and solved through either derivative-based algorithms (Newton's method) or derivative-free algorithms (branch-based methods). For example, the Newton-Raphson approaches have been adopted for solving both ac and hybrid ac/dc microgrids. On the other hand, derivative-free methods offer more reliable and superior performance for distribution systems due to several intrinsic features, such as a high number of nodes, radial topology, and high (R/X) ratio of feeders [59], [114]. However, because these factors contribute to the ill-conditioned behavior of large distribution systems, they may hinder the convergence of some conventional derivative-based algorithms. In contrast, forward-backward methods described in previous sections for ac microgrids guarantee a robust convergence behavior for radial distribution networks and offer advantages for solving large-scale

networks, such as simplicity in implementation, system-independent convergence time, and low computational and memory requirements [115].

This section introduces a novel branch-based load flow algorithm developed for performing steady-state analysis in hybrid ac/dc microgrids. In this algorithm, the traditional branch-based load flow approach has been adapted to accommodate the unique features and challenges of islanded hybrid microgrids, such as: variable frequency, droop-controlled DGs, interaction between ac and dc microgrids, and the lack of a slack bus. Unlike the Newton-based methods applied in [55], [65], the proposed algorithm has inherited the intrinsic features of branch-based techniques so that it is inversion- and derivative-free. The algorithm starts by decomposing the load flow problem for the hybrid system into two interlinked smaller sub-problems for the ac and dc microgrids, and then solves them sequentially. This approach reduces problem complexity and thus offers enhanced performance speed without compromising solution efficiency.

For the decomposition process, the coupling between the ac frequency and the dc voltage is still maintained through the modelling of the dc microgrid as a constant-power DG at the PCC on the ac side. A novel branch-based load flow algorithm, named the forward-return-forward-backward sweep (FR-FBS), as presented in the previous sections, has been proposed in this thesis for solving the ac microgrid. The proposed algorithm alternates between FB and backward forward (BF) to allow for inter-iteration updating of the solution variables and thus improves the convergence. In addition, the ac load flow is based on power sweeps rather than current sweeps. The effect of the ac microgrid is modelled and reflected on the dc side as a reference bus whose voltage is a function of the ac microgrid frequency.

A backward-forward sweep (BFS) algorithm has been developed for solving the islanded dc microgrid and determining the power interchange between the dc and ac microgrid. Similar to the algorithm proposed for ac microgrid, this BFS is a directed load flow solution that starts with an exploration and categorization of the microgrid nodes and branches in order to set the direction of the solution. The two algorithms are integrated to form the hybrid load flow tool for use with islanded hybrid microgrids. This subsection introduces a novel representation of the dc microgrid and its effect on the ac-microgrid's frequency. The dc microgrid representation is used for the inter-iteration ac microgrid's frequency update. In addition, a quadratic equation for the modelling of dc droop-regulated DGs is developed for solving the BFS load flow in dc microgrids.

6.6.1 Hybrid Power Flow Description and Solution Hierarchy

In general, a hybrid microgrid consists of islanded ac and dc microgrids connected by an IC, as illustrated in Figure 6.14. To fulfill load demand in each microgrid, the main strategy of DG control is to implement droop characteristics. In ac microgrids, DG units meet the active and reactive power load requirements through the implementation of P/ω and Q/V droop characteristics. In dc microgrids, P/V droop characteristics are implemented to meet the active power demand. At the same time, the IC between the microgrids is responsible for sharing the overall load demand of the hybrid paradigm, regardless of the location of the load. The ICs achieve this objective by transferring active power from lightly loaded microgrids to heavily loaded ones. It is important to note that the loading condition of a microgrid is inferred through a different variable for each microgrid: the frequency in the ac microgrid and the voltage in the dc one. An IC must therefore map these variables into a common normalized range in order to quantify the loading conditions of both the ac and dc microgrids:

$$\omega_{pu} = \frac{\omega - 0.5(\omega_{max} + \omega_{min})}{0.5(\omega_{max} - \omega_{min})} \tag{6.30}$$

$$V_{pu} = \frac{V_{dc,i} - 0.5(V_{dc,max} + V_{dc,min})}{0.5(V_{dc,max} - V_{dc,min})} \tag{6.31}$$

where ω_{max} and ω_{min} are the respective maximum and minimum values for the permissible frequency of the ac microgrid, and $V_{dc,max}$ and $V_{dc,min}$ are the respective maximum and minimum allowable voltages in the dc microgrid. In this formulation, the loading condition has been normalized between -1 and 1 for both the ac and dc microgrids; however, other normalizing ranges could be applied according to operator preference. An IC could thus transfer an appropriate amount of active power to equalize the normalized values [5]:

$$\omega_{pu} = V_{pu} \tag{6.32}$$

Equation (6.32) represents the coupling between the ac and dc microgrids. Equation 6.32 also indicates that the ac and dc load flows are likewise coupled. In other words, the solution cannot be applied to each microgrid individually, due to the mutual coupling between the two microgrids. However, branch-based load flow algorithms can be developed for solving each microgrid independently while the other microgrid is modelled according to this criterion. The forward-backward sweep (FBS) for solving hybrid ac/dc systems is thus formulated as the integration of the FR-FBS load flow developed for the ac microgrid and the BFS load flow created for the dc microgrid, as indicated in Figure 6.16. The dc microgrid is represented as an ac DG unit at the ac microgrid with a constant power $P_{interchange}$ and a $Q - V$ droop [5]. On the other hand, the dc microgrid has a reference bus

with a constant voltage V calculated from the ac microgrid frequency ω according to the operation of the IC expressed in (1) to (3) [58]. Based on the initial value of ω in the ac microgrid, the value of V for the dc microgrid can be calculated and the load flow in the dc microgrid can be solved to find $P_{interchange}$. The load flow in the ac microgrid can then be computed. Depending on the change in the ac frequency ($\Delta\omega$) the active power mismatch ΔP can be calculated and the frequency updated accordingly. This sequence is repeated until convergence is achieved. The load flows in the ac and dc microgrids are formulated as branch-based load flows. The ac algorithm is already explained earlier in this chapter, while the dc algorithm is described in detail in the following sections. The integration of the ac and the dc algorithms forms the hybrid load flow algorithm.

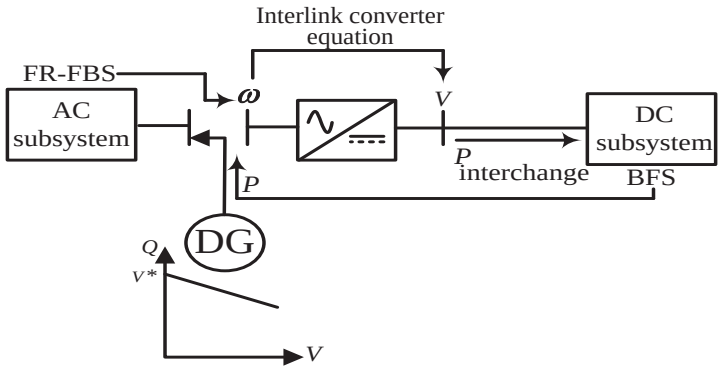

Figure 6.15: Solution hierarchy of hybrid system.

6.6.2 BFS for DC Microgrid

The dc microgrid is described using terms similar to those previously used for the ac microgrid. The system nodes will then be designated either joint, load or leaf points, and the lines are categorized as main trunk or branches, as shown in Figure 6.16. The system is solved through BFS iterations. In the backward sweep calculations, load flows are calculated toward the main trunk starting from all leaf points, and the main trunk is then solved toward the interconnection point.

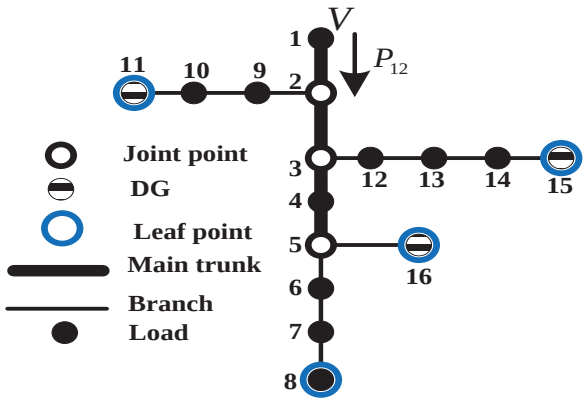

Figure 6.16: DC microgrid illustrating categorization concept.

For the two buses shown in Figure 6.18, during the backward sweep, $P_{i+1,i+2}$ and V_{i+1} are known while $P_{loss\ i+1,i}$ and $P_{i,i+1}$ are calculated using (6.33) to (6.35).

$$P_{injected,i+1} = P_{i+1,i+2} + P_{Load,i+1} - P_{gDC,i+1} \tag{6.33}$$

$$P_{loss\ i+1,i} = R_{i,i+1*}\left(\frac{P_{injected,i+1}}{V_{i+1}}\right)^2 \tag{6.34}$$

$$P_{i,i+1} = P_{injected,i+1} + P_{loss\ i+1,i} \tag{6.35}$$

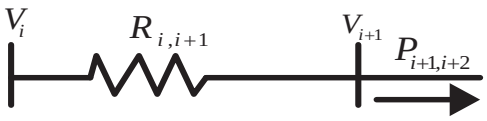

Figure 6.17: Simple two-bus dc system.

The forward sweep calculations then start from the interconnection point, which has a constant voltage V, and the voltages at all system points are computed. In the forward sweep, $P_{i,i+1}$ and V_i are known, and V_{i+1} is calculated using (6.36) and (6.37).

$$V_{Drop\ i,i+1} = R_{i,i+1*}\left(\frac{P_{i,i+1}}{V_i}\right) \tag{6.36}$$

$$V_{i+1} = V_i - V_{Drop\ i,i+1} \tag{6.37}$$

For points connected to leaf points that have droop-controlled DGs, the FBS equations can be modified to account for the DG droop control. For example, in the system shown in Fig. 8, the power balance equation at the DG bus can be written as follows:

$$P_{12} = V_1\left(\frac{V_1 - V_2}{R_{12}}\right) = \frac{V^* - V_1}{m_V} \tag{6.38}$$

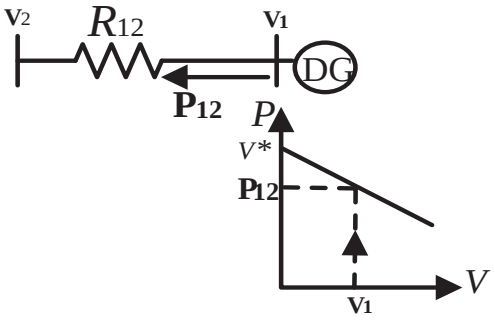

Figure 6.18: DC microgrid illustrating the categorization concept.

This power balance equation can then be rearranged to calculate the DG bus voltage V_1 as a function of V_2 (voltage at the preceding bus) and the DG droop parameters, as follows:

$$\frac{1}{R_{12}}V_1^2 + \left(\frac{1}{m_V} - \frac{V_2}{R_{12}}\right)V_1 = \frac{V^*}{m_V} \tag{6.39}$$

Equation (6.39) is used for the forward sweep voltage calculation, with V_2 known and V_1 unknown, and (6.38) is used in the backward sweep load flow calculation. The FBSs are repeated for the dc microgrid until convergence is achieved. At this converged point, the power fed to the dc microgrid (P_{12}) and the voltage at all dc buses are calculated.

6.6.3 Hybrid AC/DC Microgrids

The FBS for solving hybrid ac/dc systems is formulated through the integration of the FR-FBS load flow of the ac microgrid with the FBS load flow of the dc microgrid, as depicted in Figure 6.16. The dc microgrid is represented as an ac DG with constant power $P_{interchange}$ and a $Q - V$ droop. The dc microgrid will have a reference bus with a constant voltage V calculated from the ac microgrid frequency (6.43) [58]. The power balance equations (6.40) to (6.44) for the hybrid system are used for relating the ac microgrid frequency to the active power generated in the ac and dc microgrids. The change in ac frequency $\Delta\omega$ is then related to the active power mismatch ΔP, which is calculated ateach iteration, as indicated in (6.45) and (6.46).

$$P_{g_{AC}} + P_{g_{DC}} = P_{Load} + P_{Loss} = P_T \tag{6.40}$$

$$P_{g_{AC}} = \sum_{N_{ac}} \frac{\omega_i^* - \omega}{m_{p_i}} = \sum_{N_{ac}} \frac{\omega_i^*}{m_{p_i}} - \frac{N_{ac}\,\omega}{\sum_{N_{ac}} m_{p_i}} \tag{6.41}$$

$$P_{g_{DC}} = \sum_{N_{dc}} \frac{V_i^* - V}{m_{V_i}} = \sum_{N_{dc}} \frac{V_i^*}{m_{V_i}} - \frac{N_{dc}\,V}{\sum_{N_{dc}} m_{V_i}} \tag{6.42}$$

$$V = \frac{C_\omega \omega + C}{C_V} \tag{6.43}$$

$$P_{g_{DC}} = \sum_{N_{dc}} \frac{V_i^*}{m_{V_i}} - \frac{N_{dc}\,\frac{C_\omega \omega + C}{C_V}}{\sum_{N_{dc}} m_{V_i}} \tag{6.44}$$

$$\frac{\partial P}{\partial \omega} = -\frac{N_{ac}}{\sum_{N_{ac}} m_{p_i}} - \frac{N_{dc}\,\frac{C_\omega}{C_V}}{\sum_{N_{dc}} m_{V_i}} \tag{6.45}$$

$$\Delta\omega = \frac{\Delta P}{-\frac{N_{ac}}{\sum_{N_{ac}} m_{p_i}} - \frac{N_{dc}\,\frac{C_\omega}{C_V}}{\sum_{N_{dc}} m_{V_i}}} \tag{6.46}$$

Figure 6.20 shows the pseudo code for the hybrid ac/dc load flow algorithm. This pseudo code delineates the integration of the previously discussed FR-FBS for the ac microgrid with the BFS for the dc microgrid.

It is worth mentioning that if multiple ICs are installed in the same hybrid microgrid, they will employ a droop control scheme that allows active power sharing among the ICs. This droop scheme is realized by introducing an intentional error between the normalized voltage and frequency [58]:

$$\mathrm{e_{pu,x}} = \omega_{\mathrm{pu}} - \mathrm{V_{pu,x}} \tag{6.47}$$

where e is an intentional error introduced between the per unit frequency and dc voltage of the microgrids. This error is a variable that stimulates the ICs to share the active power transfer proportionally to their capacities.

Hybrid AC/DC Load Flow Algorithm

1 Neglect active losses and using (6.40) calculate initial guess of ω

3 Calculate dc voltage V using (6.43)

4 Perform BFS in the dc distribution subgrid

5 Calculate $P_{interchange}$

6 Perform FR-FBS in the ac subgrid considering the dc link as a DG with constant P and droop-controlled Q

7 Calculate $P_{mismatch}$ and $Q_{mismatch}$

8 Using (6.46) and $\Delta P = P_{mismatch}$ find $\Delta\omega$ and update ω

9 Using $Q_{mismatch}$ update the pivot voltage

10 GOTO **3** and repeat until convergence

Figure 6.19: Pseudo code of hybrid load flow algorithm.

Thus, the power injected in the ac side will be expressed as:

$$P_{IC,x} = \frac{1}{K_x} e_{pu,x} \tag{6.48}$$

where $P_{IC,x}$ is the active power injected at the ac side, and k_x is an error coefficient inversely proportional to the IC capacity. However, the proportional power sharing is not guaranteed if the ICs are installed at different dc buses, because, unlike the ac frequency, the dc voltage is not a global power flow variable in dc microgrids. Considering the effect of these modifications in modelling the dc-microgrid on the ac microgrid's frequency, (6.45) will be modified as presented in (6.49) to account for the error introduced between ω_{pu} and V_{pu}. Hence, (6.46) will be modified as shown in (6.50).

$$\frac{\partial P_{gDC}}{\partial \omega} = \sum_{x=1}^{N_{IC}} \frac{-(\frac{C_\omega}{C_V}) \sum_{j=1}^{N_{dg,x}} \frac{1}{m_{V,j}}}{1 - \frac{1}{K_x C_V} \sum_{j=1}^{N_{dg,x}} \frac{1}{m_{V,j}}} \tag{6.49}$$

$$\Delta\omega = \frac{\Delta P}{-\frac{N_{ac}}{\sum_{N_{ac}} m_{p_i}} - \sum_{x=1}^{N_{IC}} \frac{-(\frac{C_\omega}{C_V}) \sum_{j=1}^{N_{dg,x}} \frac{1}{m_{V,j}}}{1 - \frac{1}{K_x C_V} \sum_{j=1}^{N_{dg,x}} \frac{1}{m_{V,j}}}} \tag{6.50}$$

6.7 Case Studies for Islanded Hybrid AC/DC Microgrids

This subsection presents several case studies that demonstrate the flexibility of the proposed algorithm. First, the procedure, the application and the convergence of the proposed algorithm are investigated in detail for a small-scale hybrid system. Next, the algorithm is utilized to solve the power flow problem for a large-scale power system that includes multiple dc links. In the latter case study, various operational scenarios are considered as direct practical applications of the algorithm.

6.7.1 Simple 13-Bus Hybrid AC/DC Microgrids

The simple hybrid system presented in Figure 6.21 (a) has been used for illustrating the proposed FBS load flow when applied to hybrid ac/dc systems. As shown in Figure 6.21 (b), the ac and dc microgrids are first categorized according to the criteria explained in section 6.4. Table I lists the categorized ac and dc microgrid points and branches. As indicated in Figure 6.20, we start with the load generation balance and neglect any losses. Based on (6.40) to (6.44), an initial guess for ω is calculated and, using (6.43), the voltage at D2 is computed. This voltage is assumed to be constant and a BFS is applied to solve the dc microgrid in order to calculate the interchange power $P_{interchange}$. The BFS for the dc system begins with the assumption that all points have a voltage V. The BFS then initiates the backward process and calculates the load flow using (6.33) to (6.35).

The process starts from the leaf points to the joint points, followed by the main trunk section, until the constant *V* point (D2) is reached. The forward calculation process then starts with the calculation of the voltage at all points, based on (6.36) to (6.37). These backward/forward sweeps are repeated until convergence is achieved with respect to point voltage and branch flows. The calculation of power injected at the constant *V* point (D2) represents $P_{interchange}$. The dc microgrid is thus represented by a DG at A5 that has constant power and a droop-controlled Q. The FR-FBS is solved for the ac microgrid starting from the pivot point. The FR-FBS algorithm whose code is provided in Fig. 4 directs the solution, as indicated by the arrows in Figure 6.21 (b). At the reflection point (A0), the active and reactive power mismatches $P_{mismatch,k}$and $Q_{mismatch,k}$ are calculated. Equation (6.46) is used for computing a new estimate of the frequency ω, which updates the voltage at the dc microgrid for the next dc-BFS iteration. The reactive power mismatch is also used for updating the pivot point voltage for the next ac-FR-FBS.

The results obtained for this 13-bus hybrid system are presented in Table 6.8. As evidenced by Table 6.8, the ac DGs share the active power equally because they have the same ratings (i.e., the same slopes) and the same frequency. However, due to the unequal voltages at their terminals, they do not share the reactive power equally. In addition, the power injected at A5 represents the power transferred from the dc microgrid to the ac microgrid.

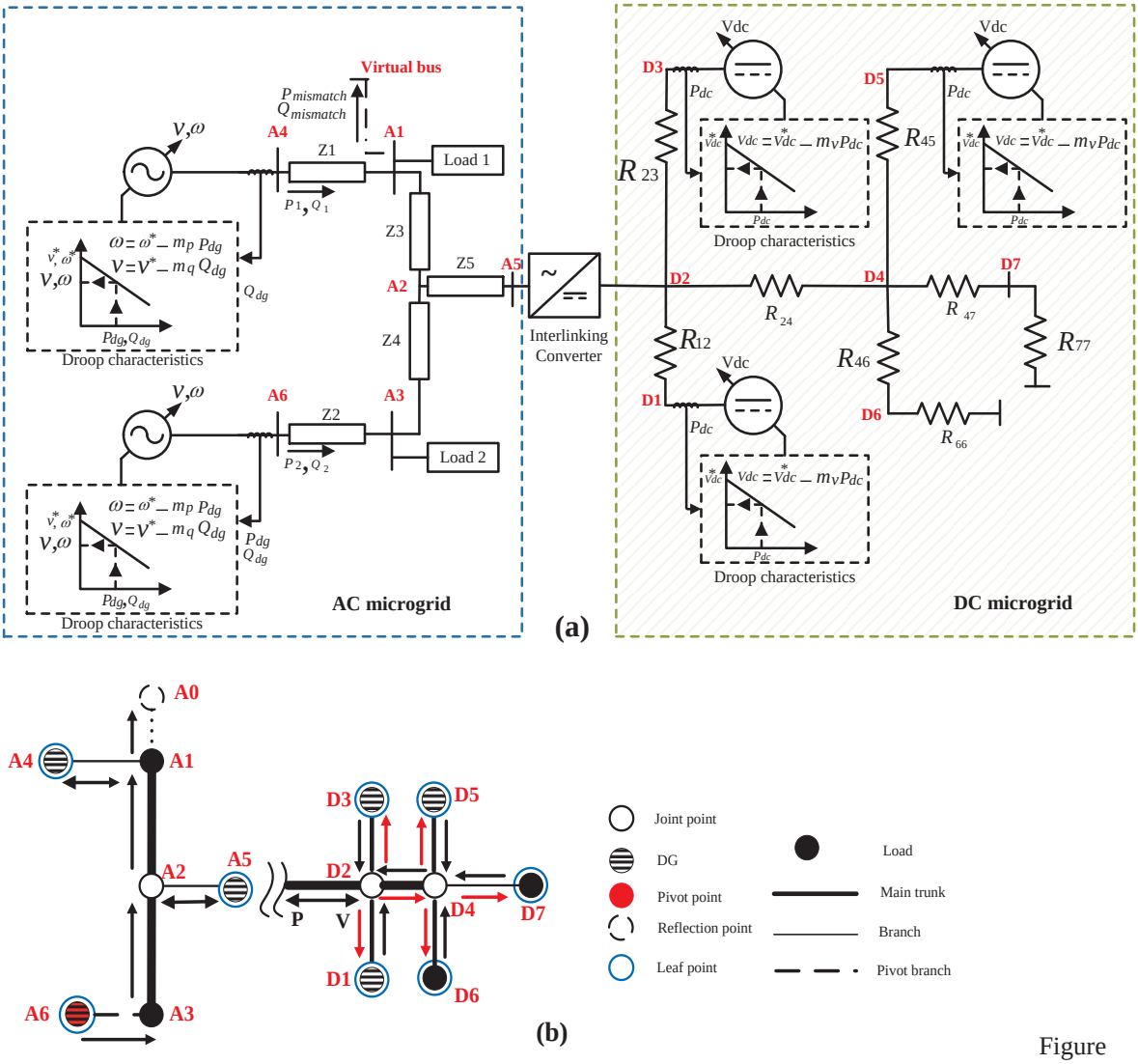

Figure 6.20: Simple 13-bus system: (a) ac and dc microgrid schematics; (b) categorization of the microgrids.

Table 6.7 Categorization of AC and DC Microgrids

	AC Microgrid	DC Microgrid
Leaf Points	A4 and A5	D1, D3, and D5-D7
Joint Points	A2	D2 and D4
Branches	A1A4 and A2A5	D3D2, D5D4, D1D2, D6D4, and D7D4
Main Trunk	A2A3 and A2A1	D2D4
	Pivot point A6 Reflection point A0 Pivot branch: A6A3	Constant V point: D2

Table 6.8 Load Flow Solution for 13-bus System

AC Microgrid					DC Microgrid		
Bus	$\|V\|$	$\angle\delta$	P_{inj}	Q_{inj}	Bus	V	P_{inj}
A1	0.9704	0.0000	0.0000	0.0000	D1	1.0283	0.3173
A2	0.9933	-0.0071	0.0000	0.0000	D2	1.0252	-0.2719
A3	1.0011	-0.0947	0.0000	0.0000	D3	1.0296	0.3039
A4	1.0282	-0.0099	0.2482	0.1628	D4	1.0218	0.0000
A5	1.0260	0.0086	0.2719	0.0000	D5	1.0231	0.3686
A6	1.0130	-0.1033	0.2482	0.3736	D6	1.0204	0.0000
$\omega = 1.0034\ p.u.$					D7	1.0174	0.0000

In order highlight the algorithm's robust performance and convergence, a flat start was assumed as the initial system solution. The voltage magnitudes and angles are, respectively, zeros and ones for the system load buses, and there is no power injection by the droop-controlled DG units. Thus, the DG voltage is V^* (reference voltage) and the ac-subgrid frequency is ω^*. The pivot-point voltage and the reactive power mismatch shown in Figure 6.22 (a) illustrate the convergence of the solution in the pivot-point voltage, while the reactive power mismatch reaches zero. Similarly, Figure 6.22 (b) provides the convergence of the ac-microgrid frequency with the number of iterations as the active power mismatch approaches zero. Using the flat start, all DG voltages start from V^* and all DG power starts from zero, as can be noticed in Figure 6.22 (c) and (d). Moreover, the dc-link starts as a load, with its power calculated from applying the flat start in the dc microgrid. It is worth mentioning that the ac-DG bus voltages (equivalently, the injected reactive power from the DGs) are bounded, i.e., $V_{min} \leq V_{dg} \leq V_{max}$ (equivalently, $Q_{min} \leq Q_{dg} \leq Q_{max}$). This limitation explains the saturation in the first iterations of V4 and V5 in Figure 6.22 (c). A better starting point can be estimated by neglecting losses and using (6.40) to find an initial guess for ω, as mentioned in the pseudo code presented in Figure 6.20. However, in this section's simulation, the conventional flat start was used to prove the robustness of the proposed algorithm.

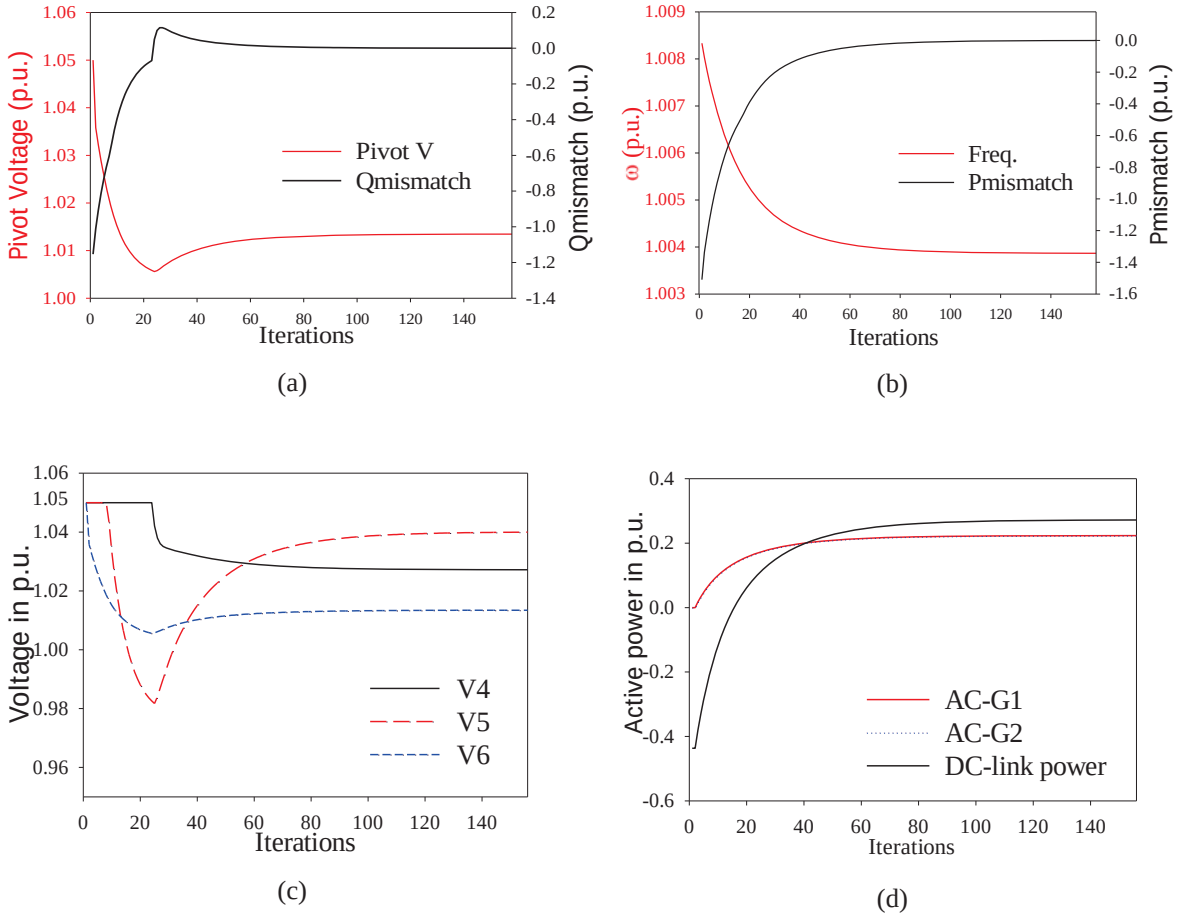

Figure 6.21: Convergence of system variables: (a) pivot point voltage and reactive power mismatch; (b) ac microgrid frequency and active power mismatch; (c) ac-DG bus voltages; (d) ac-DG active power and dc-link power

6.7.2 *Multiple AC and DC Microgrids*

The successful operation of islanded microgrids has been assessed through several operational studies, among which are voltage assessment, the effect of IC outages, and the probabilistic load flow in the presence of renewable DGs. These operational studies are considered the most salient and challenging ones. An extended IEEE 38-bus ac microgrid was augmented with two seven-bus dc microgrids, as illustrated in Figure 6.23 (a), in order to highlight the application of the proposed load flow approach with respect to the performance of these crucial analyses. The categorization of the system nodes and branches is shown in Figure 6.24(b).

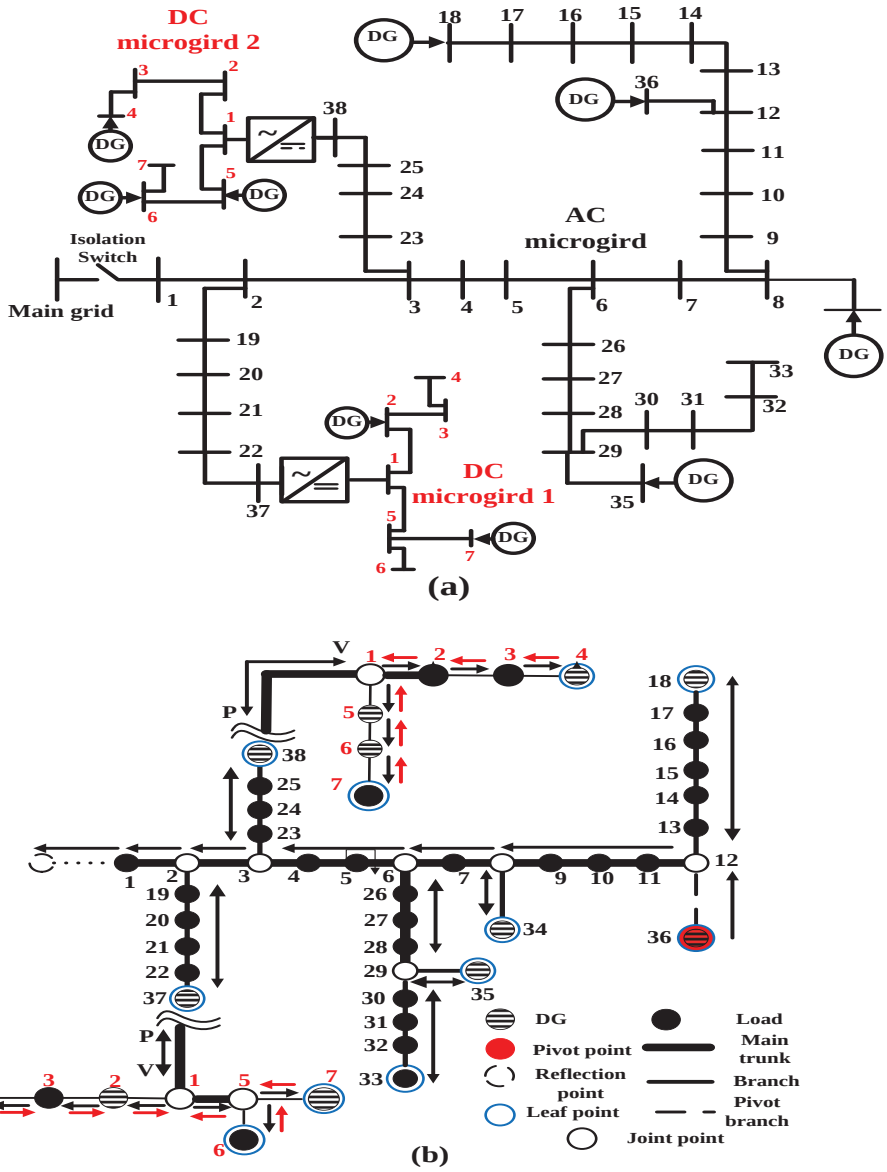

Figure 6.22: Multiple ac and dc microgrid layouts for the case studies: (a) ac and dc microgrid schematics; (b) categorization of the microgrids.

6.7.2.1 Effect of changing load level on ac side

This study is essential for assessing the system voltage profile as well as the power sharing behavior when the system loading level λ is changed. The indicators are used for determining the maximum load-ability of the system or any further readjustment required in the DG droop characteristics in order to avoid overloading. This study addresses system performance with respect to the possibility of changing the value of λ from 70% to 150%. As shown in Figure 6.24, according to conventional droop

settings, the system voltage profile is within the limit for up to 150% of the loading level. Beyond this value of $\boldsymbol{\lambda}$, the system exhibits an under-voltage condition at bus 33. This situation could be handled through further OPF studies similar to those reported in [15], but such studies are beyond the scope of this work. On the other hand, as shown in Figure 6.25, due to the excellent sharing characteristics provided by (6.32), droop settings result in a highly appropriate sharing among all DG units in both the ac and dc microgrids.

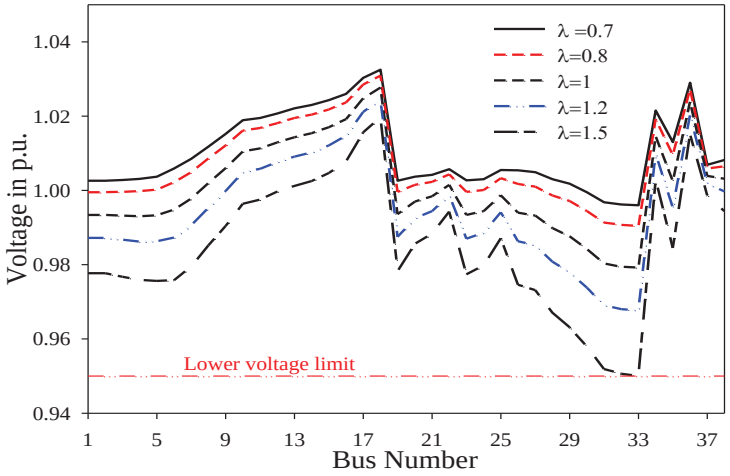

Figure 6.23: Voltage profiles for a variety of ac loading levels ($\boldsymbol{\lambda}$).

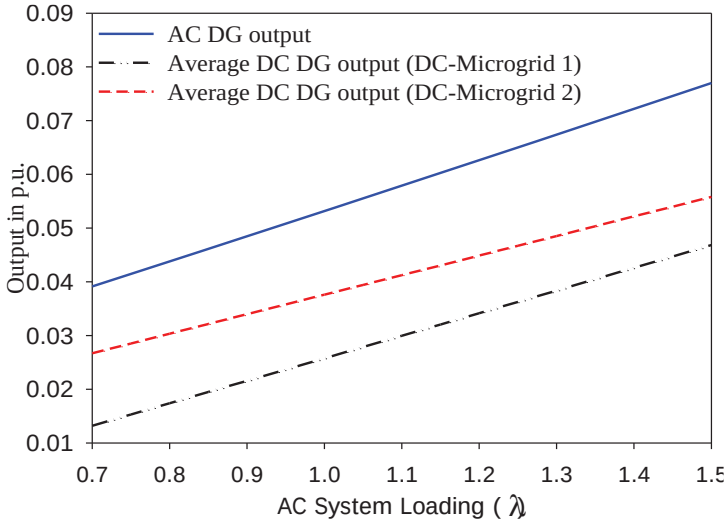

Figure 6.24: Power sharing between ac and dc DGs.

6.7.2.2 Parallel ICs with introduced error

In this case study, the first dc microgrid is assumed to be connected through two parallel identical ICs, and an intentional error is introduced between ω_{pu} and V_{pu}. In this case, both ICs are assumed to have

the same rating, with an equal error coefficient k = 0.1 (i.e. $k_{equivalent}$= 0.05). The pseudo code presented in Figure 6.20 is modified as shown in Figure 6.26 to execute the hybrid load flow algorithm and account for the error introduced into the IC equation (6.47).

1- Knowing ω_{pu} assuming e_{pu}=0

2- $V_{pu} = \omega_{pu} - e_{pu}$

3- BFs in the dc microgrid with V=V_{pu} and calculate P_{total} at convergence

4- Using P_{total} update e_{pu}= $k_{equivalent}$ P_{total}

5- GOTO 2 while $\Delta e_{pu} > \varepsilon$

6- Calculate $P_x = \frac{1}{k_x} e_{pu}$

7- Perform FR-FBS in the ac microgrid considering the dc link as a DG with constant P and droop-controlled Q

8-Calculate $P_{mismatch}$ and $Q_{mismatch}$

9- Using (35) and $\Delta P = P_{mismatch}$ find $\Delta\omega$ and update ω

10- Using $Q_{mismatch}$ update the pivot voltage

11- GOTO **1** and repeat until convergence

Figure 6.25: Pseudo code of hybrid load flow algorithm including the error introduced to all parallel operations of ICs.

Table 6.9 shows the results for both cases (i.e., with no error, and when the error between the normalized voltage and frequency is introduced).

Table 6.9 Results With/Without the Intentional Error in the IC Equation

	Case I (ω_{pu}=0.9949)		Case II(ω_{pu}=0.9948)	
	dc- microgrid 1	dc- microgrid 2	dc- microgrid 1	dc- microgrid 2
$V\ (p.u.)$	0.9827	0.9827	0.9838	0.9824
$e\ (p.u.)$	0	0	-0.0289	0
$P_{interchange}(p.u.)$	0.5979	1.2476	0.5779	1.2551

6.7.2.3 Effect of IC outages

It is important to recall that the main IC objective is to facilitate active power sharing among ac and dc microgrids. In this regard, several operational characteristics have been suggested in the literature. For example, the authors of [15] proposed active power transfer through an IC based on active and reactive power reference values that are updated according to a centralized supervisory control. However, this approach may lead to inappropriate system performance if the supervisory control signal is delayed,

especially in case of an IC outage. This drawback can be addressed through the application of the coupling approach investigated for the current study and expressed in (6.32), since it relies on local information for the updating of the active power transfer, even with a delayed supervisory control signal. Such a claim can be verified by investigating the application of both control schemes for a case study involving an outage of IC #2. To that end, three scenarios have been contrasted in this analysis.

- The first scenario (Case A) involves the two ICs in the system remaining in healthy working order.
- The other two scenarios address system performance after an outage of IC2 during the implementation of different control schemes for IC1 :
  - Case B considers IC 1 controlled through coupling characteristics.
  - Case C considers IC1 controlled through constant PQ characteristics

Figure 6.27 presents the voltage profile for the three cases. As shown, the interlinking mode of operation allowed the dc microgrid to support the ac microgrid voltage after the other dc microgrid disconnected, which helped keep the voltage within allowable limits.

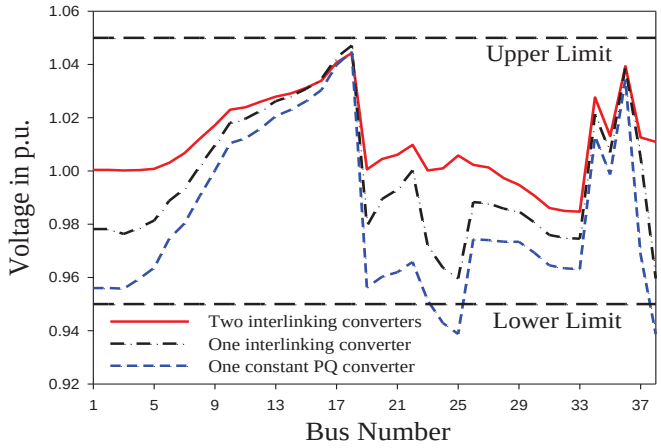

Figure 6.26: Voltage profiles for a variety of dc converter modes of operation.

An additional effect is that, in the interlinking mode of operation, the supplied power from the disconnected dc microgrid was dispatched between the generators in the ac and dc microgrids rather than having the microgrids supplied only from the ac DGs until the central controller modified the converter set points, as would be the case if the dc microgrid converter were working in constant PQ mode. Figure 6.28 shows the average DG power in the ac and dc microgrids for the three cases. In the interlinking mode of operation (Case B), the average power ratio was kept almost the same as in Case A, while in Case C, a large increase in the average DG power was evident in the ac microgrid when

one of the dc microgrids was disconnected. The frequency deviations from 60 Hz for the three different cases are displayed in Table 6.10.

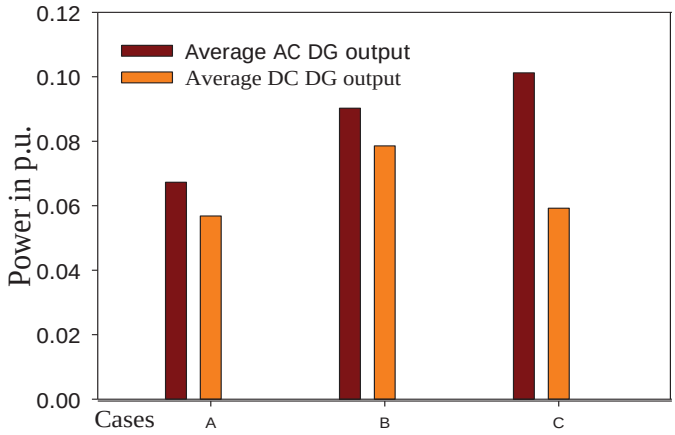

Figure 6.27: Voltage profiles for a variety of dc converter modes of operation.

The results presented in Figures 6.27 and 6.28 reveal the effect of the interlinking mode of operation with respect to supporting the ac system frequency in the case of a load increase due to the disconnection of one of the dc microgrids.

Table 6.10 Frequency Deviations for DC Converter Modes of Operation

	Case A	Case B	Case C
Δf in Hz	0.3060	0.5020	0.7140

6.7.2.4 Probabilistic load flow in the presence of renewable DGs and with consideration of probabilistic load profiles

Renewable-based generators are becoming key components of the supply mix of microgrids. This category of generators is weather-dependent, however, and thus is characterized as having a highly probabilistic nature. A successful tool for evaluating the performance of microgrid operation should be capable of taking such probabilistic behavior into account. To that end, the developed hybrid load flow has been integrated with the probabilistic load and generation model presented in Chapter 3 to form a probabilistic load flow tool for use with hybrid islanded microgrids. To verify the efficacy of this tool, for the system shown in Figure 6.23, two wind-based generators are assumed to be connected at buses 18 and 38 of the ac microgrid. In addition, two solar-based generators are assumed in the dc microgrids: one at bus 2 in the first microgrid, and another at bus 5 of the second dc microgrid. An MCS was employed to determine the probabilistic load flow of the islanded hybrid microgrid. PDFs of the variables obtained are presented in Figure 6.29 and Figure 6.30 for summer and winter, respectively.

The probabilistic loading of the IC during these two seasons is shown in Figure 6.29 (a) and Figure 6.30 (a). During the winter, due to the substantial amount of wind power located in the ac microgrid and the almost-zero solar power during the evenings, power is transferred from the ac to the dc microgrid. In contrast, during sunny and infrequent-wind-gust periods, power is transferred from the dc to the ac microgrid, negatively skewing the power.

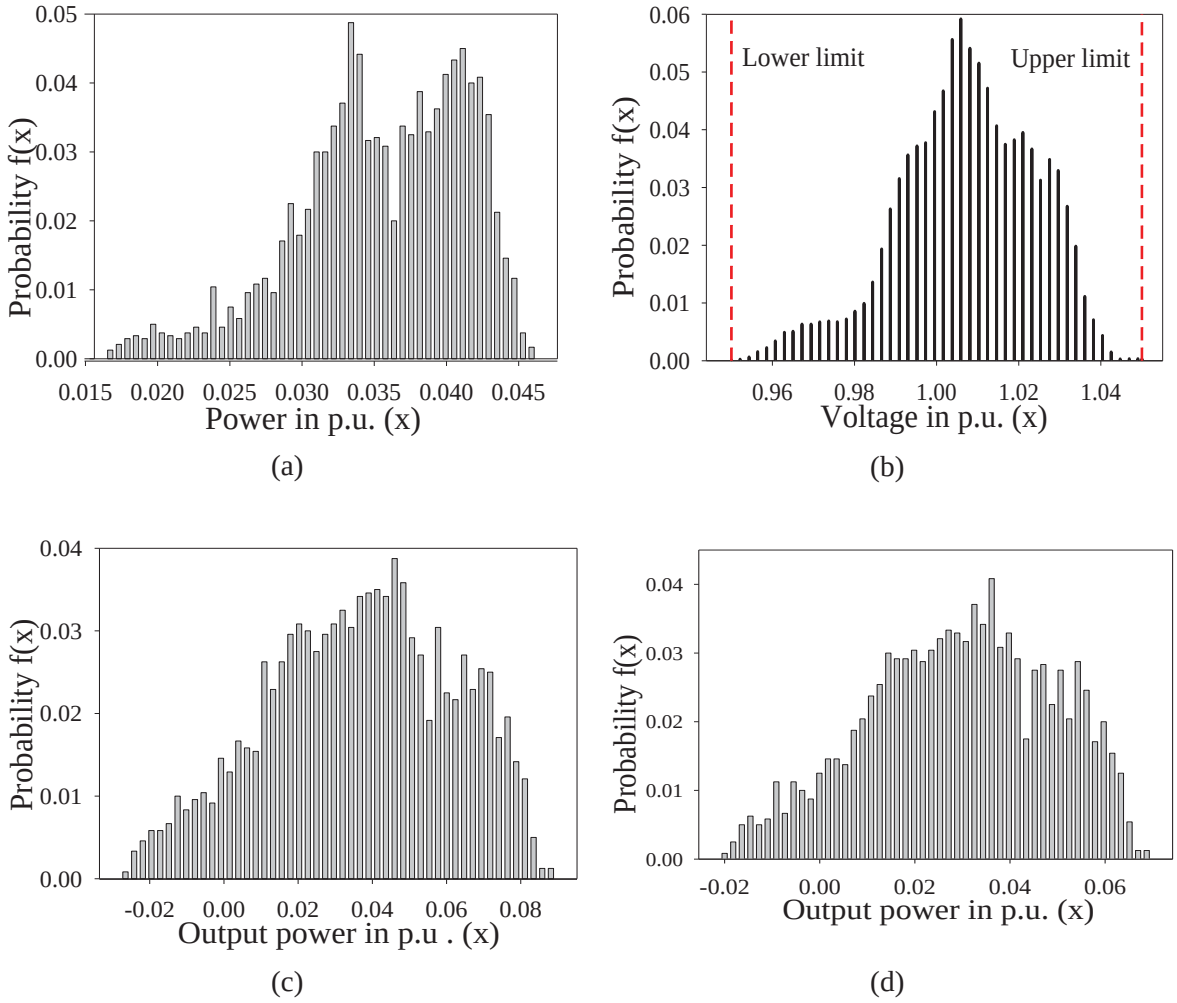

Figure 6.28: PDFs for a variety of variables during summer: (a) power interchange; (b) ac microgrid bus voltages; (c) average ac output power in the ac microgrid; (d) average DG output power in the dc microgrid.

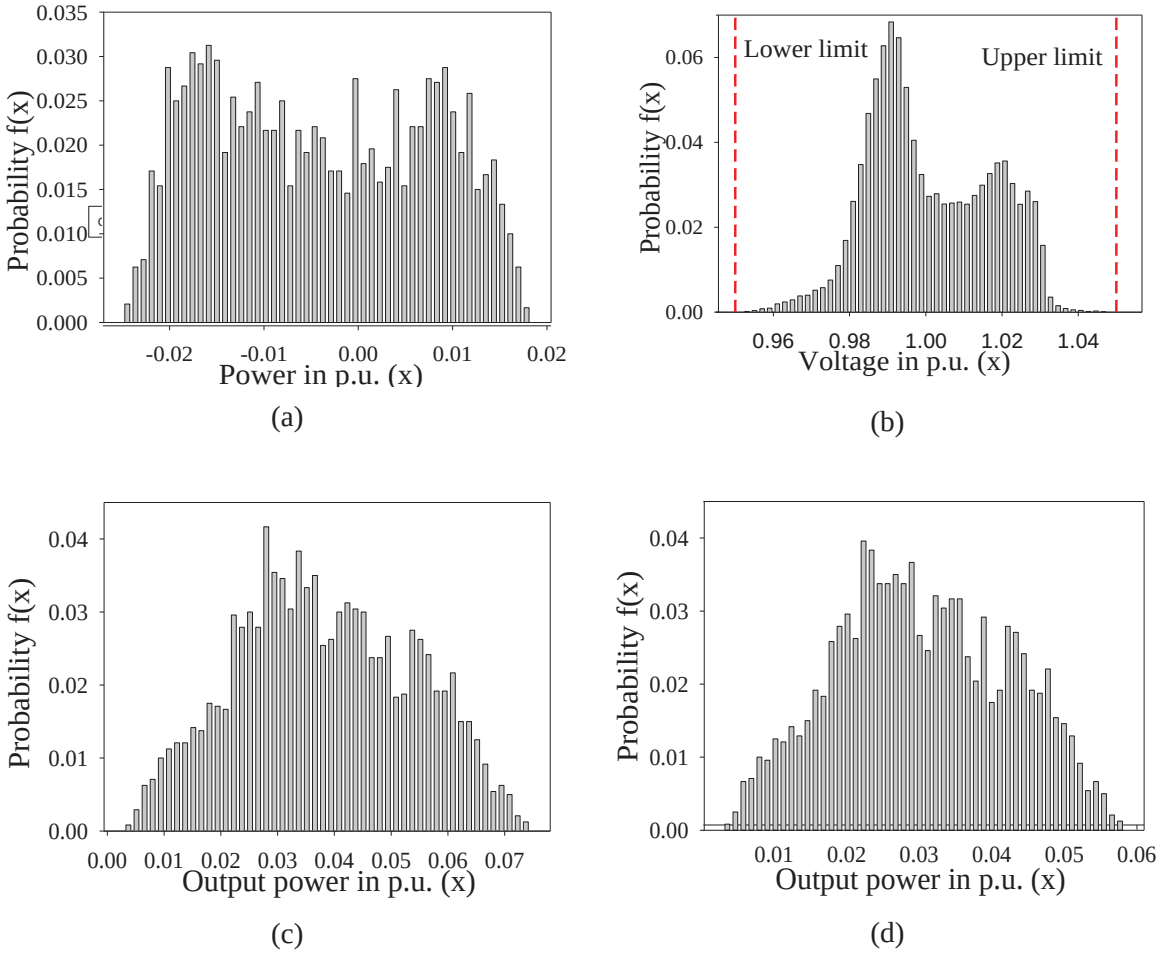

Figure 6.29: PDFs for a variety of variables during winter: (a) power interchange; (b) ac microgrid bus voltages; (c) average DG output power in the ac microgrid; (d) average DG output power in the dc microgrid.

However, the high degree of solar power located in the dc microgrid during the summer keeps the power transfer flowing from the dc to the ac microgrid, creating a positive skew in the power transfer PDF for that season. The probabilistic voltage at the ac microgrid buses is presented in Figure 6.29 (b) and Figure 6.30 (b). The results show that the voltage is kept within allowable limits for the range of variations in renewable generation and load power, which demonstrates the effectiveness of the proposed tool for the probabilistic study of isolated hybrid microgrids. However, if a violation were to occur, the tool could be used for calculating the power curtailed in order to retain the voltage within permissible limits. The probabilistic average loading of the ac and dc DGs during the two seasons is presented in Figure 6.29 (c), Figure 6.29 (d), Figure 6.30 (c), and Figure 6.30 (d). The DG loading in the ac and dc microgrids is correlated due to the coupled frequency and voltage achieved by the IC.

6.7.3 Merging and Demerging of Microgrids

The proposed branch-based algorithm has the flexibility needed to calculate the load flow for clustered microgrids to achieve the dynamic boundaries proposed. This is based on the absence of centralized formulations as well as the simplicity of the algorithm, making it compatible with the limited computational power of distributed agents. For the system shown in 6.31, there are three clusters (microgrids), with an agent assigned to each cluster, as explained in Chapter 4. Each agent will be responsible for the components under its umbrella as well as the isolation switch. Additionally, each agent will have communicability with the neighbors for data interchange and for the merging/demerging process.

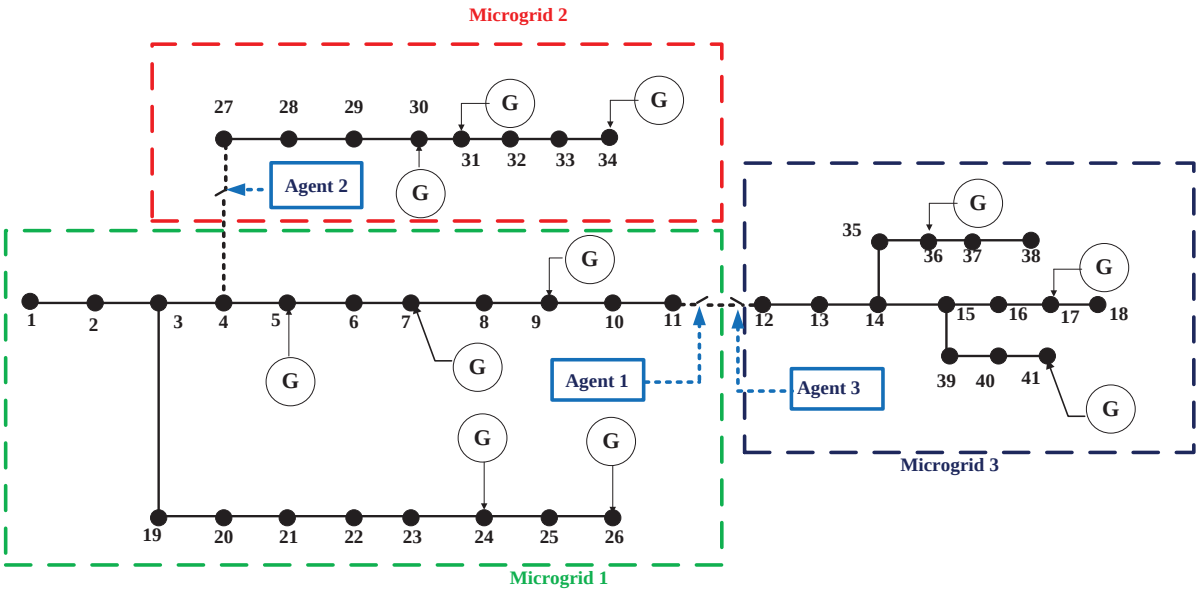

Figure 6.30: Simple 3-clustered microgrids.

Microgrid nodes and lines will be categorized according to the criteria presented in Chapter 4. The different microgrids with their categorized nodes and lines are shown in Figure 6.32. In the islanded mode of operation, where all microgrids are isolated, each microgrid will have a reflection and pivot node as described in Figure 6.32. The proposed FR-FBS algorithm will be implemented in each microgrid's agent with the information of all components, loads and generations in that microgrid. Thus, each agent will be capable of calculating the load flow based on the loading conditions as well as information on the network and DGs. The load flow in the islanded microgrids will be independent and run simultaneously using the FR-FBS. If one of these microgrids is dc, the FBS algorithm proposed earlier in this chapter will be used for the dc microgrid.

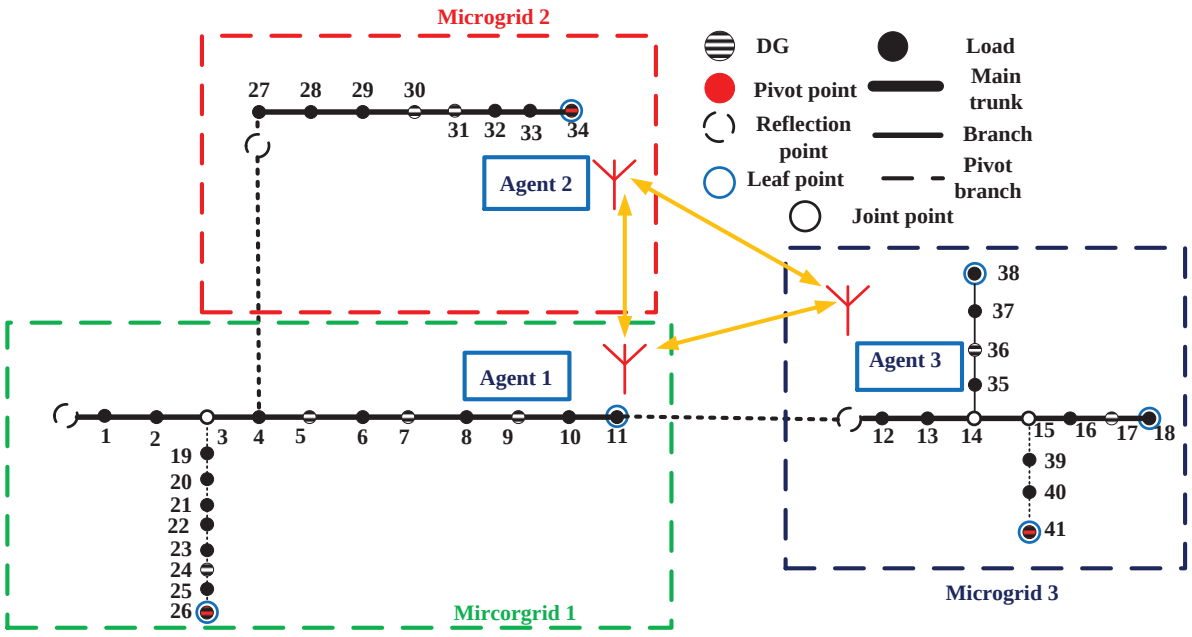

Figure 6.31: Microgrids with categorized nodes and lines.

As described in Figure 6.33, for the case of merging microgrids, the data exchange between the agents will be voltage magnitude, voltage angle, frequency, equivalent droop coefficient for dispatchable DGs, aggregated renewable generation, and aggregated load.

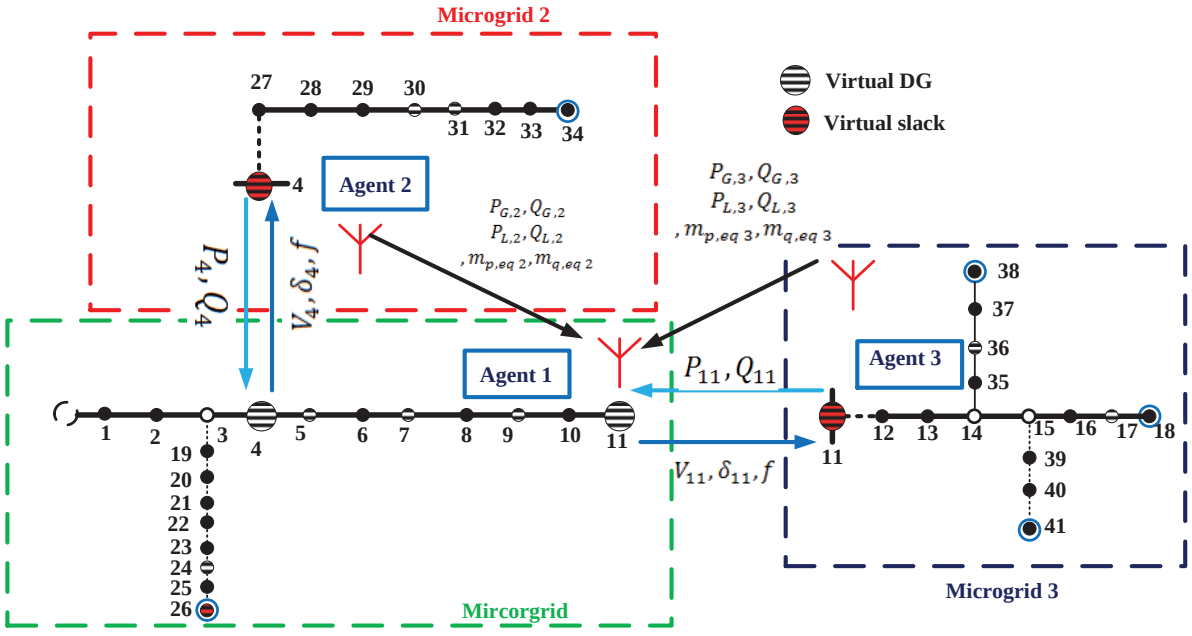

Figure 6.32: Microgrids with exchangeable information during merging mode.

For the system shown in Figure 3.33, Microgrid 1 is considered the main microgrid as it is connected to the main grid. The other two microgrids will be modelled as a virtual DG with constant power, while Microgrid 1 will be modelled as a slack bus for the other two microgrids. The pseudo code for the FR-FBS algorithm for the main microgrid is shown in Figure 6.34.

1- **Input** Network data ($z_{i,j}, A_{i,j}, N$)

2- **Input** DG and microgrids data

($N_{dg}, m_{p,i}, m_{q,i}, Q_{i,max}, V^*, \omega^*, \sum PG_{\mu g,i}, \sum PL_{\mu g,i}, \sum QG_{\mu g,i}, \sum QL_{\mu g,i}, m_{peq,i}$)

3- **Categorize** the network points and lines

4- **Assume flat start**

5- **Set** $Pflow_{i,j,0}$, $Qflow_{i,j,0}$ to zero

6- $k \leftarrow 1$

7- **Calculate** the initial $\omega_{corr,0}$ and ($P_{dg,i,0}, Q_{dg,i,0}, V_{dg,i,0},$) at the pivot point

8- **Send** V, δ, f for emanating microgrids

9- Wait for the receipt of $(P_{\mu g,i}, Q_{\mu g,i})$

10- **Repeat{** // Starting from leaf point ∈ pivot branch

11- **Forward sweep** find load flows in the lines and the voltage magnitude at buses ∈ pivot branch

12- **Read** connections at the end point (the joint point)

// Starting with branches

13- **Forward/backward sweep** find load flows in all lines and the voltage magnitude at all buses ∈ each branch connected to the end point

14- **Forward sweep** using find load flows in the lines and the voltage magnitude at buses ∈ main trunk section

// If more than one main trunk section is connected to an end point, start with the trunk section that has the longest path to the reflection point (determined by the Dijkstra shortest path algorithm) and continue until finishing all sections and reaching the following joint point ∈ main trunk

15**- If** this joint point is not the reflection point **GOTO 9 Otherwise continue**

Calculate $P_{mismatch,k}, Q_{mismatch,k}$ and

$k \leftarrow k + 1$

Update $\omega_{corr,k}$ according to $P_{mismatch,k}$ //$\Delta\omega_k = -\frac{P_{mismatch,k} \sum_{N_{ac}} m_{p_i}}{N_{ac}}$, $\omega_k = \omega^* - \Delta\omega_k$

Update V_{pivot} (Pivot) according to $\alpha\ Q_{mismatch,k}$ //$V_{pivot,k} = {V_{pivot}}^* - m_{q_{pivot}}(Q_{pivot,k-1} - \alpha\ Q_{mismatch,k})$

} Until ($P_{mismatch,k}$ **AND** $Q_{mismatch,k}$) < tolerance

Calculate voltage angle at all buses

Figure 6.33: FR-FBS algorithm for main microgrid.

6.8 Discussion

This chapter presented a novel generalized branch-based power flow algorithm for isolated microgrids. Although branch-based power flow techniques are known for their superiority with respect to distribution networks, they entail serious challenges when applied to isolated microgrids. The main challenges are the necessity of having a slack bus for the forward/backward sweep method and prior knowledge of the system frequency. In isolated microgrids, no slack bus exists, as the sizes of DGs are relatively small and usually controlled through droop to ensure proper sharing of loads to avoid DG overloading. The proposed algorithm eliminates the dependence of branch-based algorithms in the presence of a slack bus for solving the power flow problem and allows the consideration of frequency as a variable related to the DG's droop control characteristics. Thus, it solves the problems associated with the previously proposed branch-based techniques without the need for the approximations or the unrealistic assumptions such as considering the largest DG as a slack bus.

The proposed algorithm novelty lies also in the new categorization of system's lines and nodes in order to directly execute the proposed forward-return algorithm with the embedded forward/backward sweeps. The forward-return is used for updating system frequency and bus voltages based on the calculated mismatch in active and reactive power, thus eliminating the need for a slack bus or fixed system frequency to obtain the solution. Moreover, unlike the Newton-Raphson (NR) or Newton trust region (NTR) methods, the proposed technique is inversion-free, which makes it more effective for radial distribution systems, as matrices may suffer from singularity, especially for large R/X. The solution is thus fast enough to be suitable for meeting the requirements for the smart grid applications.

An additional benefit is that, in contrast to NR and NTR methods that require the formulation of Jacobian and Hessian matrices and hence are formulated centrally, the FR-FBS has no central formulation. Furthermore, distribution systems are known for their high R/X ratio which deteriorates the diagonal dominance of the Jacobian matrix and thus affects the convergence process. The proposed algorithm, however, has shown efficient performance in terms of convergence and execution time, as demonstrated by case studies applied to the IEEE 38-bus system. In addition, the proposed FR-FBS algorithm, like NR and NTR algorithms, allows for different load models and accounts for practical microgrid operating conditions, which are demonstrated by considering the constant PQ load model as well as the frequency-dependent model in the presented case studies.

The FR-FBS algorithm was validated based on a comparison of the results with those obtained from a time-domain-based simulation for a 6-bus system that is typically used in small signal stability analysis and which is easy to be built in PSCAD/EMTDC. Hence, instead of constructing complicated

time-domain models for obtaining a steady-state solution, the proposed algorithm offers a swift, reliable and simple alternative.

The proposed algorithm was also validated by comparing it to a numerical-based load flow technique. While it gives the exact same results obtained with NTR when applied to the IEEE 38 bus system, it requires only a fraction of the time to converge. This proved the accuracy and efficiency of the FR-FBS in the load flow analysis of isolated microgrid. The application of load flow analysis in studying the load-ability effect on isolated microgrids has been illustrated by obtaining the voltage profiles during different loading conditions as well as obtaining load sharing among DGs to ensure proper sharing without voltage violations. This novel power flow technique represents a vital tool for many smart grid applications, such as self-adequacy studies for successful islanding, online energy management, optimal microgrid reconfiguration, and small signal stability analyses of isolated microgrids. The presented algorithm has been extended for the steady-state analysis of islanded hybrid microgrids.

In addition, the proposed algorithm divides the load flow of the hybrid system into two coupled sub-problems that are solved sequentially. Branch-based algorithms have been developed for the ac and dc microgrids, which are then integrated based on the IC characteristics in order to form the proposed load flow tool. The developed algorithm is derivative-free and overcomes the challenges associated with the application of branch-based algorithms for isolated hybrid microgrids.

Thus, the algorithm has been explained in detail. Its implementation for a simple hybrid system has been illustrated, along with its application for a modified IEEE 38-bus system. The algorithm has proven highly suitable for performing numerous steady-state analyses, such as effects of load variations, a variety of IC control strategies, and the probabilistic nature of the impact of renewable resources and loads on system performance. The simplicity of the developed algorithm and its minimal computational requirements represent crucial advantages that could facilitate its practical implementation in future hybrid microgrids. Moreover, the proposed algoithm fits the operational requirements of the adaptive self-adequate microgrids presented in Chapter 4. The application of the load flow for microgrids with dynamic boundries needs a flexible formulation to fit the merging/demerging of microgrid clutsers, and thus the developed algoithm is an ideal candidate for such an application, as discussed throughout this chapter.

Chapter 7
Summary, Contributions, and Future Work

7.1 Summary and Conclusions

The broad objective of the work presented in this thesis was to present a framework to enable the realization of smart grids through clustering distribution systems into adaptive self-adequate microgrids – limited in size – that can be controlled as a single entity. Numerous technical challenges associated with this transition have been addressed in this work, and novel probabilistic models, a planning framework, and steady-state analysis tools have been developed. A detailed summary of the main studies performed in this research are presented below.

The first element of this research is to develop novel probabilistic models (Chapter 3) for the per-unit power of loads and renewable-based DGs. The developed models are continuous and represent the best-fit probability distribution function (PDF) for the attained historical data. The best-fit PDF is obtained using the Kolmogorov-Smirnov test (K-S) as well as the Anderson-Darling test (A-D) that measures the discrepancy between given data samples and hypothetical PDFs. Based on the Monte-Carlo-Simulation (MCS), a probabilistic power flow (PPF) algorithm is developed by the integration of the obtained probabilistic models with the well-known forward/backward sweep power flow. Chapter 4 provided a novel paradigm to divide existing bulky grids into adaptive self-adequate microgrids that change their boundary to balance local loads and generation. To that end, the developed PPF tool is used to analyze the system to identify the weakly loaded lines, thus setting a number of virtual boundaries for potential self-adequate microgrids. A series of operating scenarios were investigated and the common boundaries used to find the minimum number of building clusters to ensure self-adequacy during the scenarios. Moreover, an operational strategy was introduced to realize the proposed adaptive paradigm.

The second element of this research is the development of a planning framework for hybrid ac-dc microgrids that considers the probabilistic nature of load and generation and the availability of interconnection links between microgrids, as presented in Chapter 5. The proposed framework decides

on the optimal configuration of the system and selects the optimal generation mix to satisfy the power balance constraints. Thus, in addition to selecting the type of microgrid (ac or dc), the framework sizes renewable DGs, dispatchable DGs, energy storage and capacitors. The planning problem is formulated as a mixed integer nonlinear program to minimize the levelized investment cost, comprised of both capital and O&M costs. A variety of case studies have been conducted in order to demonstrate the effectiveness of the proposed framework in planning these novel hybrid paradigms.

The final part of the research is the introduction of a novel branch-based load flow algorithm for islanded ac-microgrids and islanded ac-dc microgrids, as introduced in Chapter 6. Although branch-based techniques are touted for their superiority when analyzing distribution systems characterized by high R/X ratio, these methods fail when applied in islanded microgrids. Branch-based techniques rely on having a slack bus to guarantee convergence, which does not exist in islanded microgrids and represents a serious flaw in these techniques. Moreover, droop-regulated DGs represent serious challenges especially when calculating the reactive power share between DGs, given that their bus voltages are unequal and unknown. The proposed novel algorithm adapts the well-known forward-backward sweep technique to solve the load flow of islanded microgrids by categorizing the system nodes and lines into predefined categories and using them to direct the solution to guarantee convergence. The proposed algorithm is capable of dealing with the absence of a slack bus and can handle the droop-regulated DGs efficiently. The accuracy of the obtained results has been verified through the comparison with a detailed time-domain simulations using PSCAD/EMTDC. Distinct from NR and Newton-Trusted-Region (NTR), the proposed algorithm is derivative-free, matrix-free, and has no complex number calculations. Thus, it is simple, swift, and compatible with the limited computational burden of distributed agents.

Furthermore, the algorithm has been extended to perform steady-state analysis of islanded hybrid ac-dc microgrids considering the control strategy of the interlinking converter connecting both microgrids. A variety of case studies have been conducted in order to demonstrate the effectiveness, robustness, and convergence characteristics of the developed power flow algorithm.

7.2 Contributions

The major contributions of the work presented in this thesis can be summarized as follows:

1. Probabilistic models for load and renewable generation have been developed and integrated with conventional FBS power flow to establish a PPF tool.

2. A novel microgrid paradigm and operation philosophy has been introduced to form self-adequate microgrids from the existing distribution networks during different possible operating scenarios. The proposed paradigm improves the reliability of the power system by ensuring load-generation balance within the obtained virtual boundaries.

3. A planning framework for hybrid ac/dc microgrids has been introduced to minimize the levelized investment cost. This framework sets the type of microgrids and designs the necessary generation and storage capacities to balance load and generation with minimum operation and maintenance cost.

4. A branch-based load flow algorithm has been developed to perform steady-state analysis for islanded ac and hybrid ac/dc microgrids. The proposed algorithm successfully overcomes the challenges of applying FBS techniques in the absence of slack bus and considering droop-controlled DGs.

7.3 Direction of Future Work

Based on the results presented in this thesis, the following areas are suggested for future investigation:

1. Conducting of a small signal stability analysis for the clustered self-adequate microgrids to ensure the seamless transitions between different operating modes. Based on this stability analysis, setting the stable boundary limits for droop coefficients and inter-microgrids energy exchange limits.

2. Development of an OPF algorithm for islanded hybrid ac/dc microgrids. This algorithm would be capable of dispatching load that considers the probabilistic behavior of renewable-based DGs and constraints with the limits obtained from the small signal stability studies.

3. Development of a synchronization control algorithm to reconnect islanded clusters to form the original distribution system after clearing the disturbance. This procedure would be a part of the microgrid agent's functionalities. The restoration plan should be studied based on the stability of the available clusters conducted using small signal stability.

Bibliography

[1] "About Renewable Energy | Natural Resources Canada." [Online]. Available: http://www.nrcan.gc.ca/energy/renewable-electricity/7295#wind. [Accessed: 15-Feb-2017].

[2] X. Fang, S. Misra, G. Xue, and D. Yang, "Smart Grid – The New and Improved Power Grid :A Survey," *IEEE Commun. Surv. Tutorials*, vol. 14, no. 4, pp. 944–980, 2012.

[3] E. Jung, H. Yoo, S.-K. Sul, H.-S. Choi, and Y.-Y. Choi, "A Nine-Phase Permanent-Magnet Motor Drive System for an Ultrahigh-Speed Elevator," *IEEE Trans. Ind. Appl.*, vol. 48, no. 3, pp. 987–995, May 2012.

[4] A. A. Hamad, H. E. Farag, and E. F. El-Saadany, "A Novel Multiagent Control Scheme for Voltage Regulation in DC Distribution Systems," *IEEE Trans. Sustain. Energy*, vol. 6, no. 2, pp. 534–545, Apr. 2015.

[5] A. A. Hamad, M. A. Azzouz, and E. F. El-Saadany, "Multiagent Supervisory Control for Power Management in DC Microgrids," *IEEE Trans. Smart Grid*, vol. 7, no. 2, p. 1, 2015.

[6] G. Reed, B. Grainger, A. Sparacino, and Z.-H. Mao, "Ship to Grid: Medium-Voltage DC Concepts in Theory and Practice," *IEEE Power Energy Mag.*, vol. 10, no. 6, pp. 70–79, Nov. 2012.

[7] L. A. de Souza Ribeiro, O. R. Saavedra, S. L. de Lima, and J. G. de Matos, "Isolated Micro-Grids With Renewable Hybrid Generation: The Case of Lençóis Island," *IEEE Trans. Sustain. Energy*, vol. 2, no. 1, pp. 1–11, Jan. 2010.

[8] T. S. Ustun, C. Ozansoy, and A. Zayegh, "Universities Power Engineering Conference (AUPEC), 2011 21st Australasian," *Universities Power Engineering Conference (AUPEC), 2011 21st Australasian*. pp. 1–6, 2011.

[9] A. A. Hamad, M. A. Azzouz, and E. F. El Saadany, "A Sequential Power Flow Algorithm for Islanded Hybrid AC/DC Microgrids," *IEEE Trans. Power Syst.*, vol. PP, no. 99, pp. 1–10, 2015.

[10] A. Mohamed, V. Salehi, and O. Mohammed, "Real-Time Energy Management Algorithm for Mitigation of Pulse Loads in Hybrid Microgrids," *IEEE Trans. Smart Grid*, vol. 3, no. 4, pp. 1911–1922, Dec. 2012.

[11] S. A. Arefifar and Y. A.-R. I. Mohamed, "Probabilistic Optimal Reactive Power Planning in Distribution Systems With Renewable Resources in Grid-Connected and Islanded Modes," *IEEE Trans. Ind. Electron.*, vol. 61, no. 11, pp. 5830–5839, Nov. 2014.

[12] J. Xiao, L. Bai, F. Li, H. Liang, and C. Wang, "Sizing of Energy Storage and Diesel Generators in an Isolated Microgrid Using Discrete Fourier Transform (DFT)," *IEEE Trans. Sustain. Energy*, vol. 5, no. 3, pp. 907–916, Jul. 2014.

[13] G. Diaz, C. Gonzalez-Moran, J. Gomez-Aleixandre, and A. Diez, "Scheduling of Droop Coefficients for Frequency and Voltage Regulation in Isolated Microgrids," *IEEE Trans. Power Syst.*, vol. 25, no. 1, pp. 489–496, Feb. 2010.

[14] M. M. A. Abdelaziz and E. F. El-Saadany, "Maximum loadability consideration in droop-controlled islanded microgrids optimal power flow," *Electr. Power Syst. Res.*, vol. 106, pp. 168–179, 2014.

[15] M. M. A. Abdelaziz, H. E. Farag, and E. F. El-Saadany, "Optimum Droop Parameter Settings of Islanded Microgrids With Renewable Energy Resources," *IEEE Trans. Sustain. Energy*, vol. PP, no. 99, p. 1, Apr. 2014.

[16] R. Ramakumar and P. Chiradeja, "Distributed generation and renewable energy systems," in *IECEC '02. 2002 37th Intersociety Energy Conversion Engineering Conference, 2002.*, 2002, pp. 716–724.

[17] A. Latheef, M. Negnevitsky, K. Muttaqi, and S. Perera, "Present Understanding of the Impact of Distributed Generation on Power Quality," in *Power Engineering Conference, 2008. AUPEC '08. Australasian Universities*, 2008, pp. 1–6.

[18] Z. Wang, J. Li, W. Yang, and Z. Shi, "Impact of Distributed Generation on the power supply reliability," in *IEEE PES Innovative Smart Grid Technologies*, 2012, pp. 1–5.

[19] T. E. McDermott, U. Electrotek Concepts, Clairton, PA, and R. . Dugan, "Distributed generation impact on reliability and power quality indices," in *Rural Electric Power Conference, 2002. 2002 IEEE*, 2002, pp. D3 – D3_7.

[20] S. K. Salman, S. Member, and I. M. Rida, "Investigating the Impact of Embedded Generation on Relay Settings of Utilities ' Electrical Feeders," vol. 16, no. 2, pp. 246–251, 2001.

[21] R. A. R. Walling, R. Saint, S. Member, R. C. Dugan, J. Burke, and L. A. Kojovic, "Summary of Distributed Resources Impact on Power Delivery Systems," vol. 23, no. 3, pp. 1636–1644, 2008.

[22] M. I. Marei, E. F. El-saadany, and M. M. A. Salama, "A Novel Control Algorithm for the DG Interface to Mitigate Power Quality Problems," *IEEE Trans. Power Deliv.*, vol. 19, no. 3, pp. 1384–1392, 2004.

[23] G. Tang and M. R. Iravani, "Application of a Fault Current Limiter To Minimize Distributed Generation Impact on Coordinated Relay Protection," pp. 1–6, 2010.

[24] M. I. M. I. Marei, E. F. El-Saadany, and M. M. A. Salama, "A Flexible DG Interface Based on a New RLS Algorithm for Power Quality Improvement," *IEEE Syst. J.*, vol. 6, no. 1, pp. 68–75, Mar. 2012.

[25] S. A. A. Shahriari, S. Member, M. Abapour, A. Yazdian, M. R. Haghifam, and S. Member, "Minimizing the Impact of Distributed Generation on Distribution Protection System by Solid State Fault Current Limiter," in *Transmission and Distribution Conference and Exposition, 2010 IEEE PES*, 2010, pp. 1–7.

[26] Y. M. Atwa, E. F. El-Saadany, M. M. A. Salama, R. Seethapathy, M. Assam, and S. Conti, "Adequacy Evaluation of Distribution System Including Wind/Solar DG During Different Modes of Operation," *IEEE Trans. Power Syst.*, vol. 26, no. 4, pp. 1945–1952, Nov. 2011.

[27] Y. M. Atwa and E. F. El-Saadany, "Probabilistic approach for optimal allocation of wind- based distributed generation in distribution systems," *IET Renew. Power Gener.*, vol. 5, no. 1, pp. 79–88, 2009.

[28] J. Hetzer, D. C. Yu, and K. Bhattarai, "An Economic Dispatch Model Incorporating Wind Power," *IEEE Trans. Energy Convers.*, vol. 23, no. 2, pp. 603–611, 2008.

[29] IESO, "A Progress Report on Contracted Electricity Supply," 2016.

[30] B. S. Borowy and Z. M. Salameh, “Optimum Photovoltaic Array Size for a Hybrid Wind/PV System,” *IEEE Trans. Energy Convers.*, vol. 9, no. 3, pp. 482–488, 1994.

[31] “IEEE reliability test system - a report prepared by the reliability test system task force of the application of probability methods subcommittee,” *IEEE Trans. Power Appar. Syst.*, vol. PAS-98, no. 6, pp. 2047–2054, 1979.

[32] G. T. Heydt, “The Next Generation of Power Distribution Systems,” *IEEE Trans. Smart Grid*, vol. 1, no. 3, pp. 225–235, 2010.

[33] Smart Grid and Cyber-Physical Systems Program Office, “NIST Framework and Roadmap for Smart Grid Interoperability, Release 3,” 2014.

[34] H. Farhangi, “A Road Map to Integration,” *IEEE Power and Energy Magazine*, no. june, pp. 52–66, 2014.

[35] F. D. Kanellos, A. I. Tsouchnikas, N. D. Hatziargyriou, and S. Member, “Micro-Grid Simulation during Grid-Connected and Islanded Modes of Operation,” *Int. Conf. Power Syst. Transients*, vol. 8, 2005.

[36] M. A. Pedrasa and T. Spooner, “A Survey of Techniques Used to Control Microgrid Generation and Storage during Island Operation,” in *Australian Universities Power Engineering Conference*, 2006, pp. 1–6.

[37] R. Majumder, “Modelling, stability analysis and control of microgrid,” Queensland University of Technology, 2010.

[38] Z. Ye, R. Walling, N. Miller, P. Du, and K. Nelson, “Facility Microgrids,” Niskayuna, New York, 2005.

[39] L. Tao, C. Schwaegerl, S. Narayanan, and J. H. Zhang, “From Laboratory Microgrid to Real Markets — Challenges and Opportunities,” in *8th International Conference on Power Electronics - ECCE Asia*, 2011, pp. 264–271.

[40] T. E. D. C. Huayllas, D. S. Ramos, and R. L. Vasquez-Arnez, “Microgrid Systems : Current Status and Challenges,” in *Transmission and Distribution Conference and Exposition: Latin America (T&D-LA)*, 2010, vol. 900, pp. 7–12.

[41] M. R. Miveh, M. Gandomkar, S. Mirsaeidi, and M. R. Gharibdoost, “A Review on Protection Challenges in Microgrids,” in *17th Conference on Electrical Power Distribution Networks (EPDC)*, 2012, pp. 1–5.

[42] J. Kim, S. Kim, and J. Park, “Contribution of an Energy Storage System for Stabilizing a Microgrid during Islanded Operation,” *Jounal Electr. Eng. Technol.*, vol. 4, no. 2, pp. 194–200, 2009.

[43] P. Basak, A. K. Saha, S. Chowdhury, and S. P. Chowdhury, “Microgrid : Control Techniques and Modelling,” in *44th International Universities Power Engineering Conference (UPEC)*, 2009, pp. 1–5.

[44] E. Barklund, N. Pogaku, and M. Prodanovi, “Energy Management in Autonomous Microgrid using Stability-Constrained Droop Control of Inverters,” *IEEE Trans. Power Electron.*, vol. 23, no. 5, pp. 2346–2352, 2008.

[45] M. N. Marwali, J. Jung, S. Member, and A. Keyhani, "Control of Distributed Generation Systems — Part II : Load Sharing Control," *IEEE Trans. Power Electron.*, vol. 19, no. 6, pp. 1551–1561, 2004.

[46] P. Piagi and R. H. Lasseter, "Autonomous control of microgrids," in *2006 IEEE Power Engineering Society General Meeting*, 2006, pp. 1–8.

[47] J. M. Guerrero, J. C. Vasquez, J. Matas, L. G. de Vicuna, and M. Castilla, "Hierarchical Control of Droop-Controlled AC and DC Microgrids—A General Approach Toward Standardization," *IEEE Trans. Ind. Electron.*, vol. 58, no. 1, pp. 158–172, Jan. 2011.

[48] K. T. M. Oshiro, S. T. A. Yona, and T. F. C. Kim, "Decentralised control of voltage in distribution systems by distributed generators," *IET Gener. Transm. Distrib.*, vol. 4, no. 11, pp. 1251–1260, 2010.

[49] D. Georgakis, S. Papathanassiou, N. Hatziagrgyriou, A. Engler, and C. Hardt, "Operation of a prototype microgrid system based on micro-sources quipped with fast-acting power electronics interfaces," in *35th Annual Power Electronics Specialists Conference PESC*, 2004, pp. 2521–2526.

[50] J. Lopes, "Defining control strategies for microgrids islanded operation," *IEEE Trans. Power Syst.*, vol. 21, no. 2, pp. 916–924, 2006.

[51] J. Lopes, C. Moreira, and F. Resende, "Microgrids black start and islanded operation," in *15th Power Systems Conference (PSCC)*, 2005, no. August, pp. 22–26.

[52] J. Lopes and C. Moreira, "Control strategies for microgrids emergency operation," in *International Conference on Future Power Systems*, 2005, pp. 1–6.

[53] H. Laaksonen, "Voltage and frequency control of inverter based weak LV network microgrid," in *International Conference on Future Power SystemsFuture Power Systems*, 2005, no. 2, p. 6 pp.–6.

[54] M. Kouluri and R. Pandey, "Intelligent agent based micro grid control," in *2nd International Conference on Intelligent Agent and Multi-Agent Systems (IAMA)*, 2011, pp. 62–66.

[55] A. A. Hamad, M. A. Azzouz, and E. F. El Saadany, "A Sequential Power Flow Algorithm for Islanded Hybrid AC/DC Microgrids," *IEEE Trans. Power Syst.*, vol. 31, no. 5, pp. 3961–3970, Sep. 2016.

[56] X. Lu, S. Member, J. M. Guerrero, S. Member, K. Sun, J. C. Vasquez, R. Teodorescu, and L. Huang, "Hierarchical Control of Parallel AC-DC Converter Interfaces for Hybrid Microgrids," *IEEE Trans. Smart Grid*, vol. 5, no. 2, pp. 683–692, 2014.

[57] X. Liu, P. Wang, and P. C. Loh, "A Hybrid AC/DC Microgrid and Its Coordination Control," *IEEE Trans. Smart Grid*, vol. 2, no. 2, pp. 278–286, 2011.

[58] P. C. Loh, D. Li, Y. K. Chai, and F. Blaabjerg, "Autonomous Operation of Hybrid Microgrid With AC and DC Subgrids," *IEEE Trans. Power Electron.*, vol. 28, no. 5, pp. 2214–2223, May 2013.

[59] M. M. A. Abdelaziz, H. E. Farag, E. F. El-Saadany, and Y. A.-R. I. Mohamed, "A Novel and Generalized Three-Phase Power Flow Algorithm for Islanded Microgrids Using a Newton Trust Region Method," *IEEE Trans. Power Syst.*, vol. 28, no. 1, pp. 190–201, Feb. 2013.

[60] F. Mumtaz, M. H. Syed, M. Al Hosani, and H. H. Zeineldin, "A Novel Approach to Solve Power Flow for Islanded Microgrids Using Modified Newton Raphson With Droop Control of DG," *IEEE Trans. Sustain. Energy*, vol. 7, no. 2, pp. 493–503, 2016.

[61] A. Elrayyah, Y. Sozer, and M. E. Elbuluk, "A Novel Load-Flow Analysis for Stable and Optimized Microgrid Operation," *IEEE Trans. Power Deliv.*, vol. 29, no. 4, pp. 1709–1717, Aug. 2014.

[62] W. Wang and M. Barnes, "Power Flow Algorithms for Multi-Terminal VSC-HVDC With Droop Control," *IEEE Trans. Power Syst.*, vol. 29, no. 4, pp. 1721–1730, Jul. 2014.

[63] J. Beerten, S. Cole, and R. Belmans, "Generalized Steady-State VSC MTDC Model for Sequential AC/DC Power Flow Algorithms," *IEEE Trans. Power Syst.*, vol. 27, no. 2, pp. 821–829, May 2012.

[64] C. Li, S. K. Chaudhary, J. C. Vasquez, and J. M. Guerrero, "Power flow analysis for droop controlled LV hybrid AC-DC microgrids with virtual impedance," in *2014 IEEE PES General Meeting | Conference {&} Exposition*, 2014, pp. 1–4.

[65] A. A. Eajal, M. A. Abdelwahed, E. F. El-Saadany, and K. Ponnambalam, "A Unified Approach to the Power Flow Analysis of AC/DC Hybrid Microgrids," *IEEE Trans. Sustain. Energy*, vol. 7, no. 3, pp. 1145–1158, Jul. 2016.

[66] J. Hetzer and K. Bhattarai, "An Economic Dispatch Model Incoperating Wind Power," *IEEE Trans. Energy Convers.*, vol. 23, no. 2, pp. 603–611, 2008.

[67] A. Soroudi, M. Aien, and M. Ehsan, "A Probabilistic Modelling of Photo Voltaic Modules and Wind Power Generation Impact on," *IEEE Syst. J.*, vol. 6, no. 2, pp. 254–259, 2012.

[68] B. W. Woodruff, A. H. Moore, E. J. Dunne, and R. Cortes, "A Modified Kolmogorov-Smirnov Test for Weibull Distributions with Unknown Location and Scale Parameters," *IEEE Trans. Reli.*, vol. R-32, no. 2, pp. 209–213, 1983.

[69] T. W. Anderson and D. A. Darling, "A Test of Goodness of Fit," *J. Am. Stat. Assoc.*, vol. 49, no. 268, pp. 765–769, 1954.

[70] Y. M. Atwa, E. F. El-Saadany, M. M. A. Salama, and R. Seethapathy, "Optimal Renewable Resources Mix for Distribution System Energy Loss Minimization," *IEEE Trans. Power Syst.*, vol. 25, no. 1, pp. 360–370, Feb. 2010.

[71] J. Hetzer, D. C. Yu, and K. Bhattarai, "An Economic Dispatch Model Incorporating Wind Power," *IEEE Trans. Energy Convers.*, vol. 23, no. 2, pp. 603–611, Jun. 2008.

[72] S. Sarkar and V. Ajjarapu, "MW Resource Assessment Model for a Hybrid Energy Conversion System With Wind and Solar Resources," *IEEE Trans. Sustain. Energy*, vol. 2, no. 4, pp. 383–391, Oct. 2011.

[73] A. Likas, N. Vlassis, and J. J. Verbeek, "The global k -means clustering algorithm," *Elsevier Pattern Recognit. Soc.*, vol. 36, no. 1, pp. 451–461, 2003.

[74] J. Morales and J. Perez-Ruiz, "Point estimate schemes to solve the probabilistic power flow," *IEEE Trans. Power Syst.*, vol. 22, no. 4, pp. 1594–1601, 2007.

[75] M. D. S. Noratiqah, A. Asmat, and S. Mansor, "Seasonal wind speed distribution analysis in

west coast of Malaysia," in *2012 International Conference on Statistics in Science, Business and Engineering (ICSSBE)*, 2012, pp. 1–5.

[76] A. G. Glen, L. M. Leemis, and D. R. Barr, "Order statistics in goodness-of-fit testing," *IEEE Trans. Reliab.*, vol. 50, no. 2, pp. 209–213, Jun. 2001.

[77] E. McGrath and D. Irving, *Techniques for Efficient Monte Carlo Simulation. Volume II. Random Number Generation for Selected Probability Distributions.* US: National Technical Information Service, 1973.

[78] G. Verbic, A. Schellenberg, W. Rosehart, and C. A. Canizares, "Probabilistic optimal power flow applications to electricity markets," in *International Conference on Probabilistic Methods Applied to Power Systems, PMAPS*, 2006, pp. 1–6.

[79] C. S. Cheng, "A modified Newton method for radial distribution system power flow analysis," *IEEE Trans. Power Syst.*, vol. 12, no. 1, pp. 389–397, 1997.

[80] S. A. Arefifar, Y. A.-R. I. Mohamed, and T. H. M. El-Fouly, "Supply-Adequacy-Based Optimal Construction of Microgrids in Smart Distribution Systems," *IEEE Trans. Smart Grid*, vol. 3, no. 3, pp. 1491–1502, Sep. 2012.

[81] Q. Fu, "Modelling, analyses and assessment of microgrids considering high renewable energy penetration," University of Wisconsin-Milwaukee, 2013.

[82] M. Smith and D. Ton, "'Key connections: The U.S. department of energy's microgrid initiative,'" *IEEE Power Energy Mag.*, vol. 11, no. 4, pp. 22–27.

[83] L. Jikeng, W. Xudong, W. Peng, L. Shengwen, S. Guang-hui, M. Xin, X. Xing-wei, and L. Shanshan, "Two-stage method for optimal island partition of distribution system with distributed generations," *IET Gener. Transm. Distrib.*, vol. 6, no. 3, p. 218, 2012.

[84] S. A. Arefifar, Y. A.-R. I. Mohamed, and T. H. M. EL-Fouly, "Optimum Microgrid Design for Enhancing Reliability and Supply-Security," *IEEE Trans. Smart Grid*, vol. 4, no. 3, pp. 1567–1575, Sep. 2013.

[85] F. S. Abu-Mouti and M. E. El-Hawary, "Optimal Distributed Generation Allocation and Sizing in Distribution Systems via Artificial Bee Colony Algorithm," *IEEE Trans. Power Deliv.*, vol. 26, no. 4, pp. 2090–2101, Oct. 2011.

[86] M. F. Akorede, H. Hizam, I. Aris, and M. Z. A. Ab Kadir, "Effective method for optimal allocation of distributed generation units in meshed electric power systems," *IET Gener. Transm. Distrib.*, vol. 5, no. 2, p. 276, 2011.

[87] Y. M. Atwa and E. F. El-Saadany, "Probabilistic approach for optimal allocation of wind-based distributed generation in distribution systems," *IET Renew. Power Gener.*, vol. 5, no. 1, p. 79, 2011.

[88] H. A. Hejazi, A. R. Araghi, B. Vahidi, S. H. Hosseinian, M. Abedi, and H. Mohsenian-Rad, "Independent distributed generation planning to profit both utility and DG investors," *IEEE Trans. Power Syst.*, vol. 28, no. 2, pp. 1170–1178, May 2013.

[89] A. Keane and M. O'Malley, "Optimal Allocation of Embedded Generation on Distribution Networks," *IEEE Trans. Power Syst.*, vol. 20, no. 3, pp. 1640–1646, Aug. 2005.

[90] M. F. Shaaban, Y. M. Atwa, and E. F. El-Saadany, "DG allocation for benefit maximization in distribution networks," *IEEE Trans. Power Syst.*, vol. 28, no. 2, pp. 639–649, May 2013.

[91] M. Baran and F. Wu, "Optimal capacitor placement on radial distribution systems," *Power Deliv. IEEE Trans.*, vol. 4, no. 1, 1989.

[92] H. Lotfi and A. Khodaei, "AC Versus DC Microgrid Planning," *IEEE Trans. Smart Grid*, vol. PP, no. 99, p. 1, 2015.

[93] S. Mashayekh and K. L. Butler-Purry, "An Integrated Security-Constrained Model-Based Dynamic Power Management Approach for Isolated Microgrids in All-Electric Ships," *IEEE Trans. Power Syst.*, vol. 30, no. 6, pp. 2934–2945, Nov. 2015.

[94] Z. Zhao, P. Yang, J. Guerrero, Z. Xu, and T. Green, "Multiple-Time-Scales Hierarchical Frequency Stability Control Strategy of Medium-Voltage Isolated Microgrid," *IEEE Trans. Power Electron.*, vol. 31, no. 8, p. 1, 2015.

[95] J. M. Guerrero, M. Chandorkar, T.-L. Lee, and P. C. Loh, "Advanced Control Architectures for Intelligent Microgrids—Part I: Decentralized and Hierarchical Control," *IEEE Trans. Ind. Electron.*, vol. 60, no. 4, pp. 1254–1262, Apr. 2013.

[96] R. G. Deshmukh and R. Ramakumar, "Reliability analysis of combined wind-electric and conventional generation systems," *Sol. Energy*, vol. 28, no. 4, pp. 345–352, 1982.

[97] W. G. Willis, H. L., & Scott, *Distributed Power Generation: Planning and Evaluation*. New York: CRC Press, 2000.

[98] M. M. A. Abdelaziz and E. F. El-Saadany, "Voltage and Reactive Power Impacts on Successful Operation of Islanded Microgrids," *IEEE Trans. Power Syst.*, vol. 28, no. 2, pp. 1716–1727, May 2013.

[99] C. A. Hernandez-Aramburo, T. C. Green, and N. Mugniot, "Fuel Consumption Minimization of a Microgrid," *IEEE Trans. Ind. Appl.*, vol. 41, no. 3, pp. 673–681, May 2005.

[100] G. Daelemans, "VSC HVDC in meshed networks," Katholieke Universiteit Leuven, Leuven, Belgium, 2008.

[101] M. E. Nassar and M. M. A. Salama, "Probabilistic Power Flow Using Novel Wind and Solar Probabilistic Models," in *2016 IEEE Power and Energy Society General Meeting (PESGM)*, 2016, pp. 1–5.

[102] K. Qian, C. Zhou, M. Allan, and Y. Yuan, "Modelling of Load Demand Due to EV Battery Charging in Distribution Systems," *IEEE Trans. Power Syst.*, vol. 26, no. 2, pp. 802–810, 2011.

[103] US Energy Information Adminstration, "Levelized Cost and Levelized Avoided Cost of New Generation Resources in the Annual Energy Outlook 2016 Levelized Cost of Electricity (LCOE) and its limitations Levelized Avoided Cost of Electricity (LACE) as an additional indicator," 2016.

[104] G. X. Luo and A. Semlyen, "Efficient load flow for large weakly meshed networks," *IEEE Trans. Power Syst.*, vol. 5, no. 4, pp. 1309–1316, 1990.

[105] D. Joyner, M. Van Nguyen, and N. Cohen, *Algorithmic Graph Theory*. 2012.

[106] D. Singh, R. K. Misra, and D. Singh, "Generation Planning," *IEEE Trans. Power Syst.*, vol. 22,

no. 4, pp. 2204–2212, 2007.

[107] "Guest editorial - special issue on power electronics in DC distribution systems," *IEEE Trans. Power Electron.*, vol. 28, no. 4, pp. 1507–1508, Apr. 2013.

[108] M. Shahidehpour, "DC Microgrids: Economic Operation and Enhancement of Resilience by Hierarchical Control," *IEEE Trans. Smart Grid*, vol. 5, no. 5, pp. 2517–2526, Sep. 2014.

[109] H. M. A. Ahmed, A. B. Eltantawy, and M. M. A. Salama, "A Planning Approach for the Network Configuration of AC-DC Hybrid Distribution Systems," *IEEE Trans. Smart Grid*, p. 1, 2016.

[110] N. Eghtedarpour and E. Farjah, "Power Control and Management in a Hybrid AC/DC Microgrid," *IEEE Trans. Smart Grid*, vol. 5, no. 3, pp. 1494–1505, May 2014.

[111] P. C. Loh, D. Li, Y. K. Chai, and F. Blaabjerg, "Autonomous Control of Interlinking Converter With Energy Storage in Hybrid AC–DC Microgrid," *IEEE Trans. Ind. Appl.*, vol. 49, no. 3, pp. 1374–1382, May 2013.

[112] C. S. Cheng and D. Shirmohammadi, "A three-phase power flow method for real-time distribution system analysis," *IEEE Trans. Power Syst.*, vol. 10, no. 2, pp. 671–679, May 1995.

[113] S. M. Moghaddas-Tafreshi and E. Mashhour, "Distributed generation modelling for power flow studies and a three-phase unbalanced power flow solution for radial distribution systems considering distributed generation," *Electr. Power Syst. Res.*, vol. 79, no. 4, pp. 680–686, Apr. 2009.

[114] A. B. Eltantawy and M. M. A. Salama, "A Novel Zooming Algorithm for Distribution Load Flow Analysis for Smart Grid," *IEEE Trans. Smart Grid*, vol. 5, no. 4, pp. 1704–1711, Jul. 2014.

[115] A. Cataliotti, V. Cosentino, D. Di Cara, P. Russotto, E. Telaretti, and G. Tine, "An Innovative Measurement Approach for Load Flow Analysis in MV Smart Grids," *IEEE Trans. Smart Grid*, vol. 7, no. 2, pp. 889–896, Mar. 2016.

Appendix A

IEEE-RTS data

This system provides daily load profiles for one year. The data are provided in three sets of tables, as follows:

- Weekly peak load as a percentage of the annual peak load, as presented in Table A.1.
- Daily peak load as a percentage of the weekly peak, as presented in Table A.2.
- Hourly peak load as a percentage of the daily peak load, as presented in Table A.3.

Table A.1 Weekly Peak Load as Percentage of Annual Peak

Week	Peak Load	Week	Peak Load
1	86.2	27	75.5
2	90	28	81.6
3	87.8	29	80.1
4	83.4	30	88
5	88	31	72.2
6	84.1	32	77.6
7	83.2	33	80
8	80.6	34	72.9
9	74	35	72.6
10	73.7	36	70.5
11	71.5	37	78
12	72.7	38	69.5
13	70.4	39	72.4
14	75	40	72.4
15	72.1	41	74.3
16	80	42	74.4
17	75.4	43	80
18	83.7	44	88.1
19	87	45	88.5
20	88	46	90.9
21	85.6	47	94
22	81.1	48	89
23	90	49	94.2
24	88.7	50	97
25	89.6	51	100
26	86.1	52	95.2

Table A.2 Daily Peak Load as Percentage of Weekly Peak

Day	Peak Load
Monday	93
Tuesday	100
Wednesday	98
Thursday	96
Friday	94
Saturday	77
Sunday	75

Table 7.3 Hourly Peak Load as Percentage of Daily Peak

Hour	Winter Weeks (1-8 & 44-52)		Winter Weeks (18-30)		Winter Weeks (9-17 & 31-41)	
	Weekday	Weekend	Weekday	Weekend	Weekday	Weekend
12-1 am	67	78	64	74	63	75
1-2	63	72	60	70	62	73
2-3	60	68	58	66	60	69
3-4	59	66	56	65	58	66
4-5	59	64	56	64	59	65
5-6	60	65	58	62	65	65
6-7	74	66	64	62	72	68
7-8	86	70	76	66	85	74
8-9	95	80	87	81	95	83
9-10	96	88	95	86	99	89
10-11	96	90	99	91	100	92
11-Noon	95	91	100	93	99	94
Noon-1pm	95	90	99	93	93	91
1-2	95	88	100	92	92	90
2-3	93	87	100	91	90	90
3-4	94	87	97	91	88	86
4-5	99	91	96	92	90	85
5-6	100	100	96	94	92	88
6-7	100	99	93	95	96	92
7-8	96	97	92	95	98	100
8-9	91	94	92	100	96	97
9-10	83	92	93	93	90	95
10-11	73	87	87	88	80	90
11-12	63	81	72	80	70	85